
Novel structures for lattice-mismatched Infrared photodetectors

A thesis submitted in part fulfilment for the degree of
Doctor of Philosophy at the University of Lancaster

A. P. Craig (2015, revised 2016)

Supervisor: A. R. J. Marshall

No part of this thesis has been, or is being, submitted
to any other university or other academic institution

Physics

Lancaster
University



Acknowledgements

Firstly, I would like to thank my supervisor, Dr Andrew Marshall, for his tireless support, guidance and optimism throughout the last four years. I would further like to thank Prof. Antony Krier, my deputy supervisor, for his support, and for facilitating a collaboration with the group of Prof. Sanjay Krishna at Center For High Technology materials Albuquerque, USA.

I would also like to thank our colleagues at Amethyst Research – especially Manish Jain, with whom I have worked closely throughout my PhD. Amethyst have provided additional funding and given me the opportunity to take part in world-leading research.

Credit should also be given to the departmental and support staff here at Lancaster: to Steve Holden, for arranging countless purchase requests, to Stephen Holt, who provided all manner of support for all things electronic, and to Shonah Ion, who provided safety training and support.

Finally, I would like to thank my parents and my grandmother for their belief in me and for all their love.

Papers published

- **A. P. Craig**, A. R. J. Marshall, Z.-B. Tian, S. Krishna and A. Krier, “Mid-infrared InAs_{0.79}Sb_{0.21}-based *nBn* photodetectors with Al_{0.9}Ga_{0.2}As_{0.1}Sb_{0.9} barrier layers, and comparisons with InAs_{0.87}Sb_{0.13} *p-i-n* diodes, both grown on GaAs using interfacial misfit arrays”, Applied Physics Letters, 103 253502 (2013).
- **A. P. Craig**, C. J. Reyner, A. R. J. Marshall and D. L. Huffaker, “Excess noise in GaAs and AlGaAs avalanche photodiodes with GaSb absorption regions—composite structures grown using interfacial misfit arrays”, Applied Physics Letters, 104, 213502 (2014).
- **A. P. Craig**, A. R. J. Marshall, Z.-B. Tian and S. Krishna, “Mid-infrared InAsSb-based *nBn* photodetectors with AlGaAsSb barrier layers – grown on GaAs, using an interfacial misfit array, and on native GaSb”, Infrared Physics and Technology, 67, p210 (2014).
- **A. P. Craig**, M. Jain, G. Wicks, T. Golding, K. Hossain, K. McEwan, C. Howle, B. Percy and A. R. J. Marshall, “Short-wave infrared barrier detectors using InGaAsSb absorption material lattice matched to GaSb”, Applied Physics Letters, 106, 201103 (2015).
- **A. P. Craig**, M. D. Thompson, Z.-B. Tian, S. Krishna, A. Krier and A. R. J. Marshall, “InAsSb-based *nBn* photodetectors: lattice mismatched growth on GaAs and low-frequency noise performance.” Semiconductor Science and Technology, 30, 105011 (2015).

Papers under review

- **A. P. Craig**, P. J. Carrington, H. Liu and A. R. J. Marshall, “Heteroepitaxial techniques for the growth of 6.1 Å III-V materials on GaAs and Si – a comparison of GaSb/GaAs epitaxy and GaSb/Si epitaxy.” Journal of Crystal Growth (2015).

Oral presentations at conferences

- **A. P. Craig**, A.R.J. Marshall, C.J. Reyner, K. Nunna, G. Mariani, B.L. Liang, K.L. Wang and D.L. Huffaker “High Bandwidth 1.55 μm GaSb Photodetectors on GaAs Substrates Using an Interfacial Misfit Array”, UK Semiconductors, Sheffield (2012).

- **A. P. Craig**, A. R. J. Marshall, Z.-B. Tian and S. Krishna, “Mid-infrared InAs_{0.91}Sb_{0.09}-based *nBn* photodetectors with Al_{0.9}Ga_{0.1}As_{0.08}Sb_{0.92} barrier layers – grown on GaAs, using an Interfacial Misfit Array, and on native GaSb”,
 - Quantum Structured Infrared Photodetector (QSIP), Santa-Fe, N.M. USA (2014).
 - UK Semiconductors, Sheffield (2014).
 - Mid-IR Optoelectronics: Materials and Devices (MIOMD), Montpellier, France (2014).
- A. R. J. Marshall, **A. P. Craig**, C. J. Reyner and D. L. Huffaker, “GaAs and AlGaAs APDs with GaSb absorption regions in a separate absorption and multiplication structure using a hetero-lattice interface”,
 - Quantum Structured Infrared Photodetector (QSIP), Santa-Fe, N. M. USA (2014).
 - UK Semiconductors, Sheffield (2014).
- **A. P. Craig** and A. R. J. Marshall, “InAs_{0.91}Sb_{0.09}-based *nBn* photodetectors: the influence of absorption layer doping and 1/f noise performance”, UK Semiconductors, Sheffield (2015).
- V. Letka, **A. P. Craig**, A. Krier and A. R. J. Marshall, “LWIR InAs/InAs_{1-x}Sb_x superlattice photodetectors on GaAs substrates, with $0.315 < x < 0.35$ ”, UK Semiconductors, Sheffield (2015).

Table of contents

(1) Introduction.....	1-6
(2) Theory.....	7-31
2.i Dark Current Mechanisms.....	7
2.ii Capacitance-Voltage Measurements.....	12
2.iii Avalanche Photodiodes (APDs) and Impact Ionisation.....	14
2.iv Noise.....	15
2.v Limitations of the Local Model of Impact Ionisation.....	17
2.vi Figures of merit.....	18
2.vii Bandstructure modelling.....	20
2.viii Device structures.....	24
2.ix Critical thickness modelling.....	28
(3) Literature review.....	32-61
3.i Interfacial misfit (IMF) arrays for lattice mismatched growth.....	32
3.ii <i>nBn</i> detectors for long wavelength detectors with low dark currents and noise.....	43
3.iii Comparison with HgCdTe performance levels using Rule 07.....	52
3.iv Avalanche photodiodes for high sensitivities in long wavelength applications.....	53
(4) Experimental methods and modelling.....	62-85
4.i Molecular beam epitaxy.....	62
4.ii Hall effect measurement.....	68
4.iii X-ray diffraction (XRD).....	70
4.iv Device processing.....	72
4.v Characterisation techniques.....	77
4.vi Modelling.....	80
(5) Results and Discussion I – IMF Arrays.....	86-102
5.i Growth of GaSb IMF <i>p-i-n</i> diodes.....	86
5.ii XRD and transmission electron microscopy (TEM) characterisation of GaSb IMF <i>p-i-n</i> diodes.....	88
5.iii Electrical and optoelectronic characterisation of GaSb IMF <i>p-i-n</i> diodes.....	94
5.iv Discussion.....	98
(6) Results and Discussion II – <i>nBn</i> detectors for Mid-Infrared applications.....	103-128
6.i Growth of <i>nBn</i> detector samples.....	103
6.ii Characterisation of <i>nBn</i> detector samples.....	107
6.iii The effects of absorption layer doping upon <i>nBn</i> detector performance.....	118
6.iv Longer-wavelength <i>nBn</i> detector sample.....	120
6.v 1/f noise characterisation of primary <i>nBn</i> detector samples...	122

6.vi Discussion.....	124
(7) Results and Discussion III – Extended wavelength APDs.....	129-145
7.i Growth of extended wavelength APDs.....	129
7.ii IV and CV characterisation of extended wavelength APDs..	130
7.iii Determination of multiplication.....	133
7.iv Excess noise measurement.....	137
7.v Excess noise results.....	139
7.vi Discussion.....	143
(8) Conclusions and further work.....	146
Appendix I – Constants for bandstructure modelling.....	151
Appendix II – Spectral response model.....	152

List of common symbols

μ	Absorption coefficient
A	Area
E_g	Bandgap
Δf	Bandwidth
k	Boltzmann Constant
C	Capacitance
T_0	Characteristic Temperature
h_c	Critical thickness
J	Current density
IV	Current voltage measurement
JV	Current-density voltage measurement
w	Depleted volume width
ϵ_r	Dielectric constant (relative)
ξ	Electric field
q	Elementary charge
F	Excess Noise factor
E_f	Fermi Energy
M	Gain
n_i	Intrinsic carrier concentration
α	Ionisation coefficient for electrons
β	Ionisation coefficient for holes
k_{eff}	Ionisation coefficient ratio
E_{th}	Ionisation threshold energy
a_0	Lattice Constant
I^2	Noise current
ϵ_0	Permittivity of free space
h	Planck Constant
I_0	Primary photocurrent
η	Quantum Efficiency
R	Resistance

$R_d A$	Resistance-area product (dynamic)
$R_0 A$	Resistance-area product (zero-bias)
D^*	Specific Detectivity
c	Speed of light in a vacuum
Δ_0	Spin orbit split-off energy
ϵ	Strain
T	Temperature (in Kelvin)
λ	Wavelength

Abstract

Using the interfacial misfit (IMF) array growth mode, GaSb p-i-n diodes were grown on Si and GaAs lattice-mismatched substrates by molecular beam epitaxy (MBE) under optimised growth conditions. For the sample grown on Si, an AlSb nucleation layer was used to reduce the occurrence of twinning defects. In addition to the samples grown on mismatched substrates, an equivalent structure was further grown on a native GaSb substrate, for comparison. X-ray diffraction (XRD) was used to demonstrate that the layers were fully relaxed, and transmission electron microscopy (TEM) imaging showed arrays of 90° misfit dislocations with measured periodicities in agreement with atomistic modelling. However, after processing, device dark current densities of 0.9 Acm^{-2} and 0.18 Acm^{-2} were recorded for the sample grown on Si and the sample grown on GaAs, respectively, at -1.0 V and 300 K . These were compared to the sample grown on native GaSb, which had a dark current density of 0.01 Acm^{-2} under the same conditions. Furthermore, TEM analysis revealed relatively high threading dislocation densities (TDDs) of $\sim 10^8 \text{ cm}^{-2}$. It was proposed that not all the interfacial strain could be accommodated by the IMF arrays, since the array periods (9:8 for AlSb/Si and 13:14 for GaSb/GaAs) were not in exact agreement with ratio of the lattice constants (of AlSb to Si and GaSb to GaAs), i.e. a population of 60° misfit dislocations was still formed.

It was therefore decided to investigate the use of nBn detector structures as lattice mismatched photodetectors. Using a design based on an InAsSb bulk-material absorber, a comparison was again drawn between two samples, one grown on mismatched GaAs and a second grown on native GaSb. This time, device dark current densities were found to be relatively similar when comparing the two samples ($1.6 \times 10^{-5} \text{ Acm}^{-2}$ vs $3 \times 10^{-6} \text{ Acm}^{-2}$ at 200 K). D^ performance figures were also found to be within one order of magnitude ($1.5 \times 10^{10} \text{ cmHz}^{1/2}\text{W}^{-1}$ vs $9.8 \times 10^{10} \text{ cmHz}^{1/2}\text{W}^{-1}$ at 200 K). Furthermore, diffusion limited pe-*

formance was exhibited at all temperatures tested, so that the effects of Shockley Read Hall (SRH) generation were established to be absent (or at least much less significant). It was also found that absorption layer doping of around $\sim 4 \times 10^{17} \text{ cm}^{-3}$ was necessary to ensure diffusion limited performance for the sample grown on GaAs and that, with this modification, diffusion limited performance was achieved even for a sample with a highly lattice-mismatched absorption layer (with higher Sb content and longer cut-off wavelength).

While nBn detector structures offer very low dark currents, it will sometimes be necessary to have a detector which is sensitive to very weak signals. In telecoms applications, avalanche photodiode (APD) structures are often used as receivers for long-haul fibre optic systems. However, relatively few avalanche photodiode designs exist for wavelengths beyond $1.55 \mu\text{m}$. Two novel separate-absorption-and-multiplication (SAM) APD structures were therefore demonstrated based on the IMF growth mode. In particular, by transitioning the lattice from 5.65 \AA to 6.09 \AA , it was possible to combine GaSb absorption layers with GaAs and (for improved noise performance) $\text{Al}_{0.8}\text{Ga}_{0.2}\text{As}$ multiplication layers. Multiplication profiles were established using capacitance voltage modelling (together with ionisation coefficients from the literature) and excess noise measurements were then carried out. Through the presence of $1.55 \mu\text{m}$ photocurrent, it was confirmed that absorption took place in the GaSb regions, with transport to the p-n junction (in the multiplication region) taking place by diffusion. Through measurements showing $0.2 < k_{eff} < 0.4$ and $0.1 < k_{eff} < 0.2$ it was confirmed that multiplication of the photocurrent took place in the GaAs and $\text{Al}_{0.8}\text{Ga}_{0.2}\text{As}$ layers. Extension of the designs for sensitivity at longer wavelengths would then be possible using other absorption layer materials which are lattice matched to GaSb. It should be noted that these include InGaAsSb (short-wave infrared) InAsSb (mid-wave infrared) and strained layer superlattices based on InAs/GaSb or InAs/InAsSb (long-wave infrared).

(1) Introduction

At present, commercially available sensors and focal plane arrays (FPAs) working in the mid-wave infrared (MWIR) spectral range (3 – 5 μm) are predominantly based on HgCdTe alloy materials.¹ InAs and InSb detectors are also available commercially, but the latter always require cooling to 77 K for operation. However, devices based on quantum structured III-V designs, such as quantum well infrared photodetectors (QWIPs) and quantum dot infrared photodetectors (QDIPs) have been developed as alternatives.¹ Table 1 compares the specific detectivity (D^*), cut-off wavelength and operating temperature for commercial HgCdTe, InAs and InSb detectors from Teledyne Judson and Vigo S.A., as well as for QWIP detectors from Jet Propulsion Laboratory (JPL). Ultimately, HgCdTe has remained the “market leader”, being employed almost exclusively by military end-users,² as well as commercial users. While thermoelectrically cooled HgCdTe sensors are widely available, HgCdTe inherently suffers from certain disadvantages, notably fragility due to the weak HgTe bond strength, poor compositional uniformity and the additional cost associated with these factors. There is therefore an identified need for alternative detector designs which can be operated under thermoelectric cooling (200 – 240 K) and grown and processed more cheaply than HgCdTe. As commented earlier, novel structures based on III-V materials are promising candidates for these purposes. The primary application for infrared sensors is thermal imaging, e.g. famously for “hotspot” in test match cricket – where small changes in temperature are mapped to show contact between bat and ball – or for target acquisition in defence applications.² Further applications include the sensing of toxic or pollutant gasses.³ Such gasses often have absorption lines in the MWIR, e.g. methane (3.3 μm), CO₂ (4.2 μm), and CO (4.6 μm), permitting gas detection systems based on spectral “fingerprints”. New detectors are required to complement recently-developed MWIR laser sources (with improved power and tunability) for these applications.⁴ Detectors with competitive performance metrics (see Table 1) are required for both thermal imaging and

Technology	Operating temperature	Cut-off wavelength	D*	Reference
InSb	77 K	5.5 μm	$9 \times 10^{10} \text{ cmHz}^{1/2} \text{ W}^{-1}$	[5]
InAs	233 K	3.5 μm	$3 \times 10^{10} \text{ cmHz}^{1/2} \text{ W}^{-1}$	[6]
HgCdTe	230 K	3.5 μm	$6 \times 10^{10} \text{ cmHz}^{1/2} \text{ W}^{-1}$	[7]
QWIP	95 K	5.5 μm	$5 \times 10^{11} \text{ cmHz}^{1/2} \text{ W}^{-1}$	[8]
QWIP	77 K	9 μm	$9 \times 10^{10} \text{ cmHz}^{1/2} \text{ W}^{-1}$	[8]

Table 1: Examples of some mid-wave infrared detector products available commercially.

gas sensing, i.e. subtle differences in the incident photon flux must be resolved.

At the same time, designs for heterostructures based on III-V materials are usually constrained through the requirement for lattice matching to a “native” substrate. The manufacture of GaAs and InP substrates has matured so that larger areas (>3” diameter) and semi-insulating varieties are available.⁹ However, Sb-bearing compounds, e.g. InAsSb, are typically required for sensitivity in the MWIR spectral range – that is to say their bandgap is small enough that photons with wavelengths between 3 - 5 μm can be absorbed by bulk material. Bulk InAsSb material is typically grown lattice matched to GaSb – lattice constant 6.1 \AA – and cannot be grown lattice matched to GaAs – lattice constant 5.65 \AA . (While QWIPs or QDIPs detectors operating in the MWIR can be grown on GaAs, devices based on bulk materials are simpler to grow and typically offer higher responsivities). However, GaSb substrates have a cost around six times greater⁹ than GaAs substrates and are not available in the largest areas or in semi-insulating varieties. Clearly therefore, it would be beneficial to grow MWIR bulk materials on GaAs substrates. However, the lattice mismatch between GaSb and GaAs is large (7.78%) and the result of this is the inevitable occurrence of threading dislocations which propagate into the electrically active overlayers. These tend to impact device performance significantly. In recent years, workers at the Department of Electrical Engineering at UCLA have claimed progress in the direct growth of GaSb on GaAs.¹⁰ Through the interfacial misfit (IMF) array growth technique – details of which will be explored in the following chapters – epilayers capable of supp-

orting high quality device layers with low ($<10^6 \text{ cm}^{-2}$) threading dislocation densities (TDDs) have been reported.¹¹

In this work, IMF arrays were used to grow 6.1 Å-lattice-constant materials on GaAs substrates without the need for a thick metamorphic buffer (250 – 500 nm buffer thickness). The first key objective of this work was to verify the quality of the material grown, in terms of the TDD, and in terms of the effects of this TDD on device performance.

In order to investigate the material quality achievable under IMF growth, simple *p-i-n* diodes were grown in Section (5). These were based both on GaSb/GaAs and GaSb/AlSb/Si mismatched epitaxy. A lattice matched structure (on GaSb) was also grown for comparison. Cross-sectional transmission electron microscopy (TEM) was used to characterise the material quality in each case. Electrical characterisation of processed devices was also carried out. It was found that defect density levels were significantly greater than those quoted by ref [11]. Electrical performance was also compromised, with 300 K dark current densities increasing (by comparison with the sample on GaSb) by factors of ~15 and ~80, for the GaSb/GaAs case and for the GaSb/Si case, respectively. Nevertheless, arrays of pure-edge dislocations (i.e. IMF arrays) were clearly visible in TEM imaging. In accordance with the literature, the array periodicities were further noted to be in good agreement with the ratio of the lattice constants of the epilayer and substrate materials. Full relaxation of the GaSb overlayers was also confirmed through XRD Bragg scans.

*Once the effects of the TDD for IMF growth upon device performance had been determined for simple *p-i-n* structures, it was decided to investigate whether these effects could be suppressed through the use of an *nBn* structure. The second key objective of this work was to determine the defect tolerance of the *nBn* detector design, and hence the suitability of the *nBn* detector to the IMF growth mode.*

nBn detector structures aim to exploit the absorption properties of a narrow-bandgap material, but at the same time achieve the dark current behaviour associated with diffusion currents, rather than Shockley Read Hall (SRH) or surface currents. *nBn* detectors were grown on both GaAs substrates (via an IMF array) and on native GaSb substrates in Section (6). It was therefore possible to assess the impact of the choice of a mismatched substrate on the final detector performance, and in particular to determine whether SRH and surface currents – which were found to be troublesome for the case of GaSb *p-i-n* devices – could be suppressed. As will be seen in the following chapters, a synergy was found to exist between the IMF growth mode and the *nBn* detector design, so that only moderate changes in the dark currents (around a factor of 5 at 200 K) occurred as a result of the choice of a mismatched substrate. Furthermore, surface leakage and SRH currents were found to be almost entirely absent (for device diameters between 50 – 800 μm). The potential for FPAs operating with thermoelectric cooling based on these structures was highlighted through specific detectivity calculations and noise measurements. Specific detectivity was found to be greater than $10^{10} \text{ cmHz}^{1/2}\text{W}^{-1}$ at 200 K for devices grown on both GaAs and GaSb, with cut-off wavelengths of $\sim 3.5 \mu\text{m}$ measured at the same temperature.

In the final part of this work, IMF arrays were exploited to create separate-absorption-and-multiplication avalanche photodiodes (SAM-APDs). These were based upon previously-impossible GaSb/GaAs and GaSb/GaAs/AlGaAs heterostructures. The key objective of this section was to determine whether such structures still exhibited the excess noise characteristics of the wide bandgap regions, whilst at the same time being photosensitive at $1.55 \mu\text{m}$.

While *nBn* detectors were investigated to determine their suitability for 2D arrays, sometimes there will be a need for a detector with higher sensitivity, i.e. for applications where very low photon fluxes need to be measured. In Section (7), SAM-APD structures based on IMF interfaces were extensively characterised, through excess noise measurements and comparison with

results from a proprietary random path length model with full field dependence. It was found that the excess noise behaviours exhibited were consistent with multiplication occurring in the wide bandgap material, i.e. that effects due to multiplication in the absorption layers or at the IMF interface were absent, whilst the devices were also photosensitive at 1.55 μm . Gains in excess of 10^3 were established for the sample with an AlGaAs multiplication region. These designs could be extended to incorporate absorption layers consisting of other materials lattice matched to GaSb (e.g. InAsSb or InGaAsSb), allowing operation beyond 1.7 μm . Single-photon devices would also be possible, by using a GaAs multiplication region.

The above noted demonstrations of lattice-mismatched photodetectors operating in the infrared spectral range aim to highlight significant new avenues of research. The combination of mismatched growth techniques with specially designed heterostructures, suppressing the effects of threading dislocations upon the dark current density, could lead to high performance, low-cost and large-area detectors and FPAs being made available commercially on GaAs (or even Si) substrates. These would be capable of operation at higher temperatures, acting as competition for HgCdTe. Further work is suggested, including the growth of two-colour nBn detectors based on strained layer superlattice (SLS) absorption regions, and the development of the SAM-APD design to incorporate a MWIR absorber.

References

- [1] A. Rogalski, J. Antoszewski and L. Faraone, *J. Appl. Phys.* 105, 091101 (2009)
- [2] I. M. Baker, S. S. Duncan and J. W. Copley, in *Proc. SPIE* 5406, 133 (2004).
- [3] A. Krier, M. Yin, V. Smirnov, P. Batty, P. J. Carrington, V. Solovev, and V. Sherstnev, *Phys. Stat. Sol. (a)* 205, 1, 129–143 (2008).
- [4] G. R. Nash, S. J. B. Przeslak, S. J. Smith, G. de Valicourt, A. D. Andreev, P. J. Carrington, M. Yin, A. Krier, S. D. Coomber, L. Buckle, M. T. Emeny, and T. Ashley, *Appl. Phys. Lett.* 94 091111 (2009).
- [5] “Indium Antimonide detectors”, Teledyne Judson Technologies (March 2003).
- [6] “Indium Arsenide detectors”, Teledyne Judson Technologies (March 2003).
- [7] “PV-2TE Series 2 – 12 μm IR Photovoltaic Detectors Thermoelectrically Cooled”, VIGO System S.A. (2015).
- [8] S. D. Gunapala, S. V. Bandara, J. K. Liu, C. J. Hill, S. B. Rafol, J. M. Mumolo, J. T. Trinh, M. Z. Tidrow and P. D. LeVan, *Semicond. Sci. Technol.* 20, 473 (2005).
- [9] web page <http://www.wafertech.co.uk/products>
- [10] S. H. Huang, G. Balakrishnan, A. Khoshakhlagh, A. Jallipalli, L. R. Dawson, and D. L. Huffaker, *Appl. Phys. Lett.* 88, 131911 (2006).
- [11] S. Huang, G. Balakrishnan, and D. L. Huffaker, *J. Appl. Phys.* 105, 103104 (2009).

(2) Background Theory

Essential concepts in the design and characterisation of infrared photodetectors are covered in this section to provide a basis for understanding the results presented in sections 5-7. These include carrier generation/dark current mechanisms, electrostatic behaviour in p-n junctions and the impact ionisation process (as occurring in avalanche photodiodes). Figures-of-merit and bandstructure and critical thickness modelling are also treated.

i) Dark current Mechanisms

Dark currents are defined as currents that flow in a photodiode without illumination. These usually depend on the applied bias. All photodiodes suffer from dark currents to some extent, and their reduction is the focus of much effort – whether through choice of materials, heterostructure design, passivation techniques, or other avenues. By minimising the dark currents of a detector for a given signal level, the signal to noise ratio is maximised. Dark currents can occur via various mechanisms.

CHCC (Conduction-Hole-Conduction-Conduction) Auger generation occurs via the collision of a highly energetic conduction band electron with a second electron residing in the valence band. The collision results in the excitation of the valence band electron into the conduction band, with a mobile hole left behind. The process is illustrated in Figure 2.1. The CHCC Auger process is analogous to the impact ionisation process (which will be treated later in this section) but occurs even in the absence of electric field (at a lower rate). The CHCC process is known to dominate (over the other Auger processes) in direct-bandgap *n*-type semiconductors.¹ Carriers generated in the neutral regions of a photodetector via the CHCC Auger process (or the CHLH or CHSH processes for holes) diffuse into the electric field, where they undergo drift, resulting in dark current. The process is strongly temperature

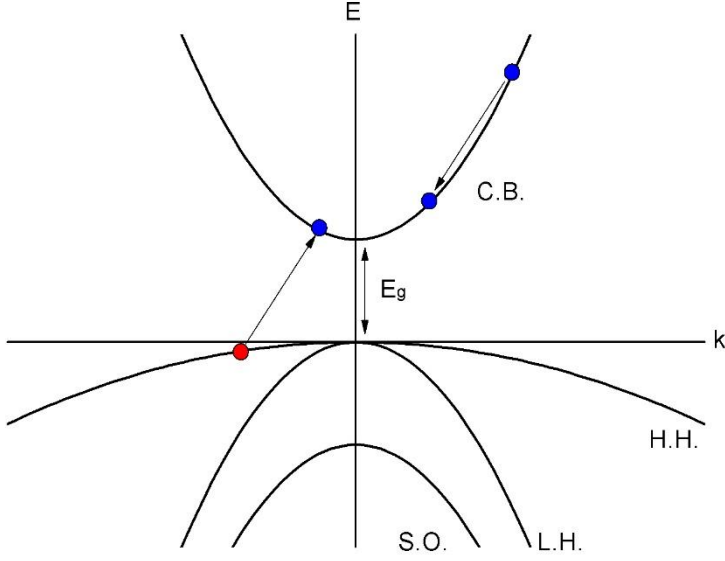


Figure 2.1: CHCC Auger process illustrated in an E-k diagram. C.B., H.H., L.H. and S.O. indicate the conduction band, heavy hole band, light hole band and the spin orbit split-off band, respectively.

dependent, via a dependence on the square of the intrinsic carrier concentration, n_i^2 , itself depending exponentially on the ratio of the full bandgap to kT ,²

$$J_{\text{diff,p}} = q \sqrt{\frac{D_p}{\tau_p}} \frac{n_i^2}{N_d} = q \sqrt{\frac{D_p}{\tau_p}} \frac{1}{N_d} N_c N_v \exp\left(-\frac{E_g}{kT}\right) \quad (2.1)$$

where q is the elementary charge, D_p is the hole diffusion coefficient, τ_p is the minority carrier lifetime, N_d is the donor concentration on the n -type side of the junction, N_c and N_v are the density of states for the conduction and valence bands, respectively, T is temperature, k is the Boltzmann Constant, and E_g is the bandgap. The above expression refers to the diffusion current due to minority carrier holes diffusing into the electric field from the n -type neutral region. An equivalent expression for electrons diffusing from an p -type neutral region, i.e. $J_{\text{diff,n}}$, can be written in terms of D_n , τ_n and N_A , the diffusion constant and lifetime for electrons

and the acceptor level in the p -type region. One term or the other will dominate for p - n junctions with asymmetric doping. For p - i - n diodes with an n -type intrinsic region, e.g. unintentionally doped InAs(Sb), diffusion currents result from holes diffusing from the (low n -type) intrinsic region into the field region or electrons diffusing from the p -type neutral region. In order to obtain to determine whether the diffusion mechanism is the dominant source of dark current in a particular device, it is common to plot the dark current density as a function of inverse temperature, and then to use a fitting to the following formula to determine the activation energy, E_a

$$J_{\text{diff}} \propto n_i^2 \propto T^3 \exp\left(\frac{-E_a}{kT}\right) \quad (2.2)$$

which is a reduced form of Equation 2.1, in which the temperature dependence of $N_c N_v$ is assumed to be proportional to T^3 . If this energy is equal to the full, low temperature bandgap of the neutral-region semiconductor, diffusion currents are expected to be dominant.

Trap states occur due native defects or threading dislocations in the crystal lattice. These can result in generation-recombination (G-R) currents.³ Trap states contain either an electron (when occupied) or a hole (when vacant). Shockley Read Hall (SRH) currents occur when electrons move via a trap state located within the bandgap from the valence band to the conduction band. The efficiency of the SRH process is energetically favoured for trap states lying close to the middle of the bandgap. For this reason, the SRH process is also maximised when the Fermi level lies close to the middle of the bandgap, i.e. for intrinsic layers. On the other hand, extrinsic doping pins the Fermi level close to the band edge, so that SRH generation is suppressed in the neutral regions. The process can be encouraged by the presence of electric field, though it may still occur for zero field. SRH currents dominate below a certain temperature, referred to as T_0 , which is a function of the material type and quality, among other factors. The rate at which SRH generation occurs is given by²

$$U = - \left[\frac{\sigma_p \sigma_n v_{th} N_t}{\sigma_n \exp\left(\frac{E_t - E_i}{kT}\right) + \sigma_p \exp\left(\frac{E_i - E_t}{kT}\right)} \right] n_i = - \frac{n_i}{\tau_{eff}} \quad (2.3)$$

where σ_p and σ_n are the hole and electron capture cross-sections, respectively, N_t is the density of traps, $v_{th} = \sqrt{3kT/m^*}$ is the average thermal velocity for carriers where m^* is effective mass, E_t the trap energy level and E_i is the intrinsic Fermi level. τ_{eff} is thus defined as the effective lifetime. The increased efficiency of the SRH process for traps with energies close to the Fermi level can be shown by varying $E_i - E_t$ in Equation 2.3. The resulting current density due to SRH generation is then given by²

$$J_{SRH} = \int_0^W q|U| dx = q|U|W = \frac{qn_i W}{\tau_{eff}} \quad (2.4)$$

where w is the width of the electric field region. Under the SRH dark current limited regime, the magnitude of the dark current density is therefore directly proportional to the intrinsic carrier concentration, so that Equation 2.4 can be rewritten as

$$J_{SRH} = \frac{qW}{\tau_{eff}} \sqrt{N_c N_v} \exp\left(-\frac{E_g}{2kT}\right) \quad (2.5)$$

where, once again, the temperature dependence of the density of states can again be approximated to be proportional to T^3 yielding the following expression for fitting.

$$J_{SRH} \propto n_i \propto T^{3/2} \exp\left(\frac{-E_g}{2kT}\right) \quad (2.6)$$

Figure 2.2 shows the relative magnitude of the diffusion and SRH components of the dark current density as modelled for an InAs *p-i-n* diode (calculated using Equations 2.1 - 2.6). Approximate values $N_c = 8.7 \times 10^{16} \text{ cm}^{-3}$ and $N_v = 6.6 \times 10^{18} \text{ cm}^{-3}$, $D_p = 13 \text{ cm}^2 \text{ s}^{-1}$, $D_n = 1000 \text{ cm}^2 \text{ s}^{-1}$, $\tau_n = 3 \times 10^{-8} \text{ s}$ and $\tau_p = 3 \times 10^{-6} \text{ s}$ were taken from [4]. The unintentional *n*-type doping in the intrinsic region was assumed to be 10^{15} cm^{-3} and the width of

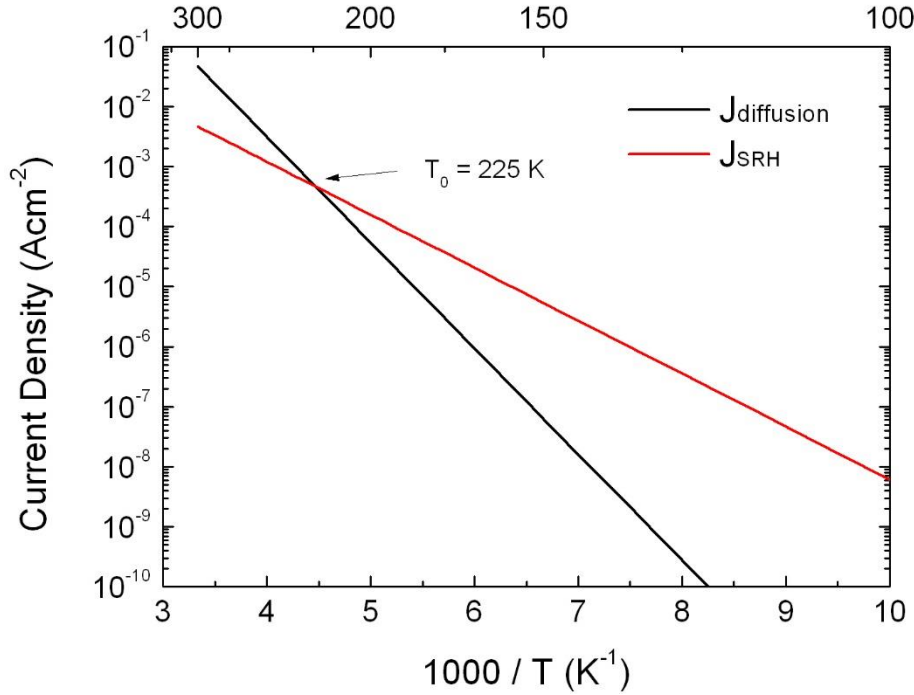


Figure 2.2: Modelled temperature dependence of the diffusion and SRH dark current contributions for an InAs *p-i-n* diode.

the depletion region was assumed to be 1 μm (corresponding to -0.2 V applied bias). It can be seen that $T_0 \approx 225$ K. For the case of an elevated trap density, as would be expected for lattice-mismatched growth, J_{SRH} , which is proportional to the trap density, would be increased further. In addition, surface leakage currents need to be considered.

Surface leakage currents are often a significant problem when designing infrared photodetectors. A *surface inversion layer* is a thin region at the surface of a semiconductor with the opposite majority carrier type to the bulk. These can occur due to dangling bonds.⁵ Surface inversion layers can act as a shunt resistance bypassing the bulk junction. *n*-type surface inversion layers can occur in *p*-InAs(Sb) layers in particular, and these result in a conducting channel. Surface leakage currents are approximately temperature insensitive and generally result in Arrhenius plots exhibiting small activation energies. Passivation using dielectrics, e.g. SU-8, have been reported to successfully reduce surface leakage currents, even by orders of

magnitude.⁵ Smaller devices are more susceptible to surface leakage effects, due to increased perimeter to area ratio. In order to determine whether processed devices are surface current limited (or bulk limited), it is useful to plot the current density for a series of mesa areas. Area scaling of the dark currents indicates that surface leakage currents are less significant, whereas scaling with the device perimeter indicates that surface leakage currents are dominant.

ii) Capacitance-voltage measurements

When two semiconductor layers with opposite doping types meet, a $p-n$ junction is formed. $p-n$ junctions in semiconductor materials result in opposing drift and diffusion processes taking place. In a $p-i-n$ diode, as illustrated in Figure 2.3, majority carriers from the p -type and n -type neutral regions diffuse into the intrinsic layer (where the carrier population is low) and recombine with each other. This leads to an imbalance of charge due to the ionised dopant atoms, which are immobile and remain in the neutral regions. The charge imbalance creates an electric field, resulting in a drift current which opposes the diffusion current. In the initial state, the diffusion process is stronger than the drift process and, as more carriers recombine, a space charge region (SCR) forms, devoid of mobile carriers. The electric field remains after the two processes have reached equilibrium, forming a built-in potential. The SCR, together with the p -type and n -type neutral regions are analogous to a parallel plate capacitor. The capacitance is given by $C = \epsilon_0 \epsilon_r A/w$, where ϵ_0 and ϵ_r are the permittivity of free space and the relative permittivity (of the semiconductor), respectively, A is the junction area and w the width of the space charge region. In fact, the SCR does not begin and terminate abruptly, since the diffusion profile of carriers has a “rounded” profile, however it is common to use the “full-depletion approximation”.⁶ This effectively considers that the SCR has a definite width, given under the assumption that the diffusion profile is abrupt. As increasing reverse bias is applied across the device, the SCR expands. In photodiodes, the

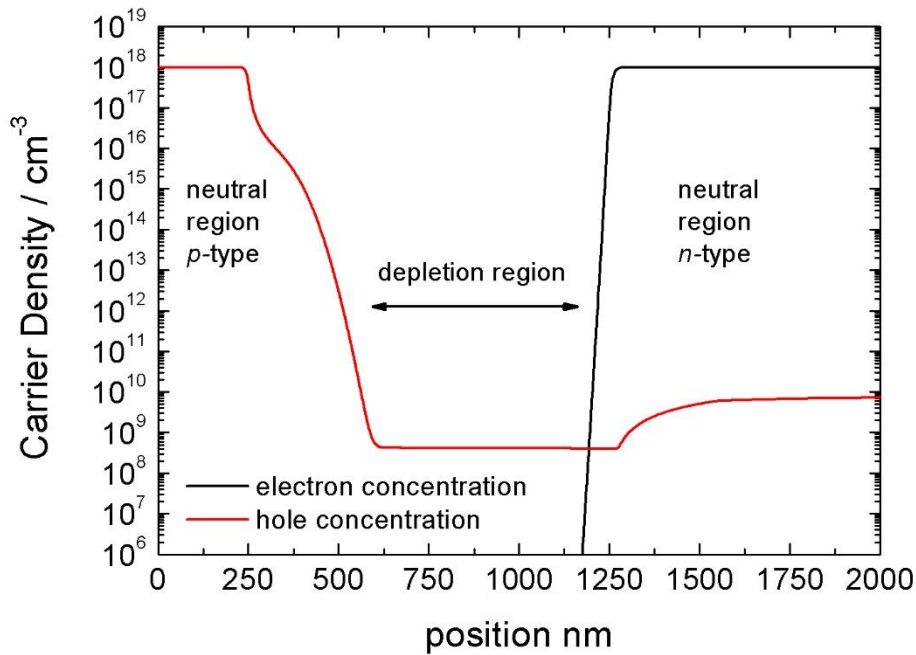


Figure 2.3: Modelled carrier populations, as a function of position, in a GaSb *p-i-n* diode (with Te compensation doped intrinsic region) under -5.0 V bias.

quantum efficiency is generally dependent on the depletion width (i.e. the width of the SCR), since photogenerated carriers in the neutral regions must diffuse to the SCR for current to flow, and since the electron-hole pairs generated within the SCR are separated with the greatest efficiency. Knowledge of the depletion behaviour, as a function of bias, is therefore essential when designing photodiodes, and becomes paramount when designing more complicated heterostructures, e.g. SAM-APDs, where the electric field profile is of crucial importance. The SCR is more commonly known simply as “the depletion region” and will be referred to as such from here on.

Capacitance is typically measured using an LCR meter, e.g. the Agilent E4980A. The LCR meter measures the complex impedance of the device under test (DUT) for changing DC bias voltage (using an AC test signal) before internally calculating the other impedance parameters (resistance, reactance, conductance, susceptance, capacitance and inductance) via trigonometry.⁷ This work concentrates exclusively on capacitance measurements.

iii) Avalanche Photodiodes (APDs) and Impact Ionisation

Carriers moving within the depletion region of an avalanche photodiode (APD) can sometimes gain sufficient energy from the electric field to generate additional carriers by impact ionisation. In the impact ionisation process, electrons in the valence band are promoted to the conduction band by energetic primary carriers, leaving behind mobile holes. In this way, additional electron-hole pairs are generated.⁸ Each additional carrier generated can be accelerated by the field in the same way, and further electron hole pairs generated. In this way, carrier multiplication takes place. Figure 2.4 shows a current-voltage (IV) for an AlGaAs avalanche photodiode from Section (7). The steep rise in the current for bias conditions >10 V is due to the impact ionisation process, with an avalanche breakdown (i.e. an infinite multiplication condition) occurring at -11.25 V (though in practice the total current is limited by the contact resistance). The probability of ionisation is described by material-specific ionisation coefficients, which are functions of the electric field, ξ . Electrons and holes have separate coefficients, $\alpha(\xi)$ and $\beta(\xi)$, respectively. These have dimensions of cm^{-1} and $1/\alpha$ and $1/\beta$ are the mean ionisation path lengths. The impact ionisation process can be exploited by APDs to amplify weak signals, i.e. to produce gain. The gain, or multiplication, is equal to the total photocurrent divided by the primary photocurrent (i.e. the photocurrent without multiplication). It should be noted that the multiplication process amplifies not only the photogenerated signal, but also the dark currents. There is also an additional noise contribution, the “excess noise”, resulting from the stochastic nature of the impact ionisation process, although much effort goes into reducing this.⁹ However, if the overall signal to noise ratio is limited by noise in the external circuit (e.g. thermal noise in an external amplifier), the use of an APD (with internal gain) can significantly increase the overall signal to noise ratio.⁸ Excess noise will be discussed in more detail in the following section.

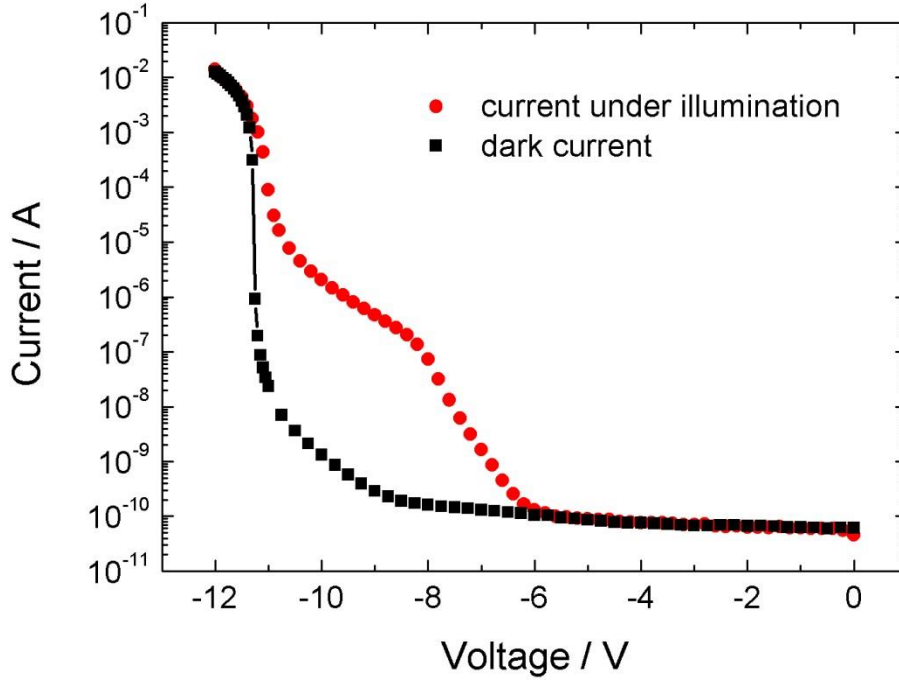


Figure 2.4: IV characteristics of an APD device, with breakdown occurring at -11.25 V.

iv) Noise

Electronic noise presents itself as random fluctuations in an electrical signal, and can result from various mechanisms. In photodetectors, these include the absorption of background radiation, as well as processes intrinsic to the device, such as the thermal agitation of carriers and the stochastic nature of the flow of individual electrons.

Thermal agitation of carriers results in thermal or “Johnson” noise.¹⁰ Thermal noise cannot be eliminated (other than at absolute zero) but reduces with temperature. The mean square value for the associated noise current is given by,

$$I_{\text{thermal}}^2 = 4kT\Delta f/R \quad (2.7)$$

where R is the resistance of the device, T is temperature and Δf is the measurement bandwidth. Thermal noise is approximately frequency independent.

Shot noise results from the discrete nature of electronic charge, which leads to the flow of current consisting of individual charges arriving at a given point in the circuit over time according to the Poisson Distribution.⁸ Shot noise is also approximately frequency independent. The mean squared shot noise current is generally taken to be

$$I_n^2 = 2q\bar{I}\Delta f \quad (2.8)$$

where q is the elementary charge, \bar{I} is the mean DC current. However, the mean DC current may differ from the total current flowing in the device, e.g. drift and diffusion currents still flow for zero bias, and so Shot noise is still present, despite zero total DC current flowing. Shot noise is temperature independent, though the flow of dark currents will vary with temperature, affecting the total shot noise current.

1/f noise is, as its name suggests, a type of noise with a magnitude with inverse frequency dependence. $1/f$ noise can occur due to traps at surfaces or heterointerfaces. When these traps are occupied, the electron and hole mobilities are locally modulated by the trapped charge, so that the trapping/detrapping process affect the total flow of current in the device.¹¹ $1/f$ noise is characterised by a “knee frequency” at which the spectral noise density of the $1/f$ component is equal to that of that of the white noise (as measured at higher frequencies). Below the noise knee frequency the $1/f$ component dominates. The trapping/detrapping time constants are reduced at lower temperatures, affecting the modulation and typically reducing the knee frequency.

Excess noise occurs due to the statistical nature of the impact ionisation process, as noted in the previous section. For the case that one of the ionisation coefficients (α or β) is zero, excess noise is eliminated, and gain simply increases exponentially with increasing electric field. In this case, no avalanche breakdown occurs and there is no limitation on bandwidth.⁸ Generally, both ionisation coefficients, α and β , are finite, leading to a positive feedback

characteristic. This can greatly amplify any initial fluctuations in current flow and lead to avalanche breakdown (i.e. infinite multiplication). Tager [1964] found that, for the condition that $\alpha = \beta$, the noise measured is greater than that for the condition where $\beta = 0$ by a factor equal to the multiplication, M .⁸ McIntyre developed this relation idea to allow for arbitrary values ratios of $k_{\text{eff}} = \beta/\alpha$ and found that, for low frequencies¹²

$$F = k_{\text{eff}}M + (1 - k_{\text{eff}}) \left(2 - \frac{1}{M}\right) \quad (2.9)$$

where F is the excess noise factor, so that the total noise current density, I_n^2 is given by

$$I_n^2 = 2qI_0MF\Delta f \quad (2.10)$$

where q is the elementary charge, I_0 is the primary photocurrent (i.e. the photocurrent for unity gain) and Δf is the measurement bandwidth. McIntyre's work is predicated on the "local model" of impact ionisation, which will be explored in the next section.

v) Limitations of the Local Model of impact ionisation

In practice, carriers accelerated by an electric field cannot initiate ionisation events until they attain the ionisation threshold energy, E_{th} .¹³ In doing so they undergo a certain displacement, referred to as the "dead space" which, in the *ballistic approximation*, is given by

$$d = E_{\text{th}}/q\xi \quad (2.11)$$

where ξ is the electric field. The effects of dead space are particularly pronounced at high electric fields, where the mean ionisation path length (which is just the inverse of the particular ionisation coefficient, $1/\alpha$ or $1/\beta$) is short. For high electric fields, the dead space can become a significant fraction of the ionisation path length. The effect of the dead space can be to reduce the excess noise factor, particularly in thin devices.¹³ As noted above, much of the theory surrounding APDs neglects the effects of dead space, which is reasonable under low

fields and/or in thick devices. However, it is possible to model multiplication and excess noise taking dead space into account. This is generally achieved using a random path length (RPL) model, or recurrence equations.¹⁴ In this work, the RPL approach will be used, with details to follow in the experimental section. The *ballistic approximation* considers that carriers are freely accelerated by the electric field and that no scattering occurs. As taken into account by analytical band Monte Carlo models, e.g. [15], scattering can have a significant effect on the fitted ionisation threshold energy, in other words the threshold energy fitted in a hard-threshold model (e.g. an RPL model) is always larger than that fitted in analytical band Monte Carlo.

vi) *Figures of Merit*

Certain *figures of merit* are commonly used to provide an indication of the performance of a particular device with respect to those found elsewhere, e.g. in the literature. Those employed most commonly in this work are outlined as follows.

Quantum efficiency is defined as the fraction of photogenerated electrons reaching the external circuit to the number of photons which arrive at the detector's surface. The number of photons per second, or photon flux, arriving at the detector, ϕ , can be calculated, in units of s^{-1} using the Planck Relation

$$\phi = \frac{P\lambda}{hc} \quad (2.12)$$

where P is the optical power, λ is the wavelength of the source, h is the Planck constant and c is the speed of light. The quantum efficiency, η , is found by dividing the photocurrent, I_{ph} , by the product of the photon flux with the elementary charge, $q\phi$.

The responsivity, R , of a detector is defined as the current generated per unit optical power incident on the detector surface, usually expressed in units of AW^{-1} . The responsivity is closely related to the quantum efficiency, and the two can be equated as follows.

$$R = \eta \frac{q\lambda}{hc} \quad (2.13)$$

It can be seen that the responsivity has an additional dependence on λ . This has implications for the D^* figure of merit, which can be calculated from R when the dark current density, temperature and dynamic resistance area product are known. The effect of this dependence is that the value of D^* measured increases as a function of the wavelength of the incident radiation (due to an increased photon flux per unit power of applied radiation).

The dynamic resistance-area product, $R_d A_d$, describes the dark currents of a detector normalised to the area of the device. Larger values indicate lower dark current densities. $R_d A_d$ can be calculated by differentiation of the dark current density, J , as a function of voltage, as follows.

$$R_d A_d = \left(\frac{dJ}{dV} \right)^{-1} = \frac{dV}{dJ} \quad (2.14)$$

The Noise Equivalent Power (NEP) describes the sensitivity of a photodetector and is defined as the incident power which produces a signal equal in magnitude to the noise.

Specific detectivity, or D^* , is a measure of detector performance inversely proportional to the NEP. It is normalised to the device area, A , and the measurement bandwidth, f .

$$D^* = \sqrt{A\Delta f}/\text{NEP} \quad (2.15)$$

D^* can also be calculated, assuming that shot noise and Johnson noise are the dominant noise sources, according to the following formula

$$D^* = R/\sqrt{2qJ + 4kT/R_d A_d} \quad (2.16)$$

where k is the Boltzmann constant (in JK^{-1}) and T is the device temperature. Equation 2.16 may be found by combining Equations 2.7, 2.8 and 2.15. It may be the case at low frequencies

that $1/f$ noise, as discussed earlier, becomes the dominant noise source, so that D^* figures calculated using Equation 2.16 may only be valid only at higher frequencies.

vii) *Bandstructure modelling*

The design and modelling of nBn detector structures in particular requires accurate knowledge of band alignments in III-V heterostructures. In this work, the method of Krijn¹⁶ was followed in order to model band alignments accounting for strain. The model of Krijn closely follows the earlier model of Van de Walle.¹⁷ Both models are based on so called “Model Solid Theory”, i.e. band alignments are calculated with respect to the average electrostatic potential in an infinite “model” solid. On the other hand, valence band reference levels can be taken from [18], which are defined with respect to the valence band position of InSb.

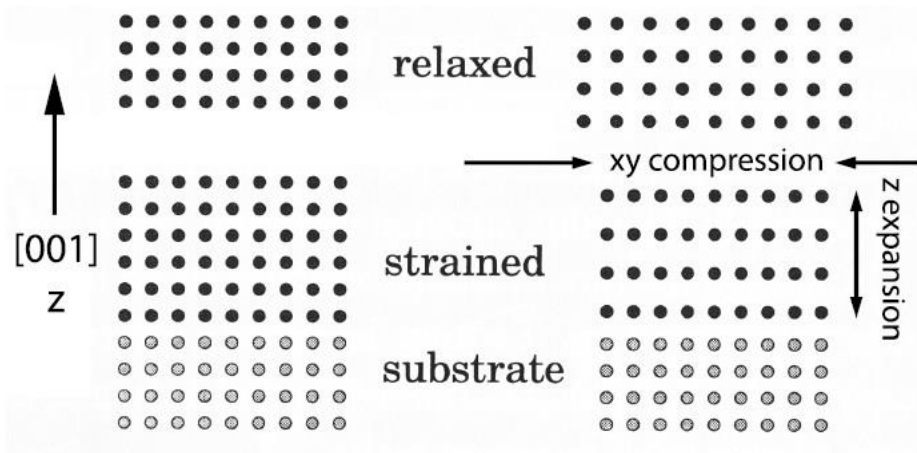


Figure 2.5: Diagram of a tetragonal distortion in a compressively strained epilayer, showing the change in the epilayer lattice constant, in the xy -plane ($a_{||}$) and in the z -direction (a_{\perp}).

Strained III-V layers undergo a *tetragonal distortion*, so that the in-plane lattice constant of the strained layer, $a_{||}$, deforms to match that of the substrate (or fully relaxed sub-layer), a_0 , i.e. $a_{||} = a_0$. In order to calculate the strain-induced shifts in the band edge energies, it is first necessary to calculate the in plane strain, $\epsilon_{||} = a_{||}/a_0 - 1$, where a_0 is the relaxed lattice con-

stant of the epilayer under consideration. The energy accrued or expended transforming the in-plane lattice constant is transferred to the perpendicular direction of the lattice, resulting in an expansion, as illustrated in Figure 2.5, (or, alternatively, a contraction) so that the perpendicular lattice constant is given by

$$a_{\perp} = a(1 - D(a_0/a - 1)) \quad (2.17)$$

where $D = 2c_{12}/c_{11}$, where c_{12} and c_{11} are the elastic constants of the epilayer. The perpendicular strain is then given by $\epsilon_{\perp} = a_{\perp}/a - 1$. The effect of the hydrostatic strain upon the valence band energy $\Delta E_{v,av}$ is then given by

$$\Delta E_{v,av}^{hy} = a_v(2\epsilon_{\parallel} + \epsilon_{\perp}) \quad (2.18)$$

and, similarly, the effect on the conduction band energy is given by

$$\Delta E_c^{hy} = a_c(2\epsilon_{\parallel} + \epsilon_{\perp}) \quad (2.19)$$

where a_v and a_c are the hydrostatic deformation potentials (material-specific proportionality constants which describe the effect of the change in the volume of the strained layer) for the valence band and for the conduction band, respectively. The effect of the hydrostatic strain can be explained in terms of the change in the overlap of the electron wave function in all three directions in the crystal, leading to an equal shift being applied to the positions of the band edges for the heavy hole (hh), light hole (lh) and spin-orbit split off (so) bands, respectively. The effect of the shear strain is to remove the degeneracy for the valence band, i.e. the hh and lh bands have different energies (at $k=0$) once strain is accounted for. The shear strain acts to change the wave function overlap in the z-direction, but also to change the wave function overlap in the x- and y-directions in an opposite manner. As a result, different energetic shifts in the band positions are applied for the hh and lh bands, and the degeneracy is removed. These are given by

$$\Delta E_{hh}^{sh} = -\frac{1}{2}\delta E^{sh} \quad (2.20)$$

$$\Delta E_{lh}^{sh} = -\frac{1}{2}\Delta_0 + \frac{1}{4}\delta E^{sh} + \frac{1}{2}\left(\Delta_0^2 + \Delta_0\delta E^{sh} + \frac{9}{4}(\delta E^{sh})^2\right)^{1/2}$$

$$\Delta E_{so}^{sh} = -\frac{1}{2}\Delta_0 + \frac{1}{4}\delta E^{sh} - \frac{1}{2}\left(\Delta_0^2 + \Delta_0\delta E^{sh} + \frac{9}{4}(\delta E^{sh})^2\right)^{1/2}$$

where Δ_0 is the spin orbit split off energy and δE^{sh} is given by

$$\delta E^{sh} = 2b(\epsilon_{\perp} - \epsilon_{\parallel}) \quad (2.21)$$

where b is the shear deformation potential (similar to the hydrostatic deformation potential, but for the shear strain) of the epilayer. Finally, E_v and E_c are found according to

$$E_v = E_{v,av} + \Delta_0/3 + \Delta E_{v,av}^{hy} + \max(\Delta E_{hh}^{sh}, \Delta E_{lh}^{sh}) \quad (2.22)$$

$$E_c = E_{v,av} + \Delta_0/3 + E_g + \Delta E_c^{hy}$$

where $\max(\dots)$ indicates that the larger value of the two bracketed values should be chosen, i.e. the uppermost of the lh and hh bands defines the band edge. Values for $E_{v,av}$ in ternary or quaternary alloys are sometimes simply interpolated from the respective binaries. However, it is also possible to use a bowing term, as suggested by [17],

$$E_{v,av} = xE_{v,av(A)} + (1-x)E_{v,av(B)} + \frac{x(1-x)(a_{v(A)} - a_{v(B)})(a_{0(A)} - a_{0(B)})}{a_{\parallel}} \quad (2.23)$$

where $a_{v(A)}$ and $a_{v(B)}$ are the deformation potentials for material A (with mole fraction x) and material B (with mole fraction $1-x$) and $a_{0(A)}$ and $a_{0(B)}$ are the unstrained lattice constants, respectively. It is explained in the reference that, within a ternary alloy, one of the binary alloys is effectively compressed whilst the other is under tension so that, even in the absence of total strain due to a mismatch with an underlying epilayer, there is still a shift in the average valence band position with respect to the (naïve) interpolated value.

The above calculations all assume (100) wafer orientation. Lattice constants for ternary and quaternary alloys are found using Vegard's law, i.e. linear interpolation. Values for E_g and Δ_0 in ternary and quaternary alloys should be found using appropriate bowing parameters from the literature using

$$E_g(ABC) = xE_{g(A)} + (1 - x)E_{g(B)} - \gamma_{E_g}x(1 - x) \quad (2.24)$$

and

$$\Delta_0(ABC) = x\Delta_{0(A)} + (1 - x)\Delta_{0(B)} - \gamma_{\Delta_0}x(1 - x) \quad (2.25)$$

where γ_{E_g} and γ_{Δ_0} are the bowing parameters for the ternary $A_xB_{1-x}C$ for the energy gap and the spin orbit split off band, respectively.

The above equations are rather cumbersome, and while it can be instructive to confirm initial results by working through them using a spreadsheet, these calculations were handled day-to-day using a Mathcad worksheet. All the constants and bowing parameters used can be found in Krijn's paper, and are also reproduced in Appendix I.

viii) Device structures

p-i-n photodiodes convert incident photons into electrical current through excitation of valence band electrons into the conduction band. Absorption occurs with a profile given by Beer's Law,¹⁹ so that the intensity of the propagating light, I , is given by

$$I = I_0 \exp(-\mu x) \quad (2.26)$$

where I_0 is the intensity of the incident light, μ is the absorption coefficient of the material (usually expressed in cm^{-1}) and x is the depth of propagation. Since the absorption profile is exponentially decreasing, the majority of the incident radiation is, in general, absorbed in the *p*-type region (for a diode with the *p*-type side facing the incident radiation) as shown in Figure 2.6 (for an absorption coefficient of $2 \times 10^4 \text{ cm}^{-1}$). Photogenerated minority carrier electrons then travel by diffusion to the intrinsic (depleted) region where they are swept away by the electric field. *n-i-p* configurations are also possible, though these are dependent on photocurrent from minority carrier holes, which usually have larger effective masses and shorter lifetimes than minority carrier electrons in *p*-type material, reducing quantum efficiency. However, *n*-type layers are less prone to surface inversion layers in InAs(Sb) (the surface inversion layer for InAsSb is itself *n*-type) and so surface currents may be reduced in the *n-i-p* configuration.

nBn photodetectors²⁰ also convert incident light into an electrical current, but use a thin, wide bandgap barrier layer in place of the intrinsic region. The barrier layer, typically AlAsSb, is designed using bandgap engineering, yielding a large conduction band offset with respect to the absorption layer – typically InAs – but a small or negligible valence band offset. As a result, the flow of dark currents due to majority carriers is blocked, but photogenerated

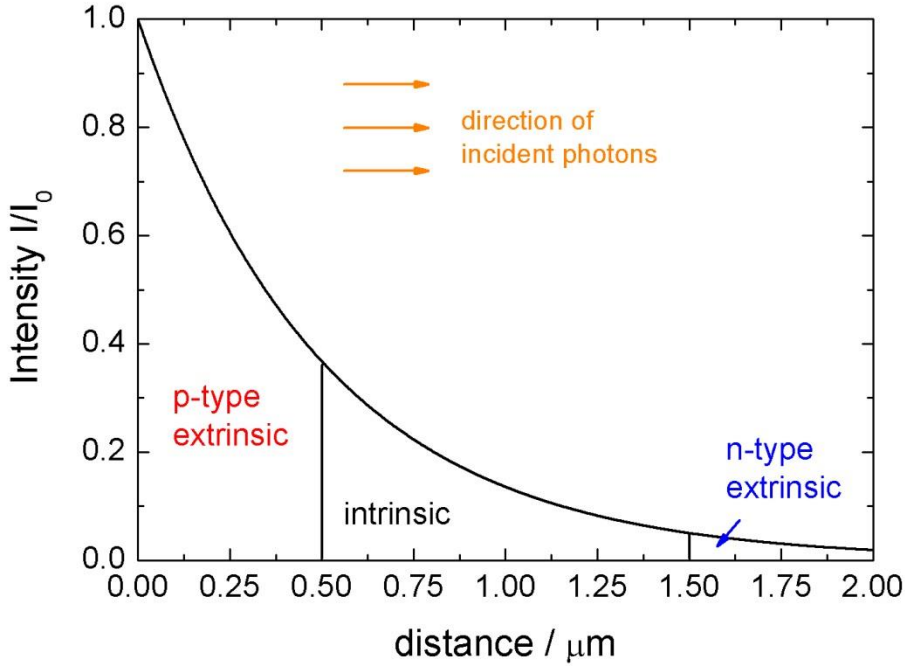


Figure 2.6: Intensity of propagating $1.55 \mu\text{m}$ radiation in an InAs diode, with $1 \mu\text{m}$ intrinsic region, according to Equation 2.26 (using an absorption coefficient from Ioffe⁴).

minority carriers flow freely, as illustrated in Figure 2.7. Generally, nBn detectors are tested under top-side illumination, i.e. radiation enters the detector from the right-hand-side of Figure 2.7, however reverse side illumination is also possible, and is preferred for focal plane arrays. Under a small applied operating bias, the electric field profile is concentrated across the barrier layer, rather than spreading into the narrow-bandgap absorption layer which is susceptible to field. As a result, SRH generation and band-to-band tunnelling processes are virtually eliminated by the nBn design. n -type doping in the absorption and contact layers further pins the Fermi level at the conduction band edge, away from mid-gap traps associated with SRH recombination. Finally, mesas are defined without etching through the barrier layer, creating a high shunt resistance for surface currents, which are also therefore almost eliminated by the nBn design. Figure 2.8 shows the same data that was presented in Figure 2.2, but for the case of an nBn photodetector. In this case, the diffusion current depends only on the contribution from holes in the absorption layer. It can be seen that T_0 is slightly

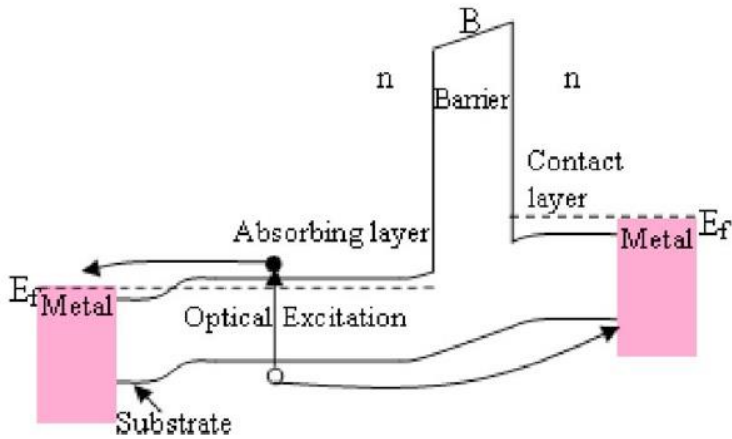


Figure 2.7: nBn band diagram showing the generation of an electron-hole pair and the free transport of holes (but not electrons) across the barrier layer.²⁰

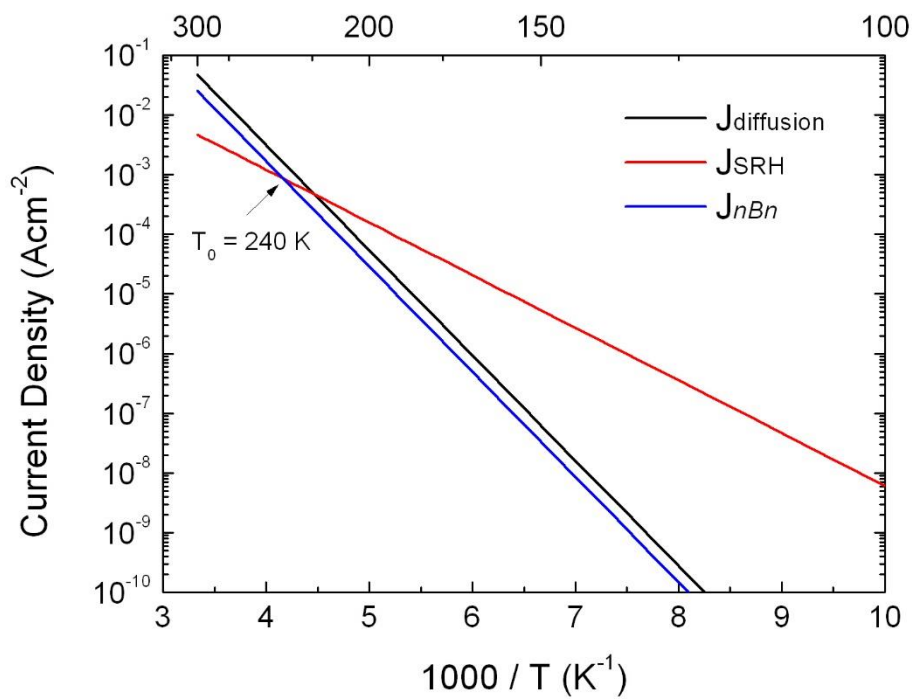


Figure 2.8: Shows the diffusion current for an InAs nBn detector in comparison with the diffusion and SRH currents for an InAs $p-i-n$ diode.

increased compared with the previous figure, at 240 K. The absorber was modelled with an n -type doping level of $1 \times 10^{16} \text{ cm}^{-3}$.

SAM-APD structures take advantage of the absorption properties of one material, i.e. a narrow bandgap, and the multiplication properties of a second material, i.e. low excess noise behaviour, low dark currents, and/or high multiplication.²¹ The two are separated by a charge sheet (heavily doped, thin layer) which allows for the confinement of the peak field to the multiplication layer, with only low field present in the absorber, as illustrated in Figure 2.9. Electron-hole pairs are generated in the absorption layer by excitation of electrons from the valence band into the conduction band, in the same way as for a p - i - n diode. Electrons (or holes for the case of an n -type absorber) are then transported by the electric field into the multiplication region, where gain occurs.

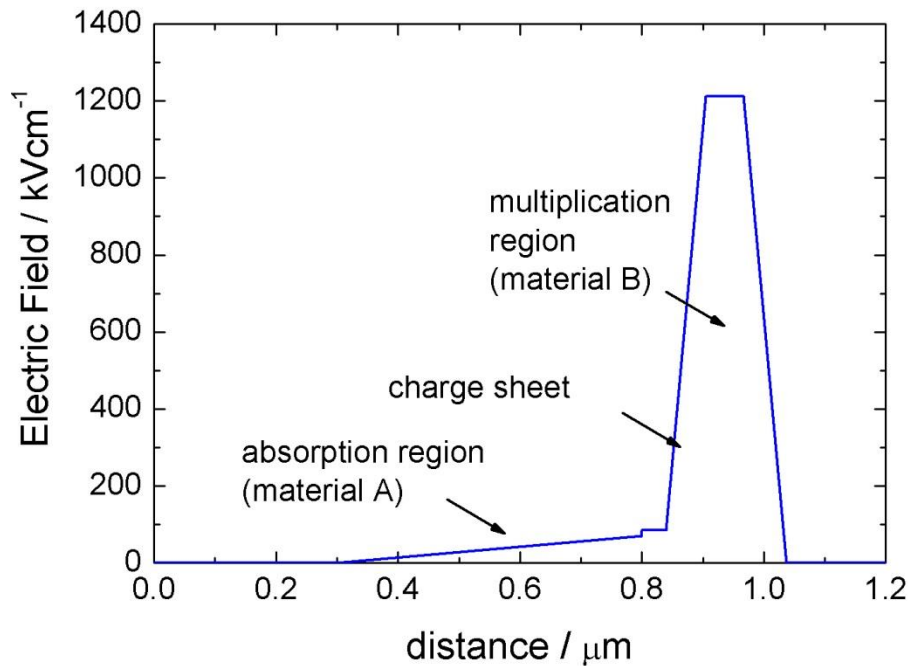


Figure 2.9: Electric field profile for a simple SAM-APD structure under operating bias, as calculated using the electric field model of Section (4), showing low field in the absorber (material A) and high field in the multiplication region (material B).

ix) Critical thickness modelling

Strain results from the growth of semiconductor epitaxial layers onto other layers with a different lattice constant. For small strains and thin layers, 2D planar growth proceeds, with the strain being accommodated through a tetragonal distortion of the overlayer. However, as the overlayer mismatch and or thickness increase, a critical thickness occurs, beyond which it is no longer possible to accommodate the strain in this way. The strain is then accommodated through faults in the crystal lattice known as dislocations. There are several models commonly used to calculate the critical thickness.^{22,23} According to Matthews and Blakeslee, the critical thickness, h_c , is given by²²

$$h_c = \frac{b \left(1 - \frac{\nu}{4}\right)}{4\pi\phi(1 + \nu)} \left(\ln\left(\frac{h_c}{b}\right) + 1\right) \quad (2.27)$$

where ν is Poisson's ratio for the epilayer, b is the Burger's vector and ϕ is the natural misfit, which is given according to

$$\phi = \frac{|a - a_0|}{\frac{1}{2}(a + a_0)} \quad (2.28)$$

where a is the relaxed lattice constant of the epilayer, and a_0 is the lattice constant of the substrate. The model of Matthews and Blakeslee was derived using a force balance approach, considering the epitaxial strain to be the "driving force" counteracted by the tension due to misfit dislocations. More recently, People and Bean derived a second model based on comparing the energies of the strained layer and the misfit dislocations, respectively. In principle, the two approaches should give identical results (since both force balance and energy minimisation are fundamental concepts of Physics).²⁴ However, it is suggested in [24] that People and Bean effectively considered a fixed dislocation density and a critical thickness at which all the strain in the epilayer is replaced by misfit dislocations catastrophically, rather than considering

the thickness at which the strain is first relieved through threading dislocations. According to People and Bean, the critical thickness is given by²³

$$h_c = \frac{b^2(1 - \nu)}{16\pi\sqrt{2}\phi^2 a(1 + \nu)} \ln\left(\frac{h_c}{b}\right) \quad (2.29)$$

where a is the epilayer lattice constant. The model of Matthews and Blakeslee provides a conservative estimate, i.e. a layer grown at the critical thickness predicted by this model will never relax. It is suggested here that the epilayer thickness at which a significant portion of the strain is relieved through misfit dislocations generally lies somewhere between values obtained from the two models. Equation 2.27 and Equation 2.29 are generally solved by tabulating the value of the right hand side of the equation against h_c , using a spreadsheet.

References

- [1] A. Rogalski and Z. Orman, *Infrared Phys* 25, 3 (1985).
- [2] S. M. Sze, *Physics of Semiconductor Devices*, 2ED (1981).
- [3] P. Chakrabarti, A. Krier, and A. F. Morgan, *IEEE Trans. Electron. Devices*, Vol 50, No 10 (2003).
- [4] NSM Archive - Physical Properties of Semiconductors, Ioffe Institute,
<http://www.ioffe.ru/SVA/NSM/Semicond/index.html>
- [5] H. S. Kim, E. Plis, A. Khoshakhlagh, S. Myers, N. Gautam, Y. D. Sharma, L. R. Dawson, S. Krishna, S. J. Lee, and S. K. Noh, *Appl. Phys. Lett.* 96, 033502 (2010).
- [6] B. Van Zeghbroeck, *Principles of Semiconductor Devices*, Chapter 4: “p-n junctions” (2011).
- [7] Agilent Impedance Measurement Handbook, 4ED. <http://cp.literature.agilent.com/litweb/pdf/5950-3000.pdf>
- [8] G. E. Stillman and C. M. Wolfe, “Avalanche Photodiodes,” in *Infrared Detectors II*, R. K. Willardson and A. C. Beer, Eds., vol. 12 of *Semiconductors and Semimetals*, pp. 291-393. Academic Press, New York 1977.
- [9] A. R. J. Marshall, C. H. Tan, M. J. Steer, and J. P. R. David, *Appl. Phys. Lett.* 93, 111107 (2008).
- [10] R. K. Willardson, *Semiconductors and Semimetals; Infrared Detectors*, Academic Press Inc. (1970).
- [11] I. M. Baker, Selex UK (personal communication).
- [12] R. J. McIntyre *IEEE Trans. Electron Devices* 13, 1, 164 (1966).
- [13] D. S. Ong, K. F. Li, G. J. Rees, J. P. R. David, and P. N. Robson, *J. Appl. Phys.* 83, 6, 3426 (1998).
- [14] M. A. Saleh, M. M. Hayat, B. E. A. Saleh, and M. C. Teich, *IEEE Trans Electron*

Devices, 47, 3 (2000).

[15] S. L. Chan, Choo K. Y, in IEEE 2nd International Conference on Photonics, p1-5 (2011).

[16] M. P. C. M. Krijn, *Semicond. Sci. Technol.* 6, 27 (1991).

[17] C. G. Van de Walle, *Phys. Rev. B*, 39, 3 (1989).

[18] I. Vurgaftman and J. R. Meyer, *J. Appl. Phys.*, 89, 11 (2001).

[19] Matthew D. McCluskey, Eugene E. Haller, "Dopants and Defects in Semiconductors", CRC Press (2012).

[20] S. Maimon and G. W. Wicks, *Appl. Phys. Lett.* 89, 151109 (2006).

[21] A. Krier (ed.), *Mid-infrared Semiconductor Optoelectronics*, Springer Series in Optical Sciences, 118 (2006) p547-592 "High-speed Avalanche Photodiodes for the 2–5 μm Spectral Range", M. P. Mikhailova and I. A. Andreev.

[22] J. W. Matthews and A. E. Blakeslee, *J. Cryst. Growth*, 27, 118 (1974).

[23] R. People and J. C. Bean, *Appl. Phys. Lett.* 47, 322, (1985).

[24] S. M. Hu, *J. Appl. Phys.*, 69, 11 (1991).

(3) Literature review

This section first provides a summary of key literature relating to the lattice mismatched growth of both GaSb on GaAs and GaSb on Si. Previous reports of derivative devices (grown on GaAs substrates) are then examined. nBn detectors are treated next, via an exploration of papers by Maimon and Wicks at Rochester, NY, U.S.A, and Klipstein et. al. at SemiConductor Devices (SCD) in Israel. Further attention is given to nBn detectors based on strained-layer-superlattice (SLS) absorption regions, including to two-colour and complementary barrier designs. Finally, avalanche photodiodes (APDs) are explored, including those based on binary InAs material, as well as more complicated separate absorption and multiplication (SAM) structures. These discussions are intended to provide a synopsis of previous works which made possible the research presented in sections 5-7, as well as providing a general overview of the literature.

i) Lattice mismatched growth and interfacial misfit arrays

Molecular beam epitaxial (MBE) growth of GaSb layers on GaAs substrates was reported in 1992 by Ivanov et. al.¹ GaAs buffer layers of 200 nm thickness were deposited at 620 °C before the growth of a GaSb buffer layer with a thickness of ~0.5 µm. Superlattice (SL) layers (acting as threading dislocation filters) consisting of 10 repeats of 5 nm Al_{0.3}Ga_{0.7}Sb/5 nm GaSb or 5 nm AlSb/5nm GaSb were then grown at temperatures between 500 °C and 540 °C. This was followed in each case by a 1 µm-thick GaSb epilayer, grown at a rate of 0.6 MLs⁻¹. Mirror-like epi-surfaces were reported for each sample after growth was complete. For the sample with an AlSb/GaSb SL, the threading dislocation density (TDD) was found using transmission electron microscopy (TEM). It was stated to be around 10¹⁰ cm⁻² at the GaSb/ GaAs interface, but this figure was reduced to 2 – 3 × 10⁸ cm⁻² within 200 – 400 nm GaSb film thickness. It was further reported that the use of a two-temperature growth improved the crystal quality: the

first 0.5 μm of the GaSb overlayer was grown at 530 $^{\circ}\text{C}$, but the remaining film thickness was grown at 500 $^{\circ}\text{C}$. This was evidenced via a reduction in full width at half maximum in x-ray diffraction (XRD) Bragg scans (154 arcsec for the two-temperature growth, compared with 160 – 215 arcsec for a single growth temperature of 530 $^{\circ}\text{C}$). It was observed that the majority of the population of misfit dislocations at the lattice-mismatched interface were of the pure-edge type, as arranged in a periodic network with a spacing of $\sim 55 \text{ \AA}$, illustrated in Figure 3.1. In addition, photoluminescence (PL) measurements for the mismatched samples were compared with similar measurements for the case of a similar film grown on native GaSb. However, it was found that the PL intensity recorded was lower by three orders of magnitude for the growth on GaAs.

In 1997, Qian et. al. reported a reduction in the defect density for GaSb films grown on GaAs through the use of SL layers.² These consisted of AlSb/GaSb and $\text{In}_{0.11}\text{Ga}_{0.89}\text{Sb}/\text{GaAs}$, respectively. GaSb layers were grown at 550 $^{\circ}\text{C}$ and 0.8 MLs^{-1} . An investigation of the relationship between the film thickness and the TDD was then carried out, both with no dislocation

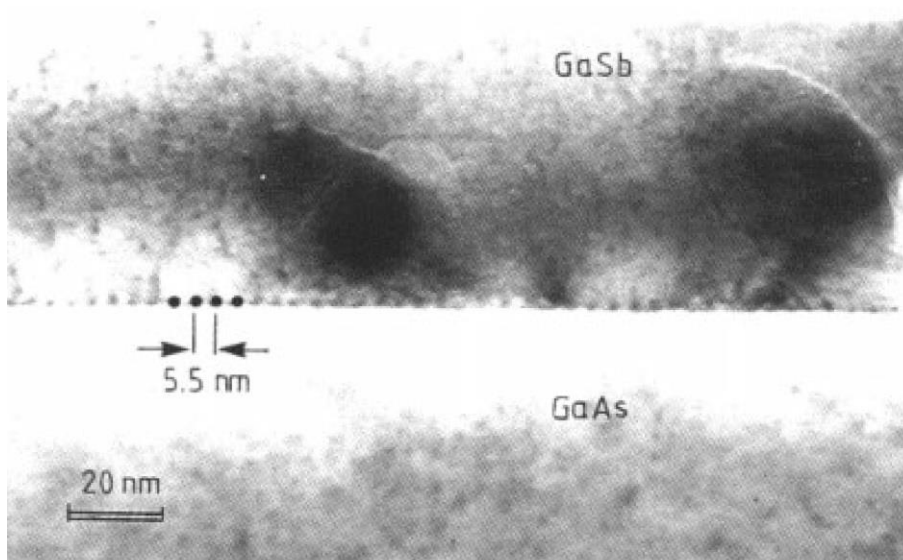


Figure 3.1: Cross-sectional TEM image showing the interface between GaAs and GaSb layers, from [1]. The dark spots were stated to be due to edge dislocations.

filter and with AlSb/GaSb and InGaSb/GaAs SL layers, respectively. Once again, TEM images showed arrays of misfit dislocations of the 90° type at the mismatched interface with a periodicity of $\sim 55 \text{ \AA}$. However, it was also reported that, by inspection of a larger volume of epilayer, there were still many threading dislocations. These were attributed to a minority population of 60° misfits. Through measurements carried out for GaSb film thicknesses between $0.5 - 14 \text{ \mu m}$, an empirical relationship between the TDD, ρ , and the film thickness, t , was obtained

$$\rho = \frac{10^9}{t^{5/3}} \quad (3.1)$$

where ρ has units of cm^{-2} and t has units of cm . The fitting used to determine the above relationship is shown in Figure 3.2. Finally, a fully optimised growth using a 5-period GaSb/AlSb SL was demonstrated, with a TDD of $5 \times 10^7 \text{ cm}^{-3}$ for a total film thickness of 2.2 \mu m .

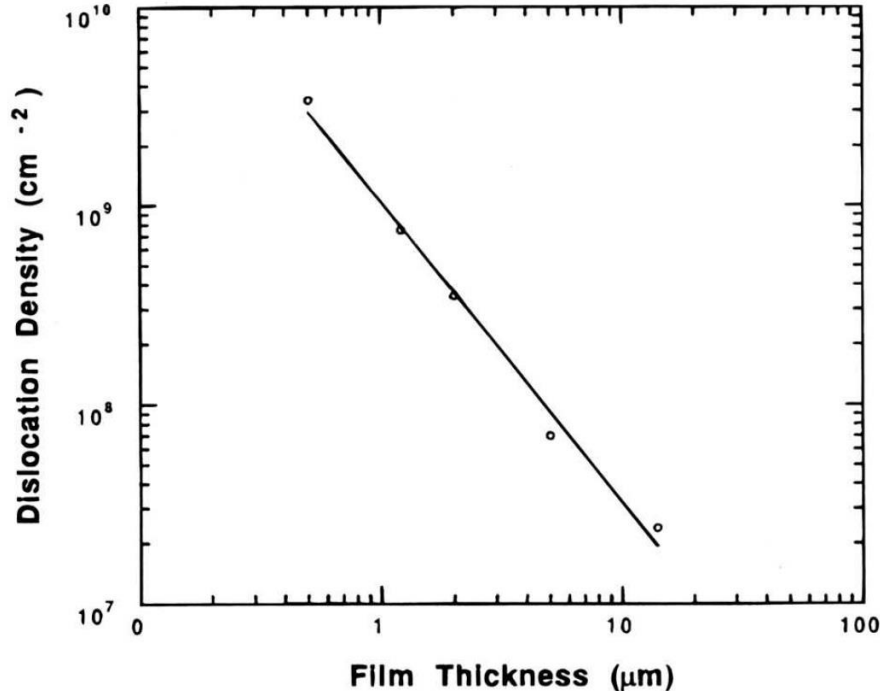


Figure 3.2: Threading dislocation density, as a function of film thickness, for GaSb films grown on GaAs by MBE, from [2].

In 2006, Huang and co-workers reported a realisation of low defect density GaSb layers grown on GaAs substrates.³ Strain relief was stated to occur exclusively via 90° (laterally propagating) dislocations, i.e. without the presence of 60° misfit dislocations. The occurrence of 60° misfit dislocations was thought to be associated with the coalescence of islands of GaSb in the early stages of growth, and the choice of growth temperature, with growth at 510°C resulting in an elimination of 60° misfits. The authors describe the growth of a GaAs buffer layer at 560°C . A special desorption step was then described, where As adatoms were removed from the growth surface by closing the As valve, leaving the growth surface Ga terminated. Sb_2 flux was then applied followed by a reduction in temperature to 510°C . GaSb growth then proceeded with a reflection high energy electron diffraction (RHEED) pattern of 1×3 reconstruction exhibited. The misfit array is illustrated using cross-sectional transmission electron microscopy (TEM) in Figure 3.3. The dark spots were stated to correspond to misfit sites and an absence of visible threading dislocations cited. The misfit separation was measured (from Figure 3.3) to be 5.6 nm, corresponding to 13 lattice sites of GaSb and 14 lattice sites of GaAs. One in every 14 Ga atoms thus forms a dangling bond. For samples grown under optimised growth conditions, KOH etch pit defect density (EPDD) defect density figures $7 \times 10^5 \text{ cm}^{-2}$ were reported (for an epilayer thickness of $3.1 \mu\text{m}$). It was further stated that growths carried out at 480°C and 540°C had larger EPDD figures, but these were not quoted. No control sample (no comparison drawn with non-IMF growth) was reported.

In 2009, the same authors reported plan-view TEM studies of GaSb epilayers grown on GaAs substrates via the IMF array growth mode.⁴ The work introduces the term *interfacial misfit (IMF) array* and refers to this as a new growth mode. However, the network of 90° misfit dislocations reported is also itself referred to as “an IMF”. A 2×8 RHEED pattern was noted to be observed following the application of Sb_2 flux, believed to be associated with the formation of the IMF array. A defect density figure of $5.4 \times 10^5 \text{ cm}^{-2}$ was reported. This

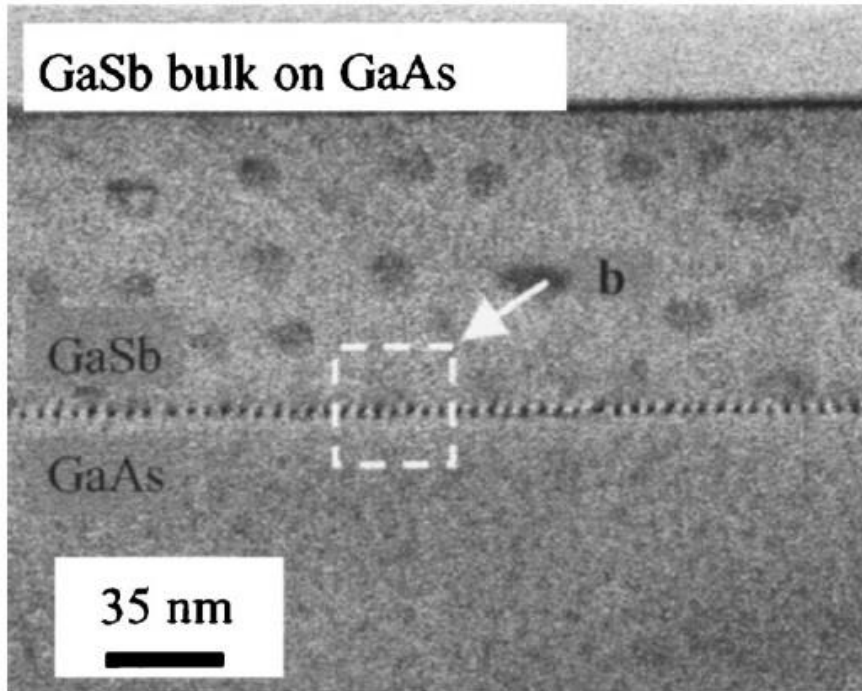


Figure 3.3: Cross-sectional TEM image showing a highly periodic array of 90° misfit dislocations (an IMF array) at the interface between a GaSb epilayer and a GaAs buffer layer.³

figure was explained to be based on counting visible dislocations in plan-view TEM images of a sample with a $5\ \mu\text{m}$ -thick GaSb epilayer. An example of such an image is reproduced in Figure 3.4.

In 2011, workers at the University of Maryland reported details of the structural properties of lattice mismatched films grown on GaAs substrates using IMF arrays.⁵ These films consisted of binary GaSb, InAs and InP, as well as ternary and quaternary alloys. It was reported that the films achieved full relaxation within a few monolayers of the interface. X-ray diffraction (XRD) reciprocal space mapping was used to determine the degree of relaxation. For the GaSb film in particular, the article points out overgrowth was carried out without first soa-king the Ga-rich surface under Sb_2 flux, in contrast to the procedure used by Huang et. al.

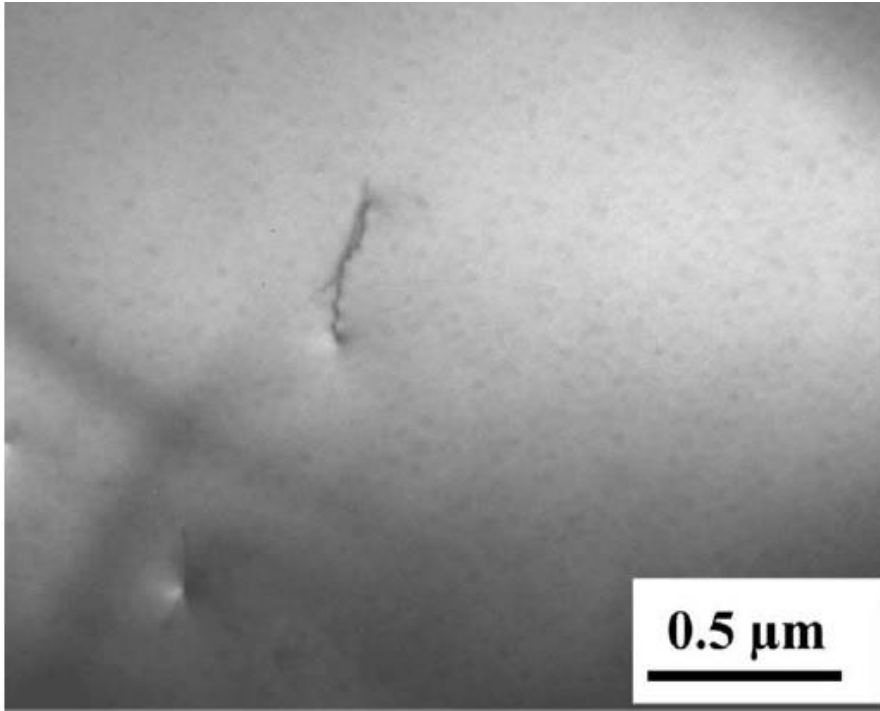


Figure 3.4: Plan-view TEM image of an IMF array sample with a thick buffer layer (5 μm of GaSb on GaAs) with a single threading dislocation exhibited.⁴

Figure 3.5(a) and 3.5(b) show $2\times$ and $4\times$ RHEED reconstructions, respectively associated with the As-terminated and Ga-terminated GaAs growth surfaces, before and after the cessation of As_2 flux (before GaSb growth). Figure 3.6(a) and 3.6(b) then show RHEED patterns exhibited as GaSb growth proceeded. The transition from initial 3D (Volmer–Weber) growth – indicated by a spotty RHEED pattern – to 2D (layer-by-layer or Frank–van der Merwe) growth – as indicated by a streaked reconstruction – is evident. XRD full width at half maxima (FWHM) of 49 arcsec, 34 arcsec and 22 arcsec were reported for film thicknesses of 1 μm , 2 μm and 5 μm films, respectively. For InAs films – for which there was no change in group-V species during growth – an FWHM of 28 arcsec was noted for 5 μm film thickness.

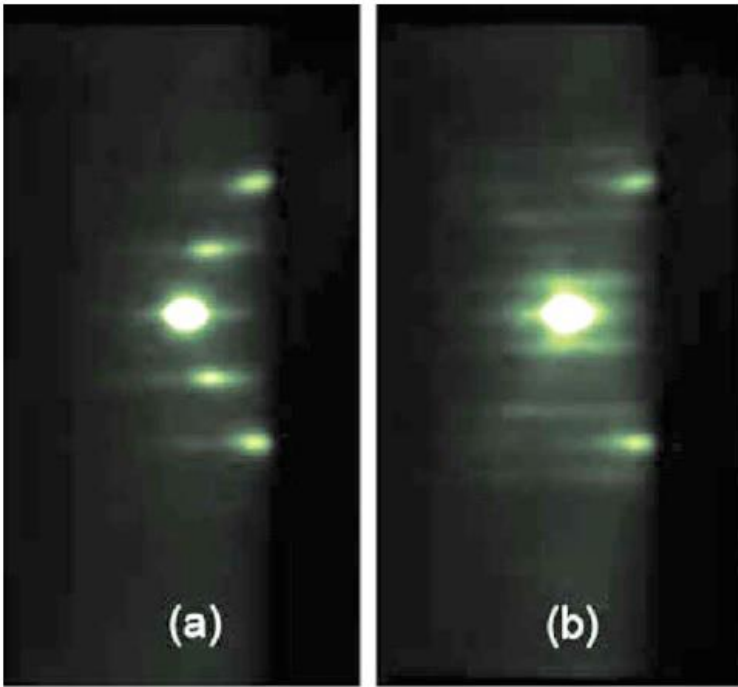


Figure 3.5: Shows the effect of the cessation of As_2 flux upon a GaAs surface, with the $2 \times$ RHEED reconstruction in (a) corresponding to an As-terminated surface and the $4 \times$ reconstruction in (b) corresponding to a Ga-terminated surface.⁵

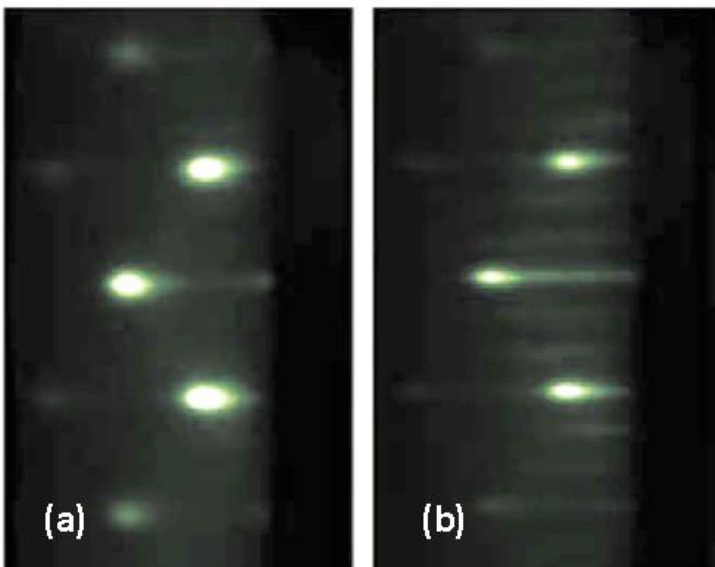


Figure 3.6: RHEED patterns exhibited after (a) 3 ML and (b) 10 ML of GaSb growth following the formation of an IMF array and the introduction of Ga flux.⁵

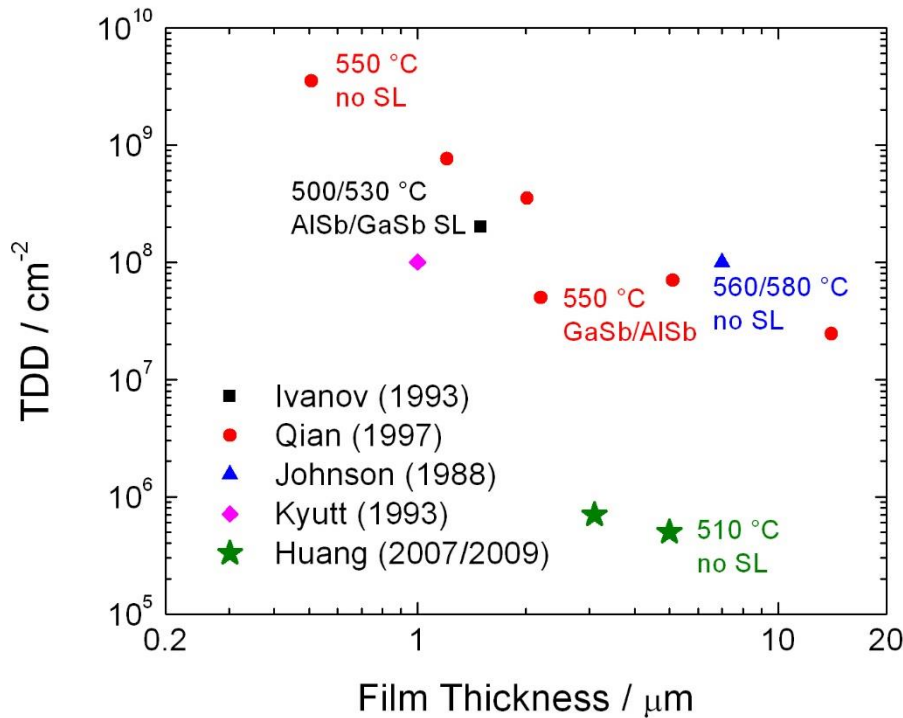


Figure 3.7: Threading dislocation density, as a function of GaSb film thickness, as found by various authors. Data for Johnson was taken from [6] and Kyutt was taken from [7]. The growth temperature and SL dislocation filter used in each case is labelled in coloured text.

Figure 3.7 provides a summary of TDDs for the growth of GaSb on GaAs, as reported by various authors. It can be seen that figures reported by Huang et. al. are several orders lower than those by other authors, even without the use of an SL dislocation filter.

Various authors (including refs [8],[9]) have reported the growth of GaSb on Si substrates using thin AISb buffer layers. In 2004, Akahane et. al. reported the optimisation of the growth temperature and thickness for the AISb buffer layers, successfully obtaining photoluminescence (PL) emission from GaSb/AlGaSb quantum wells (QWs) at 1425 nm (at 12 K).⁸ Without the AISb buffer layer, a clouded surface and an XRD FWHM of over 700 arcsec were exhibited. With the introduction of such a layer, the FWHM was reduced to 582 arcsec and the sample surface had a mirror finish. (It should be noted that the FWHM given here are not comparable to those of Richardson et. al. due to the dependence on the optics of the XRD

system). A GaSb growth temperature of around 500 °C was found to be optimal, through balancing Sb desorption at higher temperatures with crystalline quality, found to be optimised at around ~530 °C. The optimum AlSb layer thickness was found to be around 5 nm. TEM studies of GaSb layers grown on Si were reported by Kim et. al. in 2006.⁹ The authors grew GaSb onto Si, both directly and via an AlSb buffer layer, once again. An AlSb buffer layer thickness of 8 ML was used. Twin boundaries were reported for the sample without a buffer layer, as shown in Figure 3.8. These were attributed to the growth of polar compounds (III-V) on a non-polar layer (Si). The mechanism of action of the AlSb buffer layer in improving crystalline quality was explained in terms of the formation of islands of AlSb, which act as sites where 2D growth is energetically favoured.

Since the IMF array was first reported in 2006, relatively few papers have been published demonstrating derivative devices. In the same year, vertically emitting QW light emitting diodes (LEDs) based on GaSb/AlGaSb quantum well barriers/active regions grown on GaAs were reported by Metha et. al.¹⁰ The use of GaAs/AlGaAs distributed Bragg reflectors (DBR) provided a resonant cavity with superior index contrast (yielding a reflectivity of 80% for the

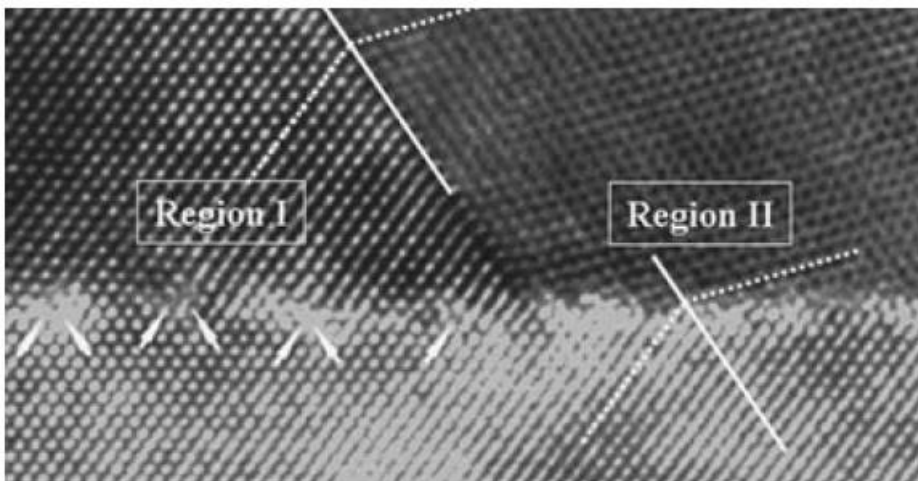


Figure 3.8: High-resolution TEM image showing twin boundaries in GaSb layers grown directly onto Si, as reported by Kim et. al.⁹ The arrows indicate misfit dislocations.

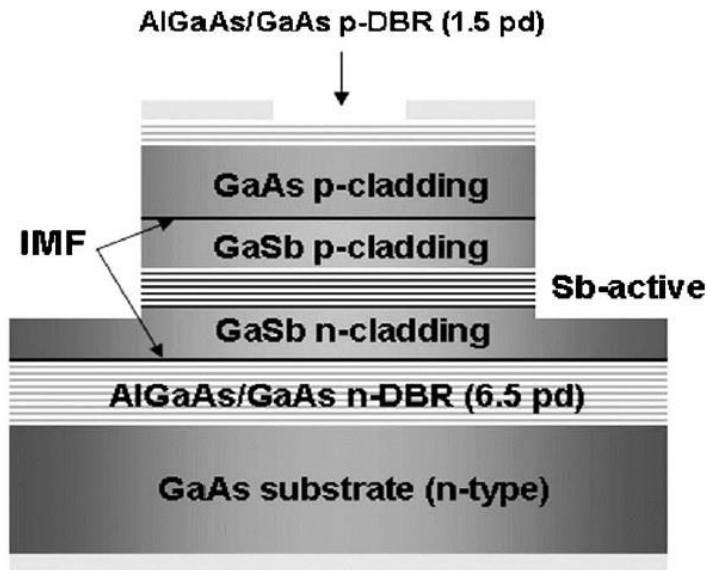


Figure 3.9: Vertically emitting Sb-based LED structure with AlGaAs/GaAs DBRs, grown on a GaAs substrate.¹⁰

lower DBR and 40% for the upper DBR) when compared to Sb-based DBRs. The requirement for an *n*-type GaSb contact – known to be problematic – was also circumvented through the use of a GaAs substrate. An AlGaSb/GaSb multiple quantum well (MQW) active region was inserted between the Bragg mirrors using two IMF array interfaces; the structure is illustrated in Figure 3.9. Emission was reported at 1.6 μm , though the authors note that the incorporation of an In mole fraction in the active region could extend the operating wavelength to 2 – 3 μm . Type-II structures were also suggested, which would allow operation beyond 3 μm .

In 2009, Rogriguez et. al. reported a continuous wave (CW) laser operating at 2.2 μm , grown on GaAs using the same steps as detailed by Huang (see above).¹¹ The active region consisted of two $\text{Ga}_{0.68}\text{In}_{0.32}\text{As}_{0.06}\text{Sb}_{0.94}$ QWs separated by $\text{Al}_{0.35}\text{Ga}_{0.65}\text{As}_{0.03}\text{Sb}_{0.97}$ barrier layers. The cladding regions consisted of $\text{Al}_{0.90}\text{Ga}_{0.10}\text{As}_{0.06}\text{Sb}_{0.94}$ lattice matched to GaSb (lattice constant 6.09 \AA). The structure is illustrated in Figure 3.10. CW operation was reported at temperatures up to 50 $^{\circ}\text{C}$. Threshold current densities of 1.5 – 2.2 kAcm^{-2} were reported; these

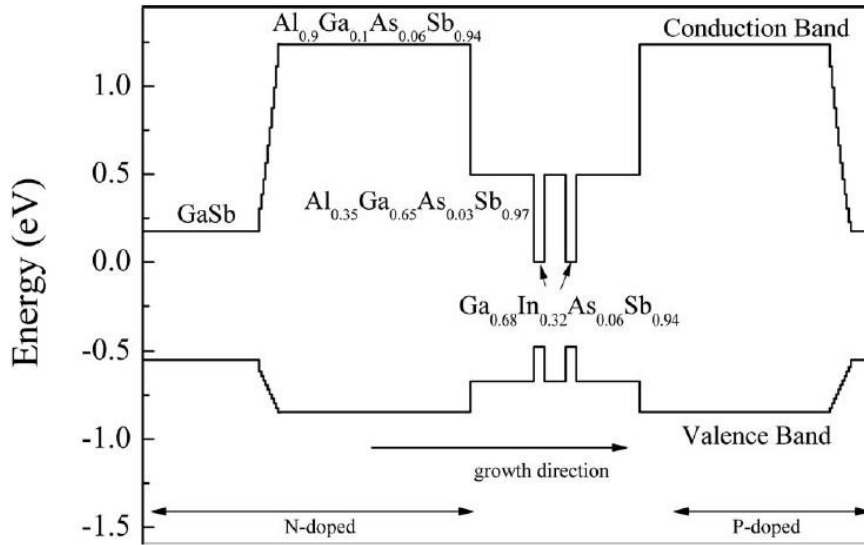


Figure 3.10: Band diagram for a $\text{Ga}_{0.68}\text{In}_{0.32}\text{As}_{0.06}\text{Sb}_{0.94}$ QW type-I laser grown on a GaAs substrate (using an IMF array).¹¹

figures were noted to be within a factor of 10 of those reported elsewhere for equivalent devices grown on native GaSb substrates.

In 2012, Nunna and coworkers reported short wave infrared (SWIR) *p-i-n* photodiodes based on GaInAsSb material grown on GaAs.¹² After the implementation of the IMF array, the structure was grown lattice matched to a GaSb buffer layer. Spectral response measurements revealed cut-off wavelengths around $2.2 \mu\text{m}$, as illustrated in Figure 3.11. An R_0A (which is just the peak value of R_dA close to zero bias) of $260 \Omega\text{cm}^{-2}$ was reported. This value was noted to be superior to values quoted in the literature for similar devices grown on native GaSb substrates ($1 - 80 \Omega\text{cm}^{-2}$). However, the authors did not produce a control sample. A peak responsivity of 0.8 AW^{-1} and peak D^* figures of $3.8 \times 10^{10} \text{ cm Hz}^{1/2} \text{ W}^{-1}$ for -0.2 V bias were also reported at room temperature. SU-8 dielectric was found to significantly ameliorate surface leakage currents, with a reduction in the dark current density by around a

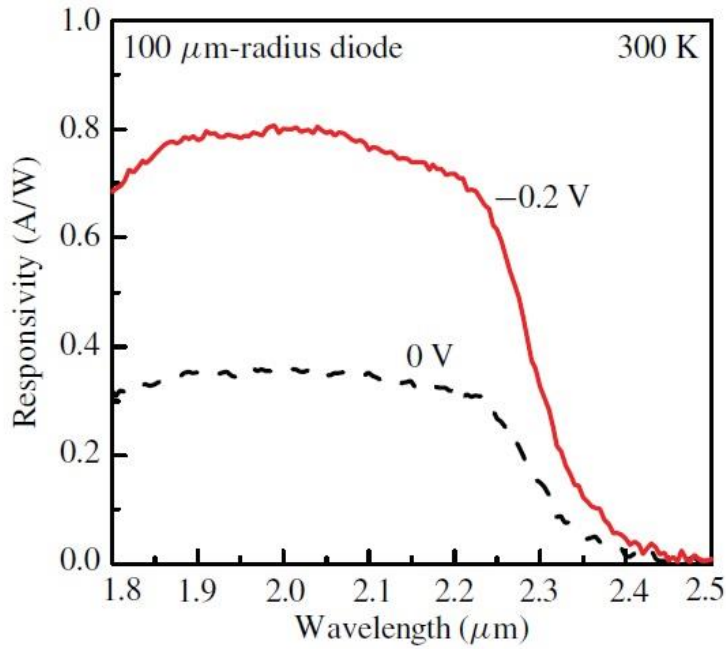


Figure 3.11: Spectral responsivity for a GaInAsSb p - i - n photodiode grown on GaAs (using an IMF array).¹²

factor of 2 for samples etched using an H_3PO_4 -based solution, and around a factor of 10 for samples processed using BCl_3/Ar dry-etch chemistry. 300 K PL measurements showed a peak emission wavelength of $2.25 \mu\text{m}$; from this result, and the lattice matching condition, the composition of the quaternary was determined to be $\text{Ga}_{0.82}\text{In}_{0.18}\text{As}_{0.16}\text{Sb}_{0.84}$.

ii) nBn detectors for long wavelength detectors with low dark currents and noise

In 2006, Maimon and Wicks reported a new type of photodetector claimed to eliminate Shockley Read Hall generation currents termed the nBn detector.¹³ As a result of this suppression of SRH generation, the dark currents and noise of the nBn detector were said to be lower than those of p - n photodiodes, permitting operation at higher temperatures (for the same level of performance). Cut off wavelengths of $3.4 \mu\text{m}$ and $4.2 \mu\text{m}$ were reported at 220 K, for samples with InAs and InAsSb absorption regions, respectively. The key components of the nBn design were given in Section (2) of this work. It was further noted in the reference that the barrier layer should be thick enough to prevent tunnelling – for the AlAsSb barriers used by Maim-

on, thicknesses of 50-100 nm were considered adequate. The barrier was specified to be undoped. A barrier layer composition of $\text{AlAs}_{0.15}\text{Sb}_{0.85}$ was found to yield the highest quantum efficiency (QE), suggesting this composition minimises the valence band offsets with respect to the InAs(Sb) absorption/contact layers. Maimon distinguishes the nBn from previous barrier detector structures through its inhibition of majority carrier dark currents, whereas other works have done the reverse, i.e. pass majority carriers and inhibit the flow of minority carriers. The primary source of dark currents in the nBn detector was identified as thermally generated minority carriers in the absorption layer which diffuse to the contact layer, i.e. diffusion current. The nBn design was further reported to eliminate surface leakage currents, as can be explained with reference to the inset of Figure 3.12. It can be seen in the figure that the mesas are defined without etching through the barrier layer, i.e. are formed from the contact layer only. This is done using a using a selective etchant ($\text{C}_6\text{H}_8\text{O}_7:\text{H}_2\text{O}_2$). The barrier layer then acts as a passivation layer, so that no additional passivation steps (e.g. the application of SU-8 dielectric) are required. Maimon further states that the absorption layer was

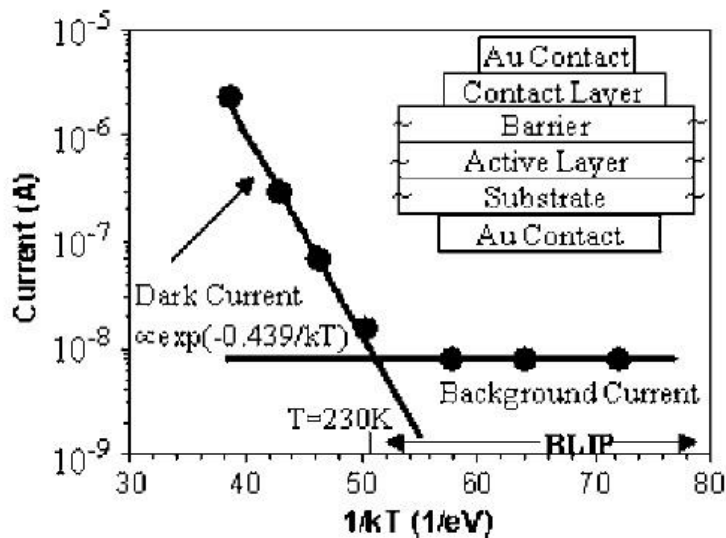


Figure 3.12: Arrhenius plot of the dark current density for an InAs nBn detector, exposed to background radiation from a 300 K scene through an angle of 2π steradians.¹³

grown with unintentional doping only ($\sim 2 \times 10^{16} \text{ cm}^{-3}$). Figure 3.12 shows an Arrhenius plot illustrating the temperature dependence of the nBn detector dark currents. It can be seen that the activation energy at high temperatures is close to the 4 K bandgap of InAs (0.417 eV), indicating diffusion limited dark currents. At lower temperatures, currents due to the 300 K scene (background radiation) dominate. The intersection point between the diffusion limited region and the background limited region indicates the background limited infrared photodetection (BLIP) temperature, which is around 230 K. Comparison was then drawn with BLIP temperatures in commercial photodiodes, which were noted to be inferior by around 100 K. The identification of the BLIP regime between $1/kT = 55 - 75 \text{ eV}^{-1}$ can be verified by calculating the 300 K blackbody spectrum between 2 – 3.5 μm for sufficiently short intervals dividing by the photon energy and then integrating, yielding $\sim 1.1 \times 10^{-8} \text{ A}$ for a 100 μm x 100 μm device (as was used for the measurement shown in Figure 3.12). The background photocurrent measured is smaller by a factor of ~ 1.4 , likely accounted for by the non-unity quantum efficiency.

Separately, Klipstein et. al. first reported XBn detectors in 2008.¹⁴ The difference in the abbreviation (XBn rather than nBn) stems from the possibility to use a wider bandgap material (such as p -type GaSb) for the contact layer, acting as an optical window (longer wavelength photons are not absorbed by the wide-bandgap material). The reference also states that the doping level in the barrier layer should be optimised to prevent depletion of the absorption layer. This can be explained with reference to Figure 3.13, which shows the band alignment for a $C_pB_n n$ design detector under operating bias. The operating bias maintains the Fermi level in the p -GaSb contact layer above that in the n -type absorption layer, allowing the free flow of holes from the barrier to the contact. At the same time, electrons residing in donor levels inside the barrier layer can all reduce their energy by moving to the electron

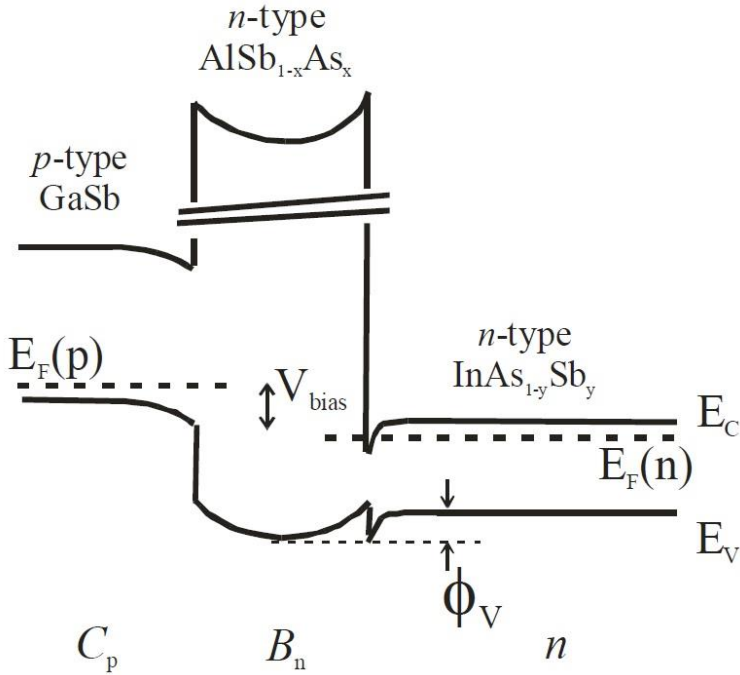


Figure 3.13: Band diagram for a $C_pB_n n$ design XB_n detector, showing the position of the Fermi level and the electron accumulation layer (adjacent to the barrier).[14]

accumulation layer at the interface between the barrier and the absorption layer. The barrier layer is therefore fully depleted. As increasing reverse bias is applied, electrons are transferred from this accumulation layer to the contact layer, avoiding depletion in the absorption layer. It is then explained that there then exist a range of operational bias conditions for which holes can be excited over the barrier potential “ ϕ_v ” – which is the energy difference between the flat valence band position in the absorption layer and the minimum position of the barrier valence band – but for which the depletion does not occur in the absorption layer. For larger reverse bias, the absorption layer would begin to deplete, and SRH generation currents would result. It is further noted that p -type barrier doping can also be used provided that an n -type delta doped sheet is inserted between the absorption and barrier layers. The reference later describes a theoretical investigation of the barrier tunnelling and thermionic emission currents. It was found that, for nBn structures with conduction band offsets in excess of 0.8 eV, thermionic

emission currents should be less than $10^{-20} \text{ Acm}^{-2}$ – i.e. should be negligible. Tunnelling current densities lower than $10^{-12} \text{ Acm}^{-2}$ were predicted for barrier thickness greater than 40 nm (presumably for small operating bias).

In 2010, Klipstein et. al. reported experimental results for $\text{InAs}_{0.91}\text{Sb}_{0.09}$ *nBn* structures with various doping levels in the absorption and barrier layers.¹⁵ Arrhenius plots of the dark current density yielded activation energies of 350 meV and 390 meV for samples with *n*-type doping in the barrier layers and absorption layer doping densities of $4 \times 10^{15} \text{ cm}^{-3}$ and $4 \times 10^{16} \text{ cm}^{-3}$, respectively. Two samples with *p*-type barrier layer doping ($\sim 10^{15} \text{ cm}^{-3}$) had absorption layer doping densities of $1.5 \times 10^{17} \text{ cm}^{-3}$ and these were found to have activation energies of 411 meV and 390 meV respectively. Area scaling of the dark currents was demonstrated (in particular) for one of the samples with a *p*-type barrier layer, as shown in Figure 3.14, indicating the suppression of surface currents was effective. A single gradient fitting is indicated in the figure, indicating dark currents remained diffusion limited at temperatures down to ~ 150 K. It was explained that measurements at lower temperatures could not be readily achieved (presumably due to the limitations of the source measurement unit). Photore-sponse measurements were carried out at 150 K for two samples with different absorption layer doping densities. 50% cut-off wavelengths of 3.96 μm and 3.65 μm were measured, for doping levels of $4 \times 10^{15} \text{ cm}^{-3}$ and $1.5 \times 10^{17} \text{ cm}^{-3}$, respectively. The blue shift with doping density was attributed to Moss-Burstein shift. Peak responsivities (measured at around 3 μm) of 1.1 AW^{-1} and 0.7 AW^{-1} , respectively, were also determined.

Klipstein et. al. further demonstrated focal plane arrays (FPAs) based on *XBn* detectors in 2013.¹⁶ Based on InAsSb absorption material grown lattice matched to GaSb, these were noted to be among the first to have been made commercially available, branded as “Kinglet”. Their operational temperature was stated to be 150 K.

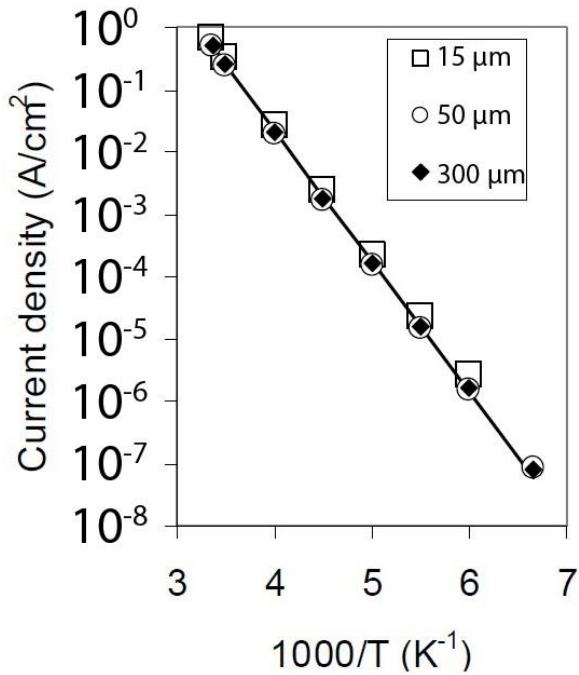


Figure 3.14: Arrhenius plot showing the dark current density, for various mesa areas, for an *nBn* sample with a *p*-type barrier layer.¹⁵

Various authors have demonstrated *nBn* structures using type-II strained-layer-superlattice (SLS) absorption layers, including refs [17-21]. Refs [17-20] are based on absorption regions with a configuration of 8 ML InAs / 8 ML GaSb, yielding cut-off wavelengths of around 4.2 μm at 77K and around 5.2 μm at 300 K. These used barriers consisting of $\text{Al}_{0.2}\text{Ga}_{0.8}\text{Sb}$ or $\text{Al}_{0.4}\text{Ga}_{0.6}\text{Sb}$. It is noted that the SLS electron effective mass is larger (around $0.04m_0$)¹⁵ than that of HgCdTe materials, and does not depend on the cut-off wavelength of the superlattice, resulting in lower tunnelling currents. Mesa diodes were defined using either wet chemical etchants based on H_3PO_4 – refs [17,19] – or using BCl_3/Ar dry-etch chemistry – refs [18, 20]. Refs [17,19] also use dry-etching for the barrier layer. Ref [17] investigates the effect of using a deep mesa etch, i.e. etching the mesas to a depth below the barrier, as illustrated in Figure 3.15(b). It was found that 77 K dark currents two orders of magnitude greater were

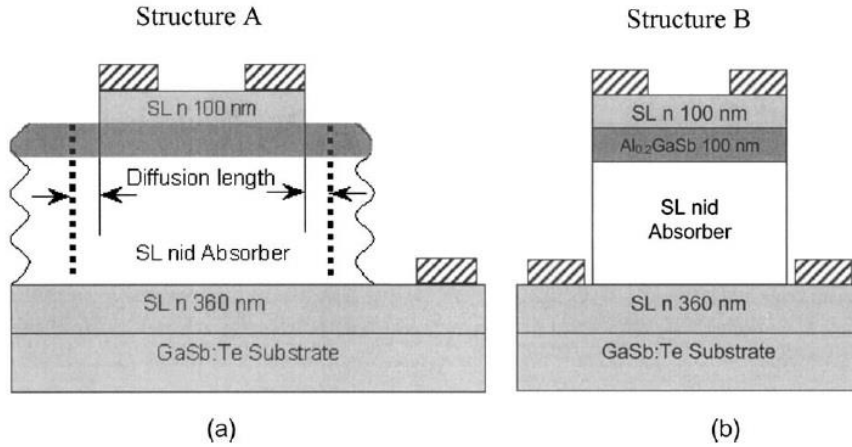


Figure 3.15: Illustration of (a) conventional nBn processing and (b) a deep etched nBn sample. Deep etching was found to result in inferior dark current performance.¹⁷

measured than for the conventionally processed nBn , i.e. where the barrier layer is not etched, acting as a passivation layer, as in Figure 3.15(a). This highlights the suppression of surface currents by the nBn design. Typical peak D^* figures of around $6 \times 10^{11} \text{ cm Hz}^{1/2} \text{ W}^{-1}$ and $10^9 \text{ cm Hz}^{1/2} \text{ W}^{-1}$ were reported, at 77 K and 300 K, respectively.^{14,15} Ref [19] reports the fabrication of an FPA based on a type-II SLS-based nBn structure, yielding a peak responsivity of 1.6 AW^{-1} at $3.8 \mu\text{m}$. Ref [20] gives details of an nBn structure once again based on 8 ML InAs / 8 ML GaSb, but grown on GaAs using an IMF array. Dark current densities of around $6 \times 10^{-4} \text{ Acm}^{-2}$ at -0.1 V and peak D^* figures of $1.2 \times 10^{11} \text{ cm Hz}^{1/2} \text{ W}^{-1}$ were reported at 77 K. These figures were noted to be comparable to equivalent figures for nBn and $p-i-n$ detectors grown on GaSb by the same group. Ref [21] gives details of a LWIR nBn structure, with an absorption layer configuration of 13 ML InAs / 7 ML GaSb, yielding a cut-off wavelength of around $8 \mu\text{m}$ at 300 K. This was then compared with an equivalent $p-i-n$ structure, using measurements at 77 K, and found to have lower a lower dark current density (0.05 Acm^{-2} vs 0.08 Acm^{-2} at -0.1 V), a higher peak D^* ($7.2 \times 10^9 \text{ cmHz}^{1/2} \text{ W}^{-1}$ vs $6.1 \times 10^9 \text{ cmHz}^{1/2} \text{ W}^{-1}$) and a higher responsivity (1.28 AW^{-1} vs 1.03 AW^{-1}).

Through the use of two SLS absorption regions positioned either side of the barrier layer, Khoshakhlagh et. al. demonstrated a “two-colour” *nBn* detector.²² Selection of the absorption wavelength is made through the bias polarity, as illustrated in Figure 3.16. The authors explain that the structure was developed to use a thick, mid-wave infrared (MWIR) SLS absorption layer – consisting of 8 ML InAs / 8 ML GaSb – in place of the top contact layer, and a long-wave infrared (LWIR) SLS absorber on the other side of the barrier, consisting of 9 ML InAs / 5 ML In_{0.25}Ga_{0.75}Sb. The full structure is depicted in the inset of Figure 3.17. Figure 3.17 further shows measured spectral response for both bias polarities. In the main figure, which shows the spectral response, two separate cut-off wavelengths of 4.5 μm and 8 μm are clearly apparent, although the responsivity and D^* were not quantified.

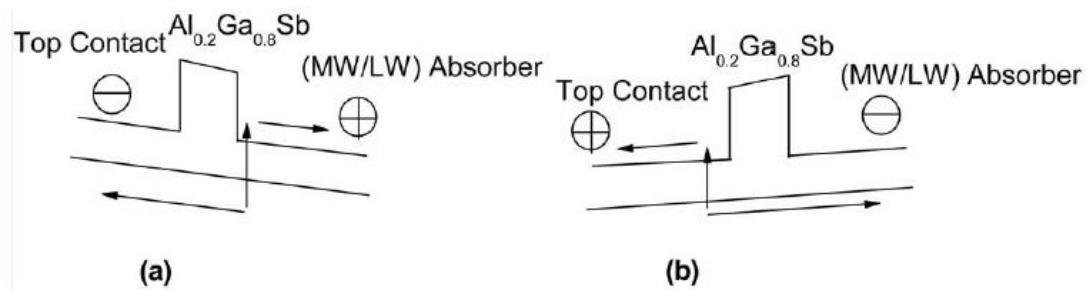


Figure 3.16: Band diagrams showing an *nBn* detector operating (a) in reverse bias, where photogenerated carriers in the absorber (mid- or long-wave, MW/LW) are collected, and (b) in forward bias, where the detector is sensitive to absorption in the top contact.²²

In 2009, Ting and coworkers demonstrated a variation of the *nBn* design named the “complementary barrier” infrared detector (CBIRD).²³ Through the use of two barrier layers, which block the dark currents due to both electrons and holes, respectively, 77 K dark current densities as low as $1 \times 10^{-5} \text{ Acm}^{-2}$ were demonstrated, for 9.9 μm cut-off wavelength and -0.2 V bias. Peak D^* figures of $1 \times 10^{11} \text{ cm Hz}^{1/2} \text{ W}^{-1}$ were further reported, for a temperature of 87 K. The barrier layers were formed using SLS layers of 8 ML InAs / 2 ML AlSb

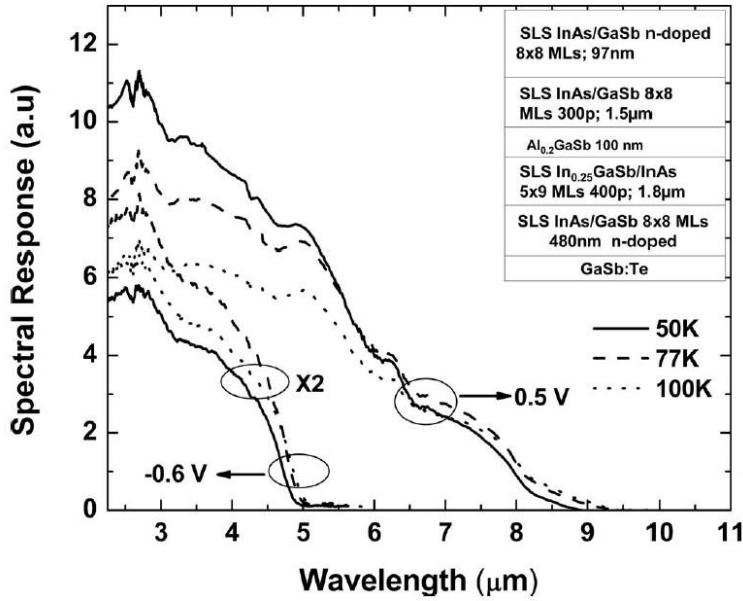


Figure 3.17: Spectral response for a two-colour *nBn* detector (for both bias polarities) with MWIR and LWIR absorbers positioned either side of the barrier layer.²²

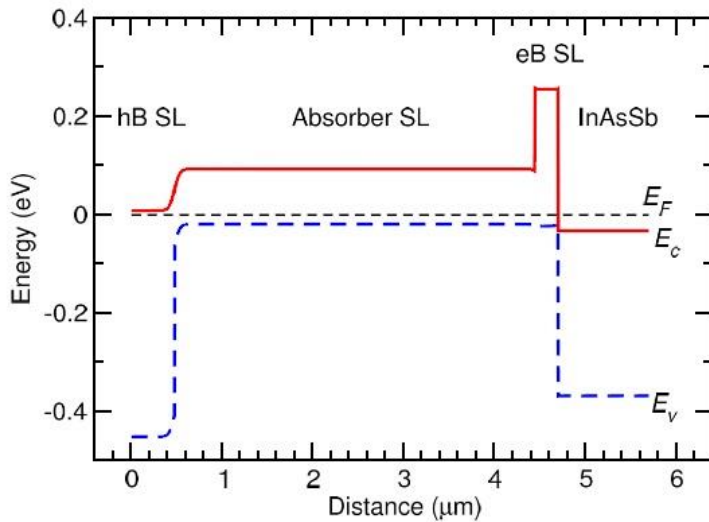


Figure 3.18: Band diagram for a CBIRD detector, showing the hole-blocking superlattice (hB SL) and electron-blocking superlattice (eB SL).²³

for the hole barrier, and 4 ML InAs / 4 ML AlSb for the electron barrier. A band diagram for the structure is depicted in Figure 3.18. It is explained that, under small applied forward operating bias, the electric field is concentrated across the electron barrier, and that photo-

generated electrons generated in the absorber are collected by the contact layer (which is just the hole barrier layer). Photogenerated holes simply recombine (across the interface between the InAsSb layer and the electron barrier) with electrons injected at the bottom contact (the InAsSb layer). Responsivity values of 1.5 AW^{-1} and 0.9 AW^{-1} were reported for a wavelengths of $8.2 \mu\text{m}$ and $5 \mu\text{m}$, respectively.

iii) Comparison with HgCdTe dark current performance levels using Rule 07

In 2008, Tennant et. al. reported a simple expression to describe the dark current behaviour in HgCdTe as a function of cut-off wavelength and temperature.²⁴ Empirically derived using dark current data taken for optimised HgCdTe photodiodes by Teledyne Imaging Sensors, Rule 07 predicts dark current density, J, performance over 13 orders of magnitude. The expression was given as:

$$J = J_0 \exp\left(\frac{1.24qC}{k\lambda_e T}\right) \quad (3.2)$$

where $J_0 = 8367 \text{ Acm}^{-2}$, $C = -1.163$, q is the elementary charge, T is temperature, k is the Boltzmann constant and

$$\lambda_e = \lambda_{cut-off} \text{ for } \lambda_{cut-off} \geq \lambda_{threshold}$$

$$\lambda_e = \lambda_{cut-off} / \left(1 - \left(\frac{\lambda_{scale}}{\lambda_{cut-off}} - \frac{\lambda_{scale}}{\lambda_{threshold}}\right)^{Pwr}\right) \quad (3.3)$$

where $\lambda_{scale} = 0.2008$, $\lambda_{threshold} = 4.635$ and $Pwr = 0.5441$. Using these formulae, the performance of an infrared detector can be compared with that of an optimised HgCdTe device for arbitrary wavelength, i.e. without the need to consult the literature for an exactly equivalent device. In 2010, the same authors reviewed the accuracy of Rule 07 through comparison with

more recent data, and found good agreement.²⁵ Specifically, dark current densities measured were within the range 0.4x – 2.5x of those calculated.

iv) Avalanche Photodiodes for high sensitivities in extended wavelength applications

Sometimes it will be desirable to have an MWIR detector which is sensitive to very weak signals/low photon fluxes. Avalanche photodiodes (APDs) are commonly used to achieve this in long-range fibre optical applications (generally at 1.55 μm).²⁶ However, relatively few APD devices have been demonstrated at longer wavelengths. A few examples of existing longer wavelength APD structures will be explored in this section.

APDs based on InAs binary material – providing sensitivity up to 3.5 μm at 300 K – were characterised by Marshall et. al.^{27,28} High gains were demonstrated for electron injection. At the same time, virtually no gain associated with hole injection was found. These conditions (i.e. low values for $k_{\text{eff}} = \beta/\alpha$) are sufficient to suggest very low excess noise. Furthermore, it is noted that the bandstructure of InAs has large energetic separations between the Γ valley and the L and X valleys – 0.7 eV and 1.0 eV, respectively – so that carriers remain in the Γ valley (where scattering is low) to higher energies. On the other hand, the shallow curvature of the heavy hole band, which indicates strong scattering, results in the suppression of hole multiplication. An absence of band-to-band tunnelling was also noted for the electric fields ranges investigated ($<100 \text{ kVcm}^{-1}$). Surface leakage currents were observed for larger reverse bias voltages, but these were stated not to be large enough to be prohibitive of multiplication measurements. Excess noise measurements were also reported, as illustrated in Figure 3.19 for the case of electron injection in a *p-i-n* structure. Excess noise factors, F , close to or slightly beyond the theoretical limit for pure electron multiplication ($F \rightarrow 2$) were recorded. It was suggested that dead space effects were responsible for the values of $F < 2$.

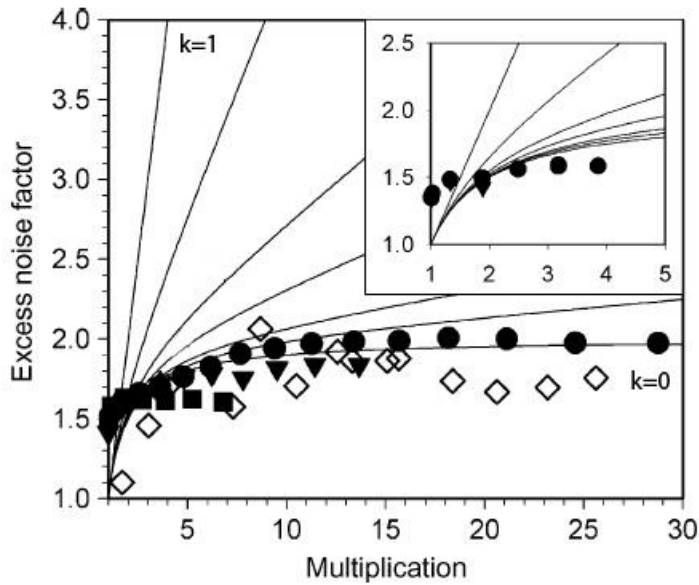


Figure 3.19: Excess noise for InAs *p-i-n* photodiodes, with 3.5 μm intrinsic region, under pure electron injection, for mesa diameters of 50 μm (\bullet), 100 μm (\blacktriangledown) and 200 μm (\blacksquare). Excess noise results are also presented for an HgCdTe APD (\diamond). The solid lines indicate $k = 0, 0.01, 0.02, 0.05, 0.1, 0.3$ and 1 under the local (McIntyre) model.²⁷ The inset shows the same measurement for devices with a 2 μm intrinsic region.

Mallick et. al. reported APDs based on a type-II 8 ML InAs / 8 ML GaSb SLS structure in 2007.²⁹ Multiplication factors in excess of 1,800 were measured at 77 K and -20 V. Excess noise factors in the range $0.8 < F < 1.2$ and multiplication in excess of 200 were measured at 120 K. However, the multiplication was noted to decrease with temperature; at 140 K it was reduced to a value of around 25. The cut-off wavelength was found, from spectral response, to be 4.14 μm and 4.92 μm , at 77 K and 300 K, respectively. IV curves exhibiting an exponential behaviour (rather than a breakdown) provided an indication of single carrier multiplication. An excess noise characteristic was also given, as shown in Figure 3.20. This also indicates single carrier multiplication (through excess noise factors $F < 2$).

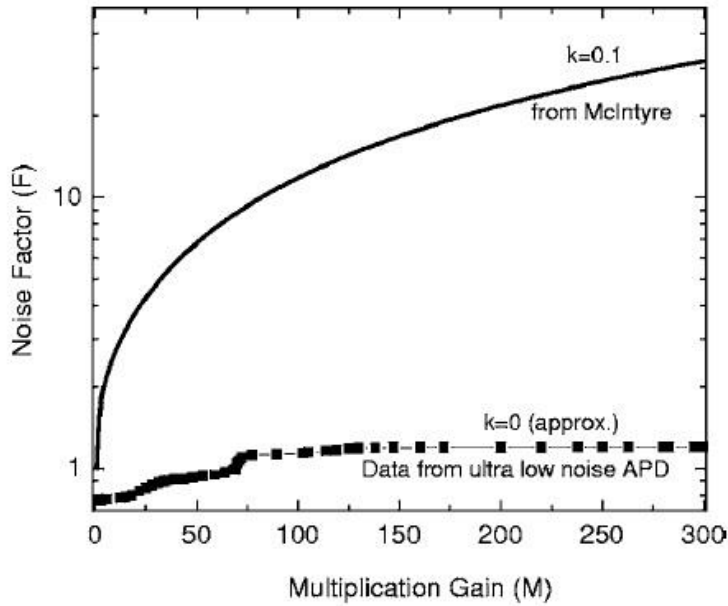


Figure 3.20: Excess noise for an 8 ML InAs / 8 ML GaSb SLS structure, measured at 120 K,²⁹ indicating single carrier multiplication through excess noise values $F \rightarrow 1$.

In 2009, Goh et. al. reported an APD based on a type-II $\text{In}_{0.53}\text{Ga}_{0.47}\text{As}/\text{GaAs}_{0.51}\text{Sb}_{0.49}$ SLS intrinsic region (with unspecified periodicity) and cladding layers of $\text{In}_{0.53}\text{Ga}_{0.47}\text{As}$.²⁸ Sensitivity in the 2 – 2.5 μm range was reported to be achieved. Low values for k_{eff} were stated to have been measured. No figures for multiplication were quoted, however.

Separate absorption and multiplication (SAM) APD structures have further been identified as an avenue to allow long wavelength sensitivity to be combined with high multiplication and low noise characteristics. Duerr et. al. reported APDs based on an $\text{In}_{0.15}\text{Ga}_{0.85}\text{As}_{0.17}\text{Sb}_{0.83}$ absorption region and an $\text{Al}_{0.55}\text{Ga}_{0.45}\text{As}_{0.05}\text{Sb}_{0.95}$ multiplication region in 2007.³¹ All layers were lattice matched to a GaSb substrate. The epilayer structure is given in Figure 3.21. Geiger mode operation was demonstrated (where the APD is biased above the breakdown voltage, so that a single photogenerated carrier can initiate a breakdown). An avalanche probability, i.e. the probability of a breakdown due to a single carrier, of 35% was reported. At 2.0 μm the QE was estimated to be around 10%, although it was suggested that this figure could be

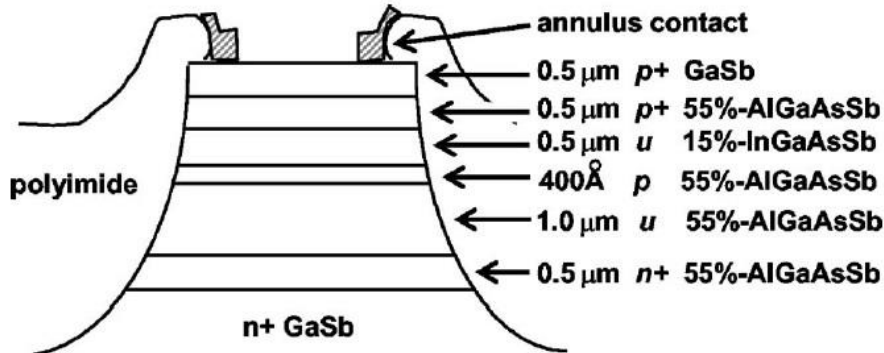


Figure 3.21: Epilayer structure for an InGaAsSb/AlGaAsSb SAM-APD structure, sensitive at 2 μm . The polyimide layer provided passivation.³¹

improved through the use of a thicker absorption region and/or an antireflective coating.

In 2004, Sulima and coworkers reported low-voltage SAM-APDs based on an $\text{In}_{0.15}\text{Ga}_{0.85}\text{As}_{0.17}\text{Sb}_{0.83}$ absorption layer and an $\text{Al}_{0.28}\text{Ga}_{0.72}\text{As}_{0.014}\text{Sb}_{0.986}$ multiplication region.³² These were grown by liquid phase epitaxy (LPE). It was stated that these materials were chosen to minimise noise, since high values of β/α (i.e. a very low electron ionisation coefficient) were known to exist for similar materials. Specifically, for $\text{Al}_{0.4}\text{Ga}_{0.6}\text{Sb}$, it was noted that $k \approx 60$ at 300 K. Responsivity values of up to 43 AW^{-1} – which were attributed to avalanche multiplication – were recorded at 2.1 μm . The authors further report comparison of the above devices with results from a conventional APD structure, made from the same absorption material, i.e. an $\text{In}_{0.15}\text{Ga}_{0.85}\text{As}_{0.17}\text{Sb}_{0.83}$ homojunction. Significantly greater dark currents were noted compared with the SAM-APD; at -8.0 V current densities of $5 \times 10^{-6} \text{ Acm}^{-2}$ and $2 \times 10^{-5} \text{ Acm}^{-2}$ were reported, for the SAM-APD and the homojunction, respectively. For the homojunction, responsivities of around 8.9 AW^{-1} were reported, again indicating multiplication, albeit of lower magnitude. No figures for multiplication were directly quoted.

Ong et. al reported a simple model to determine avalanche multiplication and noise in APD structures in 1998.³³ The model was based upon randomly generated ionisation path lengths (RPL) and a hard threshold dead space. Excellent agreement was found with results from an analytical band structure Monte Carlo model (which accounts for scattering). In particular, mean multiplication values obtained using both models were found to be in close correspondence for thin GaAs *p-i-n* diodes, even for narrow structures (50 nm thickness). However, avalanche noise was found to be slightly underestimated by the model for the narrowest devices (with 50 nm and 100 nm thickness). Results are shown in Figure 3.22. The model can be explained as follows. First, the dead space, d , experienced by an injected carrier is calculated according to $d_{e/h} = E_{th}/q\xi$, where E_{th} is the hard threshold ionisation energy (which is different for electrons and holes), q is the elementary charge and ξ is the electric field. Ionisation coefficients, α and β , are then required – commonly parameterised as a function of electric field in the literature. *Enabled* ionisation coefficients, α^* and β^* , are next calculated,

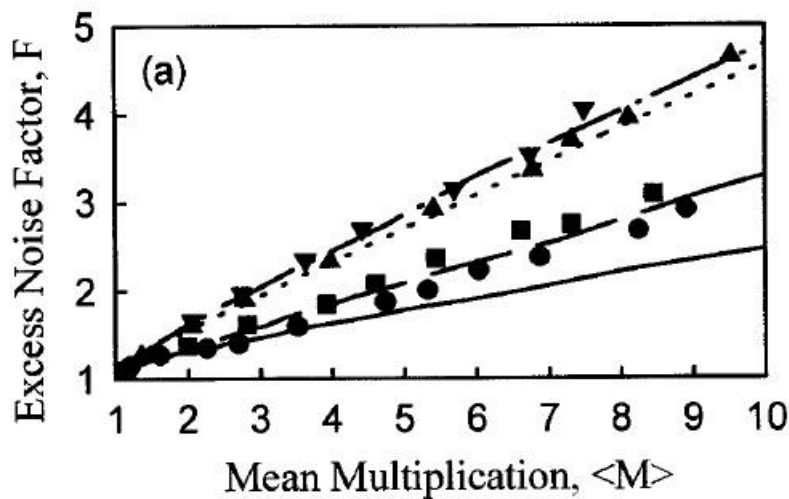


Figure 3.22: Modelled excess noise behaviour for thin GaAs *p-i-n* diodes, as simulated using a hard-threshold dead space (symbols) and an analytical-band structure Monte Carlo (lines). Intrinsic widths of 50 nm (\bullet), 100 nm (\blacksquare), 0.5 μm (\blacktriangle) and 1 μm (\blacktriangledown) were considered.³³

which represent the ionisation probability after the respective carrier has crossed the dead space (in general, measured ionisation coefficients do not account for dead space effects). These are found according to

$$\alpha^* = \frac{\alpha}{1 - d_e \alpha} \quad \beta^* = \frac{\beta}{1 - d_h \beta} \quad (3.4)$$

and ionisation path lengths, l_e and l_h , for electrons and holes, respectively, are then generated using random numbers $0 < r < 1$ according to the following formulae.

$$l_e = d_e^* - \frac{\ln(r)}{\alpha^*} \quad l_h = d_h^* - \frac{\ln(r)}{\beta^*} \quad (3.5)$$

Once functions have been coded to generate values for l_e and l_h , the average progeny of an injected electron (or hole) is simply determined using a nested loop, i.e. with an inner loop used to generate new ionisation path lengths for each generated electron and hole, and an outer loop used to carry out many trials. The excess noise factor, F , is then calculated according to $F = \langle M^2 \rangle / \langle M \rangle^2$. A further loop is used, finally, to determine M and F as a function of electric field (i.e. for various applied voltage points).

References

- [1] S. V. Ivanov, P. D. Altukhov, T. S. Argunova, A. A. Bakun, A. A. Budza, V. V. Chaldyshev, Y. A. Kovalenko, P. S. Kop'ev, R. N. Kutt, B. Y. Meltser, S. S. Ruvimov, S. V. Shaposhnikov, L. M. Sorokin and V. M. Ustinov, *Semicond. Sci. Technol.* 8, 347 (1993).
- [2] W. Qian and M. Skowronski, *J. Electrochem. Soc.*, 144, 4 (1997).
- [3] S. H. Huang, G. Balakrishnan, A. Khoshakhlagh, A. Jallipalli, L. R. Dawson, and D. L. Huffaker, *Appl. Phys. Lett.* 88, 131911 (2006).
- [4] S. Huang, G. Balakrishnan, and D. L. Huffaker, *J. Appl. Phys.* 105, 103104 (2009).
- [5] C. J. K. Richardson L. He and S. Kanakaraju, *J. Vac. Sci. Technol. B*, 29 (3) (2011).
- [6] G. R. Johnson, B. C. Cavenett, T. M. Kerr, P. B. Kirby and C. E. C. Wood, *Semicond. Sci Technol.* 3, 1157 (1988).
- [7] R. N. Kyutt, R. Scholz, S. S. Ruvimov, T. S. Argunova, A. A. Budza, S. V. Ivanov, P. S. Kopev, L. M. Sorokin, and M. P. Scheglov, *Phys. Solid State* 35, 372 (1993).
- [8] K. Akahane, N. Yamamoto, S.-I. Gozu, and N. Ohtani, *J. Cryst. Growth*, 264, 21 (2004).
- [9] Y. H. Kim and J. Y. Lee, *Appl Phys Lett*, 88, 241907 (2006).
- [10] M. Mehta, G. Balakrishnan, S. Huang, A. Khoshakhlagh, A. Jallipalli, P. Patel, M. N. Kutty, L. R. Dawson, and D. L. Huffaker, *Appl. Phys. Lett.* 89, 211110 (2006).
- [11] J. B. Rodriguez, L. Cerutti, and E. Tournié, *Appl. Phys. Lett* 94, 023506 (2009).
- [12] K. C. Nunna, S. L. Tan, C. J. Reyner, A. R. J. Marshall, B. Liang, A. Jallipalli, J. P. R. David, and D. L. Huffaker, *IEEE Photonics Technol. Lett.* 24, 3 (2012).
- [13] S. Maimon and G. W. Wicks, *Appl. Phys. Lett.* 89, 151109 (2006).
- [14] P. Klipstein, in *Proc. SPIE 6940, Infrared Technology and Applications XXXIV*, 69402U (2008).
- [15] P. Klipstein, O. Klin, S. Grossman, N. Snapi, B. Yaakovovitz, M. Brumer, I. Lukomsky, D. Aronov, M. Yassen, B. Yofis, A. Glozman, T. Fishman, E. Berkowicz, O. Magen, I.

- Shtrichman, and E. Weiss, in Proc. SPIE 7660, Infrared Technology and Applications XXXVI, 76602Y (2010).
- [16] P. C. Klipstein, Y. Gross, D. Aronov, M. ben Ezra, E. Berkowicz, Y. Cohen, R. Fraenkel, A. Glozman, S. Grossman, O. Klin, I. Lukomsky, T. Marlowitz, L. Shkedy, I. Shtrichman, N. Snapi, A. Tuito, M. Yassen and E. Weiss in Proc. SPIE 8704, Infrared Technology and Applications XXXIX, 87041S (2013).
- [17] G. Bishop, E. Plis, J. B. Rodriguez, Y. D. Sharma, L. R. Dawson and S. Krishna, *J. Vac. Sci. Technol. B* 26(3), 1145 (2008).
- [18] J. B. Rodriguez, E. Plis, G. Bishop, Y. D. Sharma, H. Kim, L. R. Dawson and S. Krishna, *Appl. Phys. Lett.* 91, 043514 (2007).
- [19] H. S. Kim, E. Plis, J. B. Rodriguez, G. D. Bishop, Y. D. Sharma, L. R. Dawson, S. Krishna, J. Bundas, R. Cook, D. Burrows, R. Dennis, K. Patnaude, A. Reisinger and M. Sundaram, *Appl. Phys. Lett.* 92, 183502 (2008).
- [20] E. Plis, J. B. Rodriguez, G. Balakrishnan, Y. D. Sharma, H. S. Kim, T. Rotter and S. Krishna, *Semicond. Sci. Technol* 25, 085010 (2010).
- [21] A. Khoshakhlagh, S. Myers, H. Kim, E. Plis, N. Gautam, S. J. Lee, S. K. Noh, L. R. Dawson and S. Krishna, *IEEE J. Quantum Elect.* 46, 6 (2010).
- [22] A. Khoshakhlagh, J. B. Rodriguez, E. Plis, G. D. Bishop, Y. D. Sharma, H. S. Kim, L. R. Dawson, and S. Krishna, *Appl. Phys. Lett.* 91 263504 (2007).
- [23] D. Z.-Y. Ting, C. J. Hill, A. Soibel, S. A. Keo, J. M. Mumolo, J. Nguyen and S. D. Gunapala, *Appl. Phys. Lett.* 95, 023508 (2009).
- [24] W. E. Tennant, D. Lee, M. Zandian, E. Piquette and M. Carmody, *J. Electron. Mater.* 37, 9 (2008).
- [25] W. E. Tennant, *J. Electron. Mater.* 39, 7 (2010).
- [26] J. C. Campbell, S. Demiguel, F. Ma, A. Beck, X. Guo, S. Wang, X. Zheng, X. Li, J. D.

- Beck, M. A. Kinch, A. Huntington, L. A. Coldren, J. Decobert, and N. Tscherptner, *IEEE J. Sel. Topics Quantum Electron*, 10, 4 (2004).
- [27] A. R. J. Marshall, C. H. Tan, M. J. Steer, and J. P. R. David, *Appl. Phys. Lett.* 93, 111107 (2008).
- [28] A. R. J. Marshall, C. H. Tan, M. J. Steer, and J. P. R. David, *IEEE Photonics Technol. Lett.* 21, 13, 866 (2009).
- [29] S. Mallick, K. Banerjee, S. Ghosha, E. Plis, J. B. Rodriguez, S. Krishna and C. Grein, *Appl. Phys. Lett.* 91, 241111 (2007).
- [30] Y. L. Goh, D. S. G. Ong, S. Zhang, J. S. Ng, C. H. Tan and J. P. R. David, in *IEEE Lasers and Electro-Optics Society, LEOS Annual Meeting Conference Proceedings 2009*, 4–8 October 2009, pp. 293-294.
- [31] E. K. Duerr, M. J. Manfra, M. A. Diagne, R. J. Bailey, J. P. Donnelly, M. K. Connors, and G. W. Turner, *Appl. Phys. Lett.* 91, 231115 (2007).
- [32] O. V. Sulima, M. G. Mauk, Z. A. Shellenbarger, J. A. Cox, J. V. Li, P. E. Sims, S. Datta and S. B. Rafol, in *IEE Proceedings - Optoelectronics*, 151, 1, February 2004, p. 1 – 5.
- [33] D. S. Ong, K. F. Li, G. J. Rees, J. P. R. David, and P. N. Robson, *J. Appl. Phys.* 83, 6, 3426 (1998).

(4) Experimental methods and modelling

Procedures used for molecular beam epitaxy (MBE) are listed in this section. In particular, compositional control was achieved using growth rate calibrations obtained using reflection high energy electron diffraction (RHEED), and substrate temperatures were sometimes calibrated using RHEED transitions also. Dopant calibrations were carried out using Hall Effect measurements. X-ray diffraction experimental procedures are also given. Device processing steps particular to nBn detectors are covered in detail. Characterisation procedures including current voltage (IV) and capacitance-voltage (CV) measurements are also treated. An electrostatic model used to simulate CV profiles allowed for modelling of device field profiles and (therefore) multiplication and excess noise behaviour, via a random-path-length model with full field dependence. These methods will be employed in sections 5-7 to obtain and fully interpret experimental results.

i) Molecular beam epitaxy

VG V80-H and Veeco Gen 930 molecular beam epitaxy (MBE) reactors were used to produce the samples detailed in this work. A simple MBE reactor schematic is illustrated in Figure 4.1. An ultrahigh vacuum (UHV) between 10^{-9} and 10^{-12} Torr is required in order to allow for sufficiently long mean free path lengths for the source elements to travel from the sources – thermal effusion K-cells for group III elements, and valved cracker cells for group-V elements – to the heated substrate assembly. This vacuum is provided by several ion pumps, as well as a cryogenic pump (cryopump), which traps gasses through condensation on a cold (~13K) surface. Cryopanel is filled with liquid nitrogen (LN₂) in order to further adsorb residual gasses and thermally isolate the cells from one another. Substrates are mounted in molybdenum (high melting point) holders, heated to the growth temperature

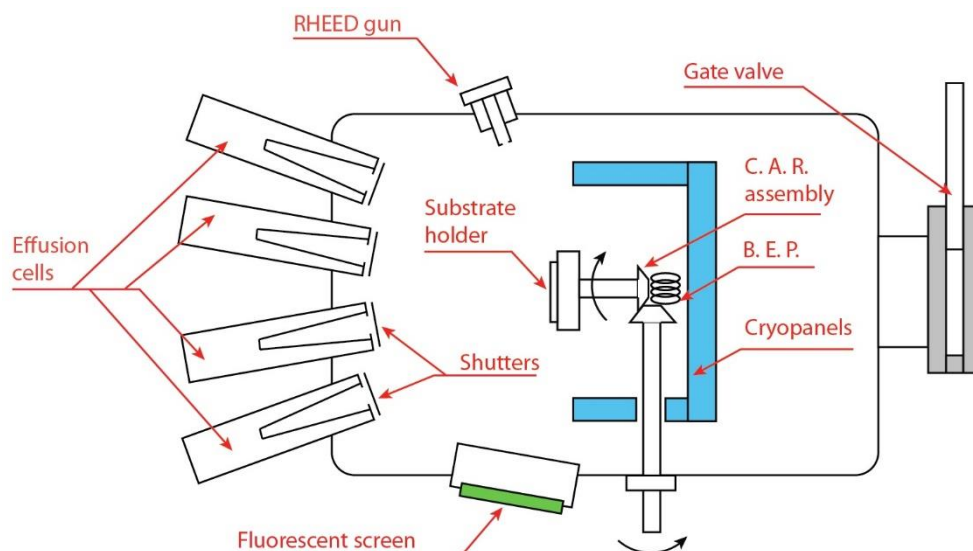


Figure 4.1: Schematic for an MBE reactor, showing the effusion cells, RHEED assembly, substrate block/heater, cryopanel and BEP gauge.

(typically 400 – 600 °C) and rotated using a continuous azimuthal rotation (CAR) assembly (in order to ensure uniform growth rates across the wafer surface). Deposition occurs via evaporation (due to heating) of the source materials from crucibles mounted in the cells which are typically made of pyrolytic boron nitride, which does not outgas (release gas) as it is heated. Group III and group V fluxes then migrate and react on the hot sample surface to form epitaxial layers. Layer thicknesses are controlled using shutters positioned in front of the sources, whereas compositions are controlled by varying cell temperatures (for group-III elements) and/or the valve positions (for group-V elements). Ion gauges are used to indicate background pressure, and can also be used to determine the flux from the sources, i.e. beam equivalent pressure (BEP). Dopant cells (Si, GaTe and Be) are temperature controlled and shuttered in the same way as the group-III cells. RHEED analysis can be used for in-situ monitoring of growth rates and layer quality. A RHEED gun, as indicated in the figure, emits a beam of electrons which arrive at the sample surface at a small angle. They are then diffracted by the uppermost layer of atoms of the sample and strike the fluorescent screen, which they excite to produce a visible pattern. Streaked reconstructions are indicative of good quality, 2D growth, whereas

spotty patterns indicate 3D (Volmer–Weber) growth, strain relaxation or a poor quality layer. The specific type of reconstruction provides an indication of the epilayer material, e.g. a 4×2 reconstruction is expected for GaAs growth. A “ $2 \times$ ” pattern has one secondary line between each pair of primary lines, whereas a “ $4 \times$ ” pattern has three, with the $2 \times$ and $4 \times$ patterns visible on the RHEED screen at orthogonal positions of the CAR assembly. These patterns originate from the surface reconstruction of the epilayer. In general, the surface will terminate with the group-V element. For the case of GaAs, the As atoms will then dimerise (to eliminate their dangling bonds) along the $\langle \bar{1}10 \rangle$ direction, which is favoured due to the position of the underlying Ga atoms along $\langle 110 \rangle$. This is illustrated in Figure 4.2. This results in a diffraction pattern which is different at orthogonal positions of the CAR assembly, i.e. the period of the pattern exhibited is shorter for the $\langle \bar{1}10 \rangle$ direction than in the $\langle 110 \rangle$ direction. In practice, As_2 dimers cannot form at every possible site due to coulomb repulsion. In fact, for the case of GaAs, dimers form at adjacent sites with two vacant sites between each pair, resulting in a surface reconstruction repeating over 4 periods of the unit cell along $\langle \bar{1}10 \rangle$ but only 2 periods of the unit cell along $\langle 110 \rangle$, hence a 4×2 reconstruction is exhibited.

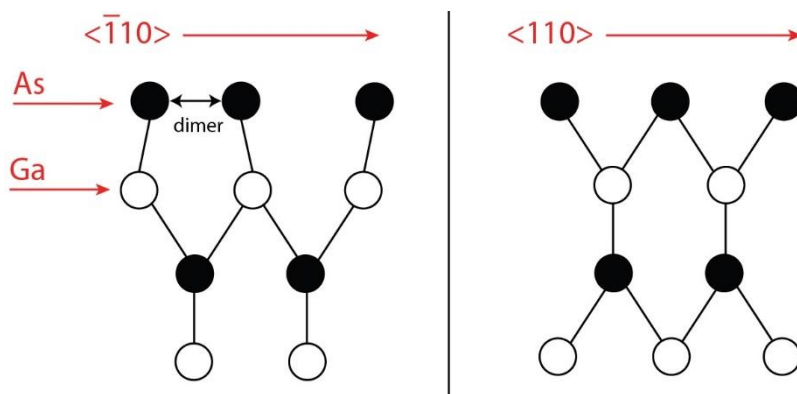


Figure 4.2: Shows the surface termination of the GaAs lattice, with the formation of an As_2 dimer along the $\langle \bar{1}10 \rangle$, but not the $\langle 110 \rangle$ direction.

The intensity of the RHEED pattern central spot further varies over the course of each monolayer of growth. When the monolayer is incomplete, the intensity of the RHEED pattern is at a minimum due to random scattering of the incident electrons by the rough surface. When the monolayer is complete, the intensity is at a maximum as a result of the increased reflectivity of the planar crystal surface. Both group-III and -V growth rates can be calibrated by recording the period of these intensity oscillations using a photomultiplier tube. Indium-bonded wafers were used to calibrate growth rates, using AlAs growth for Al, GaAs growth for Ga, InAs growth for In, GaAs growth for As and InSb growth for Sb. Group-III elements were calibrated by starting with a group V overpressure. The group III cell is then opened and the intensity oscillations recorded. Group-V elements are calibrated by depositing a covering of 5 – 10 ML of group III element on the sample before closing the group III shutter and, after a few seconds, opening the group V shutter. By measuring the group V element growth rates in this way, the sticking coefficient is taken into account (unlike for BEP-calibrated growth, where only the flux is measured). It should be noted that there is a transient effect

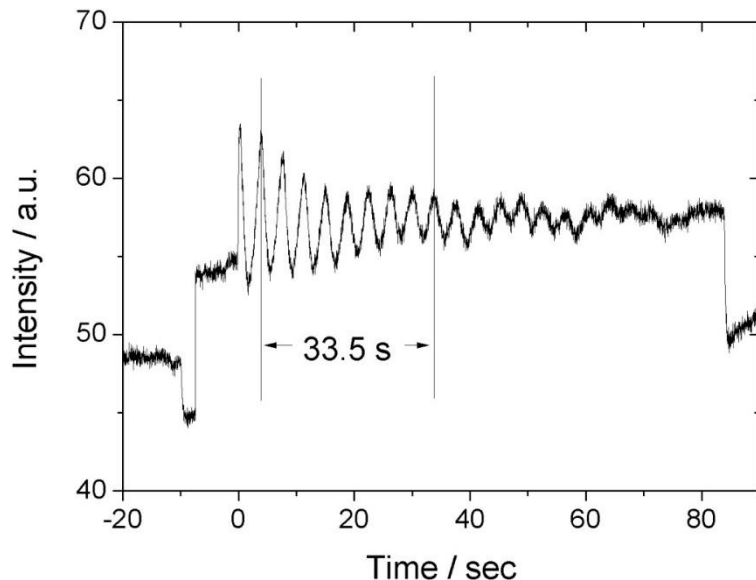


Figure 4.3: Example of a RHEED intensity oscillations plot, as obtained using a photomultiplier tube for an In growth rate calibration.

upon the growth surface temperature when group III shutters are first opened, due to radiation from the cell no longer being reflected back from the shutter. This can have an effect on the oscillation period observed in the first few seconds of the measurement, and the first few oscillations observed are generally disregarded for this reason. Figure 4.3 shows an In growth rate calibration at 730 °C cell temperature and 830 °C tip temperature. Nine periods of oscillation in period of 33.5 s indicate a growth rate of 0.27 MLs⁻¹. Once the group III elements have been calibrated, the cell temperatures required for a certain composition, x , can be found from the flux ratio, ψ , using the following equation.

$$\psi = \frac{xa_1^2}{(1-x)a_2^2} \quad (4.1)$$

It can be seen that in calculating the required flux ratio, it is necessary to take into account the difference in the epilayer lattice constants, a_1 and a_2 , of the calibration growths. For example, in calculating the fluxes required for an In _{x} Ga _{$1-x$} As epilayer, a_1 would be the lattice constant for InAs (since the In flux is calibrated using InAs growth) and a_2 the lattice constant for GaAs (since the Ga flux is calibrated using GaAs growth). For the group-V elements, no such simple relation exists, since Sb₂ and As₂ dimers compete to incorporate on the epi-surface. In this case, trial and error is required, with x-ray diffraction scans used to determine the compositions of a series of growths until the desired composition is achieved. It is further noted that the substrate temperature indicated by the thermocouple on the CAR assembly may differ significantly from the temperature of the sample surface, which has a dependence on the type of substrate (GaAs or GaSb, doped or semi-insulating) and the type of substrate holder used. It is sometimes possible to use transitions in the RHEED pattern which occur at a known temperature to calculate the offset in the thermocouple reading. In particular, when the growth of a GaSb epilayer is paused under Sb₂ flux, there is a transition between 3 × and

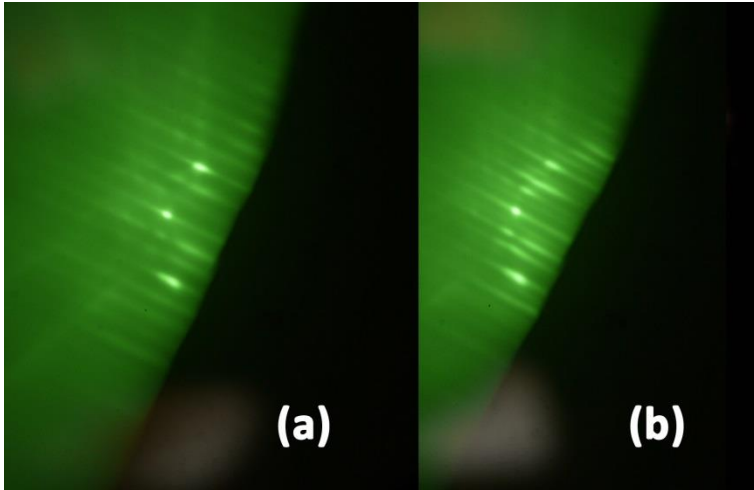


Figure 4.4: RHEED reconstruction for a GaSb layer under 1.5 MLs^{-1} Sb_2 flux (a) at $530 \text{ }^\circ\text{C}$ ($3 \times$ pattern) and (b) at $525 \text{ }^\circ\text{C}$ ($5 \times$ pattern).

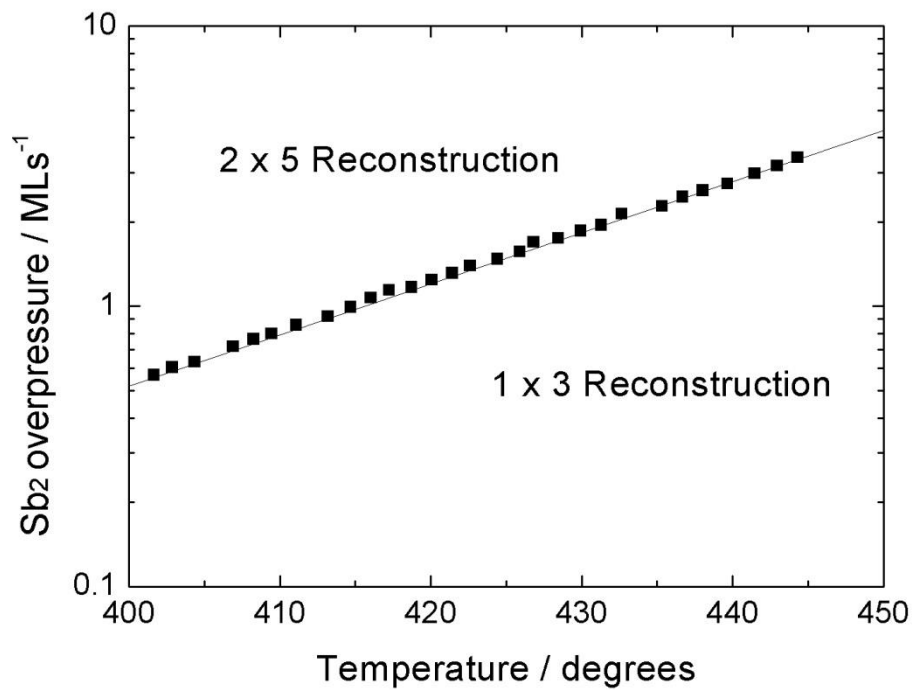


Figure 4.5: Plot showing $3 \times / 5 \times$ RHEED transition temperatures for a GaSb surface exposed to Sb_2 flux, as a function of the Sb_2 growth rate (overpressure).²

5 × reconstruction patterns occurring when the surface temperature passes through a transition temperature.¹ The transition is completely reversible, and the 3 × and 5 × patterns can be seen in Figure 4.4 (a) and (b), respectively. The particular transition temperature depends on the group-V (Sb₂) overpressure, as illustrated in Figure 4.5.

ii) Hall Effect measurement

The Hall Effect exhibits itself as a potential difference which occurs as a result of a magnetic field perpendicular to the flow of current in a sample. This potential difference, the Hall Voltage, V_h , is perpendicular to both the current flow, I , and the field, B . The direction of V_h is given by Fleming's Right Hand Rule, as shown in Figure 4.6. The Hall Voltage results from the electric field, ξ_h , which builds up to oppose the Lorentz force, F_B , on the charge carriers, given by

$$F_B = qvB = q\xi_h \quad (4.2)$$

where the mean velocity of the carriers, v , can be expressed in terms of the cross sectional area of the sample A , the carrier concentration n , and the elementary charge, q ,

$$v = \frac{I}{nAq} \quad (4.3)$$

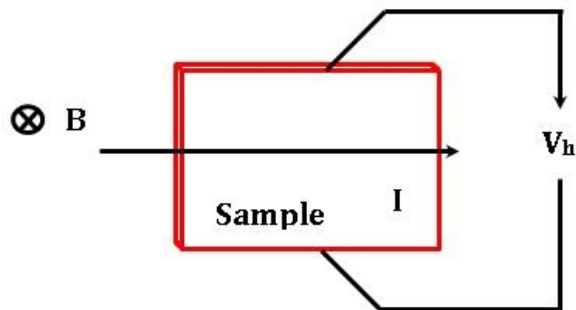


Figure 4.6: The Hall Effect results in a potential difference, V_H , orthogonal to the direction of both the current and the magnetic field.

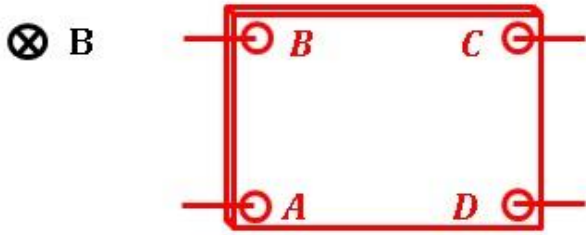


Figure 4.7: Van der Pauw measurement, with four contacts (made with In solder) positioned symmetrically at the corners of a sample.

Since $V_h = w\xi_h$ these equations can be rearranged to give

$$V_h = \frac{IB}{qnt} \quad (4.4)$$

where t is the thickness of the sample. Negative values of the carrier concentration indicate that the material is p -type. The Hall Effect can therefore be used to learn the type (electrons or holes) and density of charge carriers in a sample. In particular, Hall Effect experiments can be carried out to calibrate the dopant cells used for MBE growth. This is typically achieved with specially grown samples. By growing test layers onto semi-insulating substrates, the doping level can be measured accurately without the need to correct for the effects of conduction through a (doped) substrate. InSb epilayers – generally grown on GaAs – are generally used for this purpose. These are chosen since they easily form an Ohmic contact with the In solder used to mount the hall sample.

The Van der Pauw technique is a convenient method to determine mobility, resistivity and carrier concentration in Hall Effect samples. Generally, the test wafer is cleaved into a square piece and the contacts are affixed at as closely as possible to the corners, as shown in Figure 4.7. By defining resistances in the form R_{abcd} , determined using Ohm's law where the current

is measured between contacts A and B and the Hall Voltage is measured across contacts C and D, it is possible to express the resistivity, ρ , of the material as

$$\rho = \frac{\pi t}{\ln(2)} \frac{R_{abcd} + R_{bcda}}{2} \Phi \quad (4.5)$$

where t is the epilayer thickness and Φ is equal to one when the sample is exactly symmetrical.³ The Hall mobility, μ_h , can be calculated from the change in the diagonal resistances R_{acbd} and R_{bdca} when the magnetic field is applied, according to

$$\mu_h = \frac{t\Delta R}{B\rho} \quad (4.6)$$

and the carrier concentration is then given according to

$$n = \frac{1}{q\rho\mu_h} \quad (4.7)$$

where negative values indicate p -type material, once again. In general, these calculations are handled using a spreadsheet template.

iii) X-ray diffraction

A Bede QC200 double-crystal x-ray diffraction (XRD) system was used to perform XRD measurements. X-rays generated from a hot filament are accelerated by a strong (~ 35 kV) electric field and strike a copper target, producing Cu $\kappa\alpha_1$ and $\kappa\alpha_2$ spectral emission lines, at wavelengths of 1.541 Å and 1.545 Å, respectively. The radiation is then incident via a beam conditioning crystal on the sample. Diffraction occurs according to Bragg's law

$$2d_{hkl}\sin\theta_B = n\lambda \quad (4.8)$$

where d_{hkl} is the interplanar spacing of the crystal lattice, θ_B is the Bragg angle, n is an integer and λ is the x-ray wavelength. As a result, epilayers with different compositions – and

hence different lattice spacings – produce separate peaks in the XRD scan, i.e. different values for θ_B . The operation of the QC200 system can be understood with reference to Figure 4.8. The angle 2θ is first set according to the substrate material, e.g. 66.05° for GaAs or 60.7268° for GaSb. ω is then optimised to obtain maximum intensity for the substrate peak. A further angle, φ , is also optimised (not shown) which is just the tilt of the plate around the direction perpendicular to the page. The system then scans through a range of conditions for 2θ whilst continuously adjusting the angle ω so that diffracted rays are directed towards the detector. For samples grown lattice matched to GaSb substrates, these are generally set to ± 5000 arcsec, whereas for 6.09 \AA -lattice-constant samples grown on GaAs (i.e. IMF array samples) scans are typically carried out between $-12,500$ arcsec and $2,500$ arcsec. XRD scans are then uploaded to Bede RADS Mercury software for analysis. The RADS software prompts the user for an epilayer structure, with parameters for layer thicknesses, compositions and strain relaxation, in order to generate simulated curves. Through comparison with the experimental data and repetition, the parameters are refined, yielding experimental data for the epilayer compositions.

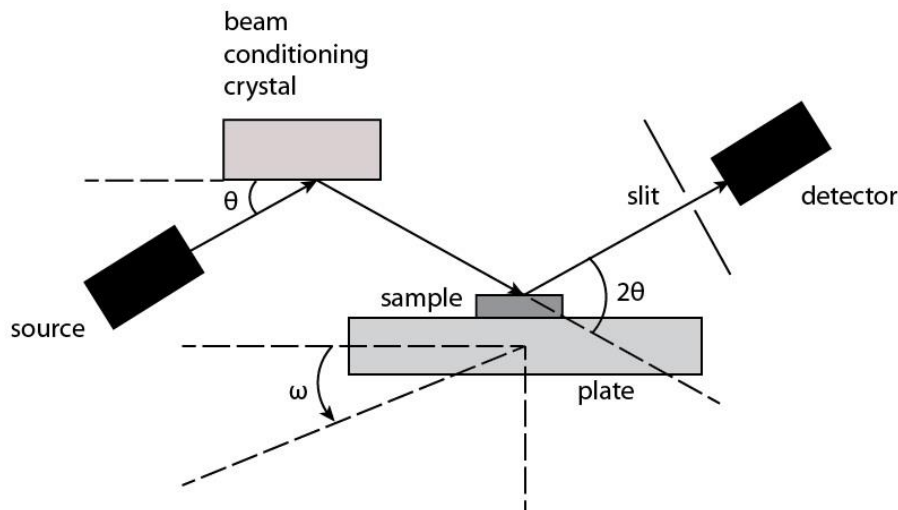


Figure 4.8: Schematic for an $\omega - 2\theta$ scan, indicating the angles ω and 2θ with respect to the source, sample and detector.

iv) Device processing

Once semiconductor device wafers have been removed from the MBE chamber, processing is required to apply metallic contacts and define mesas, as required for further characterisation. Contacts are generally applied using at least two metallic layers, where the first layer (e.g. Ti) generally acts as a barrier to prevent diffusion of the second layer metal (e.g. Au) into the semiconductor material (especially during annealing), where it can act as a dopant. The metal for the first layer should also be chosen so that its work function is approximately equal to the electron affinity of the semiconductor layer. This ensures that the absence of a Schottky barrier, and an Ohmic contact is formed. Mesas are etched using H_2O_2 in combination with an acid. The role of the H_2O_2 is to oxidise the surface of the semiconductor material, whilst the acid then removes the oxide, so that etching occurs.

The first step in processing semiconductor wafers is cleaning; this is generally achieved using three solvents, which are either heated or agitated using an ultrasonic bath. n-Butyl acetate, a more powerful solvent, is used first to remove organic residues from the sample surface. Acetone and isopropyl alcohol (isopropanol) are further used, in that order – i.e. in order of density – in order to remove stains and residues from the heavier solvents. Cotton buds can be used in combination with the n-Butyl acetate in order to aid dissolution of any residues. Residual solvent and/or water vapour is then removed by baking the sample on a hotplate.

Photolithography is then used to pattern photoresist for the evaporation of metal contacts. Steps given in this paragraph were found by following manufacturer's datasheets – given as references – but also by trial and error. A Microposit LOR 3B layer is typically applied first using a SUSS MicroTec LabSpin spinner operated at 4000 rpm for 30 s, achieving a film thickness of around 300 nm.⁴ This is then baked on a hotplate at a temperature of 175 °C for 180 s. S1805 photoresist is next applied using the same spin speed and time, and baked at 115

°C for 60 seconds.⁵ Exposure is achieved using a SUSS MicroTec MJB4 mask aligner operating at 365 nm and 325 W power for between 0.9 – 1.1 s. The sample is subsequently developed using MF-CD-26 developer for a period of 33 – 35 s. The resist is then inspected using an optical microscope; the mask has special grid features specially intended to assess over/under-development, and the process can be repeated if the results are outside of tolerance.

The function of the LOR 3B resist can be understood with reference to Figure 4.9. The LOR layer is not photosensitive, but is developed more quickly than the S1805 resist, so that an undercut is formed (illustrated in Figure 4.9d). This undercut aids lift-off through the creation

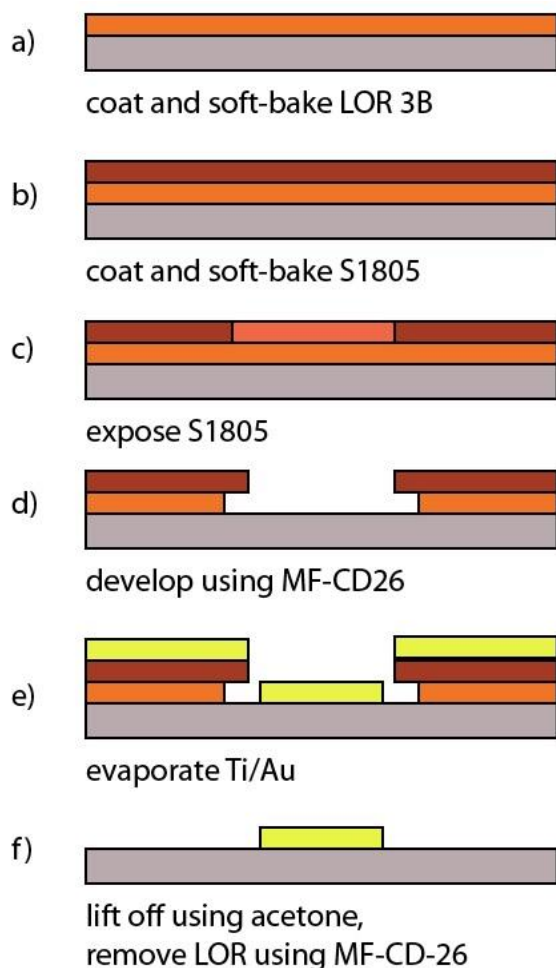


Figure 4.9: Metallisation steps illustrating the use of LOR 3B, together with and an imaging resist (S1805).⁴

of a break in the evaporated metal. It should be noted that the use of LOR resist has some-times been associated with poor adhesion of the metal contacts. It may be useful to use an HCl:H₂O (1:10) oxide-removal step prior to evaporation to aid adhesion.

Evaporation was carried out in a Moorfield MiniLab thermal evaporation system. 20 nm Ti / 200 nm Au contacts were used for *n*-type InAsSb and *p*-type GaSb. AuGe / Ni / Au and 20 nm InGe / 200 nm Au contacts were used for *n*-type and *p*-type GaAs, respectively. *n*-type GaSb contacts were achieved using 50 nm AuGe / 200 nm Au. Ti evaporation was achieved using a 41 Ampere tungsten basket source from Kurt J. Lesker (EVB12B3025W), which was found to have a suitable resistance in order to obtain the temperatures required. In particular, it is important to allow the Ti metal to become molten before exposing the samples to the evaporated metal (i.e. opening the shutter). This can be achieved by paying close attention to the evaporator pressure, which will drop sharply upon melting due to the trapping effects of Ti sublimation. Au, AuGe and InGe were evaporated from alumina coated baskets from Megatech LTD (NC-11). Sources were cleaned using an ultrasonic bath (in acetone) and heated under vacuum to their operational temperature for several minutes (“firing”) prior to first use. The source materials are also cleaned prior to evaporation, again using an ultrasonic bath. Thicknesses were monitored using QPod software through a reference crystal resonating at a varying frequency (between 5 – 6 GHz) depending on the total volume of evaporated material. The software requires that the metal density and Z-ratio are input as parameters – these are commonly available online.⁶ Once the evaporation is complete, the sample should be immersed in acetone for 5 mins before agitation is briefly applied to complete the lift-off. It is important that lift-off is fully complete before the sample is removed from the acetone since any loose metal will stick permanently to the sample if allowed to dry (due to Van der Waals forces). The LOR layer is not removed by the acetone, but can be easily removed using MF-CD-26 developer solution (through immersion for ~35 s). S1805 photoresist is then applied to the

sample once more, and patterned for mesa etching. Semiconductor etching was generally achieved using wet-chemical etchants. In particular, InAsSb material can be etched using $C_6H_8O_7:H_2O_2$ (2:1), where the $C_6H_8O_7$ solution is prepared at a ratio of 1 g $C_6H_8O_7$ solid / 1 ml deionised water (DIW). In particular, this etchant is almost perfectly selective for InAsSb epilayers over Al(Ga)AsSb *nBn* barrier layers. HCl: H_2O_2 : H_2O (1:1:5) etchant was used to etch GaSb, as well as Al(Ga)AsSb. However, this etchant is not selective for (i.e. etches) InAsSb. $H_3PO_4:H_2O_2:H_2O$ (1:1:10) solution can also be used to etch InAsSb. Etchants were generally found from ref [7], which provides an exhaustive index of the literature relating to etch recipes, given by material. Etch depths were monitored using a KLA Tencor Alpha Step IQ surface profiler. Finally, the lower contact is evaporated. This can sometimes be made directly to the reverse of the wafer, assuming there is no electrical barrier (occurring e.g. due to a semi-insulating substrate or IMF array) underneath the electrically active layers. Usually, it is best practice to apply the lower contact metallisation directly to the top-side of the wafer (i.e. a top-top contact). In this case, LOR 3B and S1805 are applied again, and patterned to form a “grid” contact (illustrated in Figure 4.10) using photolithography. For *nBn* detector structures, the grid area is etched to penetrate the barrier layer before evaporation. Evaporation and lift-off are carried out once more, as detailed above.

Also indicated in Figure 4.10 are transmission line measurement (TLM) patterns for the upper and lower contact layers. These can be used to check for Ohmic contacts (indicated by a linear IV). Furthermore, if the contacts are found to be Ohmic, the resistances measured can be plotted as a function of pad separation, yielding a linear fit which allows the determination of the contact resistance, R_c and the sheet resistance R_s . R_c is the resistance associated with the interface between the metallisation and the semiconductor, which is dependent on the contact area. R_s is the resistance of the semiconductor material itself, which is dependent on

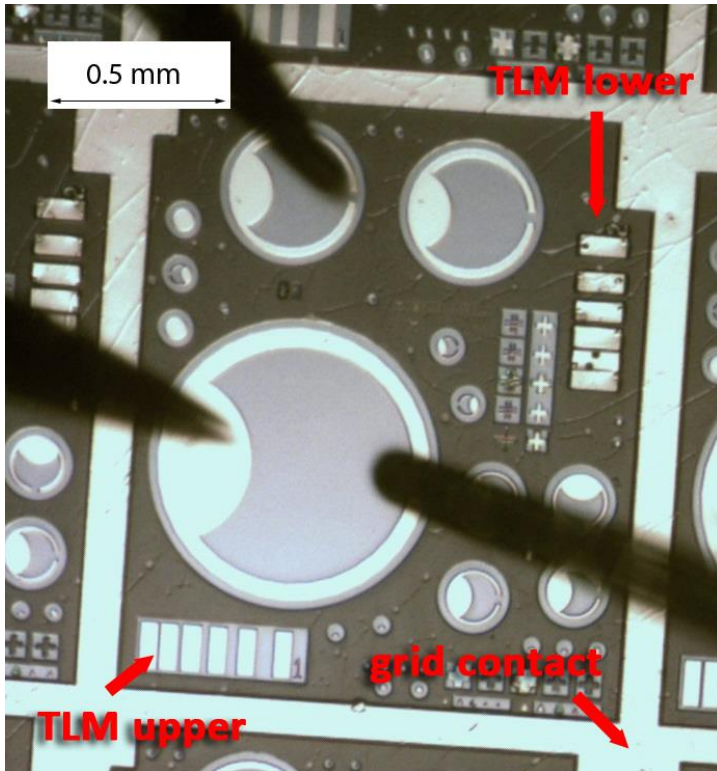


Figure 4.10: Processed wafer, with mesas of diameter 25 – 800 μm , a grid contact and two TLM patterns. Two probe tips (left) and an optical fibre (right) can also be seen.

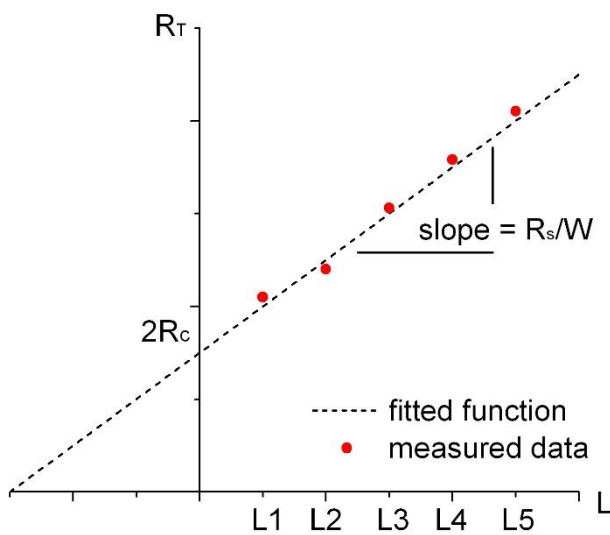


Figure 4.11: Determination of the contact and sheet resistances can be made through TLM measurements.

both the doping level and the thickness of the contact epilayer. R_s is generally measured for the lower contact, and in this case relates to the ability of the contact layer to extract current from the mesa perimeter to the lower metallisation (grid contact). As illustrated in Figure 4.11, R_c can be found from the y-intercept via $R_c = y(x = 0)/2$ and the sheet resistance, R_s , can be found via $R_s = mW$, where m is the fitted gradient and w is the width of the TLM pads perpendicular to the direction of conduction. R_c has units simply of Ω , whereas R_s has units of Ωcm^{-1} (“Ohms per square”) i.e. the units for length and width of the pads cancel, so that the dimension is simply Ohms.

v) Characterisation techniques

Current voltage (IV) measurements were carried out using Keithley 2400 and Keithley 6430 Sourcemeters. The former is a basic source-measurement unit, allowing measurements to be taken in the range between approximately 80 pA – 1 A. The latter is a low-noise unit with an external preamplifier, allowing measurements to be taken below 1 fA (though in practice our measurements were limited to a minimum sensitivity around 1 pA). The use of the Keithley 2400 system is motivated by its short integration time – providing good accuracy when set at 1 power line cycle (PLC) (i.e. 20 ms). While the Keithley 6430 meter provides superior sensitivity to small currents, there is in practice a requirement for a long source delay (>5 s), i.e. a period between the application of the voltage and the current measurement, to allow the currents to settle. Various effects, including triboelectric currents, i.e. currents generated due to friction between the insulator and the conductor within connecting cables, and/or piezoelectric effects, i.e. generation of charge by an insulator (cable sheath) under mechanical stress, can result in variations in the measured current for high impedance devices.⁸ As a result, measurements taken using the low-noise Sourcemeter are generally prohibitively slow when full temperature-dependent voltage sweeps are required, so that it is more convenient to take

measurements at a few voltage points only. Guarding may also be required, i.e. the insertion of a secondary connection between the body of the probe station and the Sourcemeter so that any current flowing through the body of the probe station (and back to the meter via paths other than through the measurement circuit) is excluded from the measurement. This is illustrated in Figure 4.12; although such currents are generally very small, they may become significant when measuring high impedance devices, e.g. nBn detectors at low temperature. All measurements were recorded using LabVIEW software.

Capacitance voltage measurements were carried out using an Agilent E4980A LCR meter. A test signal level and frequency of 25 mV and 1 MHz, respectively, were used. The meter was first corrected for the open circuit condition by probing the ground contact only. During sweeps, phase angles were monitored to ensure that the data collected was valid, through verification that the phase angle is around -90° , i.e. the device is behaving as a capacitor. Measurements were further routinely verified by taking results for various device diameters,

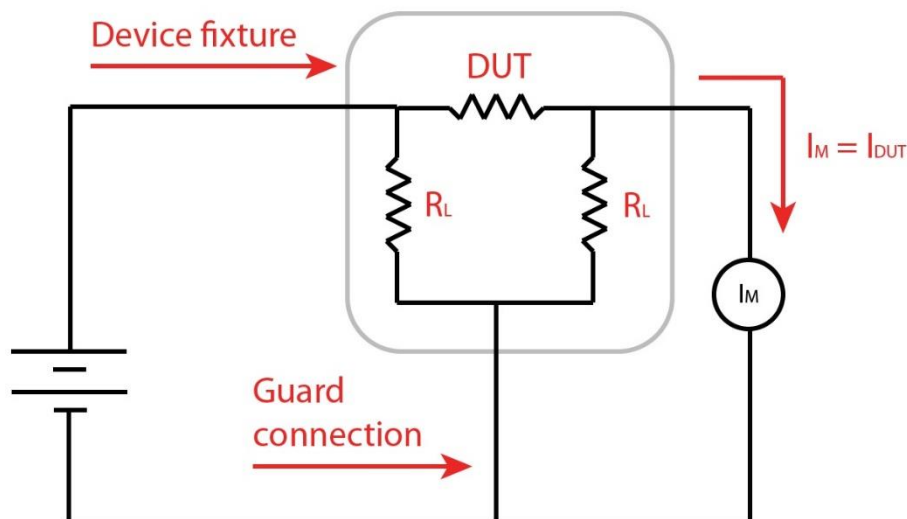


Figure 4.12: Guarding concept illustration: current flowing via R_L (the device fixture) and through the body of the probe station is excluded from the measurement at I_M , instead flowing through the guard connection directly back to the voltage source.⁸

which should scale with the device area, and at different frequencies. In particular, frequency dependent results usually indicate the presence of trap states within the depletion region. These can even result in profiles where the capacitance increases locally with increasing reverse bias. Spectral response measurements were carried out using a 900 °C blackbody source for measurements between 3 – 5 μm and an Oriel tungsten filament lamp for measurements between 1 – 3 μm . A Bentham TMc300 monochromator was used to select the wavelength whilst a Stanford Research Systems (SRS) SR570 preamplifier and SR830 lock-in amplifier were used to isolate the signal from the noise, i.e. phase-sensitive detection. Spectral response measurements were further carried out for various samples by the Center for High Technology Materials, Albuquerque, NM, USA. These were performed using a Nicolet 6700 Fourier Transform Infrared (FTIR) Spectrometer. Responsivity measurements were further carried out using an IR-563 blackbody and SRS 760 Spectrum Analyser.

Excess noise measurements were carried out using an HP8970B Noise Figure Meter operated at frequencies between 20 and 25 MHz. Calibration was carried out using the manufacturer's reference attachment. The device was connected using a 50 Ω impedance-matched cable. Bias was supplied via a Picosecond 5541A bias tee using a Keithley 2400 Sourcemeter.

nBn low frequency noise behaviour was investigated using an Agilent 35670A Dynamic Signal Analyser. Signal amplification and device biasing were achieved using an SRS 570 low-noise current preamplifier.

Low temperature results were obtained using a Lakeshore TTPX low-temperature probe station or an Oxford Instruments cryostat. Liquid nitrogen cryogen was used in both cases.

Usually, results presented in the following chapters were taken from best-case devices following screening to exclude defective devices, e.g. those damaged during fabrication. Where no statement is made, results are simply presented from typical devices.

vi) Modelling

The capacitance-voltage profiles of more complicated structures (e.g. SAM-APDs) can often be understood through the use of modelling software. It is possible to calculate the depletion behaviour, even for complicated structures, through solving Poisson's Equation in one dimension. In the case of a simple 3-layer structure – such as a *p-i-n* diode – as illustrated in Figure 4.13, the electric fields at the layer boundaries, ξ_1 and ξ_2 , can be calculated according to

$$D_1 = qN_1X_1 \quad D_2 = D_1 + qN_2X_2 \quad D_2 = -qN_3X_3 \quad (4.9)$$

where q is the elementary charge, N_i are the doping densities, X_i are the depleted widths and the electric displacement fields, D_i , are related to the electric field through $D = \epsilon_0\epsilon_r\xi$ (ϵ_0 and ϵ_r are the vacuum permittivity and the local dielectric constant, respectively). Eliminating D_1 the following expression is obtained.

$$X_3 = \frac{-qN_1X_1 - qN_2X_2}{qN_3} \quad (4.10)$$

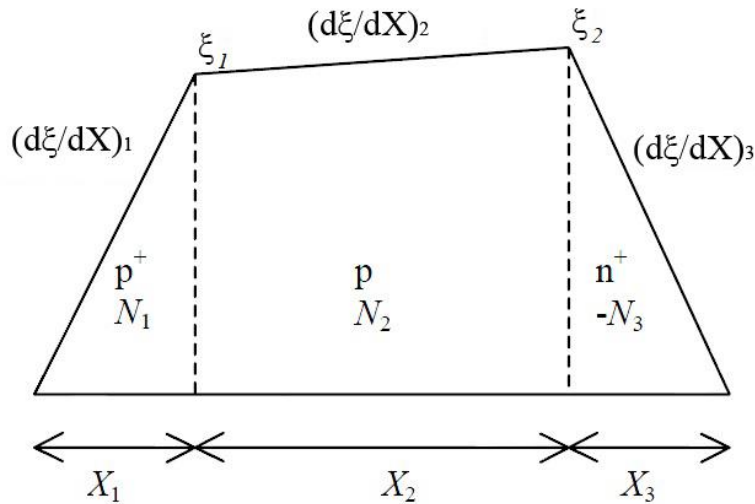


Figure 4.13: Electric field profile for a simple 3-layer structure, with thicknesses X_1, X_2, X_3 , doping densities of N_1, N_2, N_3 and boundary electric field strengths ξ_1 and ξ_2 .

Concurrently, the sum of the applied and built in voltages, V_{tot} , can be related to the integral of the electric field, according to,

$$V_{\text{tot}} = \frac{1}{2} \left(\frac{D_1 X_1}{\epsilon_1} + \frac{D_2 X_3}{\epsilon_3} + \frac{(D_1 + D_2) X_2}{\epsilon_2} \right) \quad (4.11)$$

and by substitution of Equation 4.9 and Equation 4.10 into Equation 4.11, a quadratic equation for X_1 can be obtained, given by,

$$X_1 = \frac{-b + \sqrt{b^2 - 4ac}}{2a} \quad (4.12)$$

where the coefficients are found according to the following formulae.

$$\begin{aligned} a &= N_1 \left(\frac{1}{\epsilon_1} - \frac{N_1}{N_3 \epsilon_3} \right) \\ b &= 2N_1 \left(\frac{X_2}{\epsilon_2} - \frac{N_2 X_2}{N_3 \epsilon_3} \right) \\ c &= \frac{-(N_2 X_2)^2}{N_3 \epsilon_3} + \frac{X_2^2 N_2}{\epsilon_2} - \frac{2V_{\text{tot}}}{q} \end{aligned} \quad (4.13)$$

The above approach can be extended to more complicated structures i.e. to take into account an arbitrary number of layers. This is best achieved using Maple software, since the algebra becomes particularly cumbersome. In this case, the quadratic coefficients are given by

$$\begin{aligned} a &= N_m \left(\frac{1}{\epsilon_m} - \frac{N_m}{N_n \epsilon_n} \right) \\ b &= 2N_m \sum_{k=m+1}^{n-1} \left(\frac{X_k}{\epsilon_k} - \frac{N_k X_k}{N_n \epsilon_n} \right) \\ c &= \frac{-(\sum_{k=m+1}^{n-1} (N_k X_k))^2}{N_n \epsilon_n} + \sum_{k=m+1}^{n-1} \left(\frac{X_k^2 N_k}{\epsilon_k} \right) + \sum_{k=m+1}^{n-2} \left(2N_k X_k \sum_{l=k+1}^{n-1} \left(\frac{X_l}{\epsilon_l} \right) \right) - \frac{2V_{\text{tot}}}{q} \end{aligned} \quad (4.14)$$

where the width calculated using the quadratic formula corresponds to the depleted region of the m^{th} layer, i.e. the outermost depleted layer on the p -side of the junction. The depletion in the outermost (n^{th}) layer on the n -side is simply given by the requirement for the charges to balance on each side of the junction, i.e.

$$X_n = \frac{-\sum_{k=0}^{n-1} N_k X_k}{N_n} \quad (4.15)$$

The doping densities, N_i , are negative for n -type layers. The above noted calculations require the program to first calculate the location of the layers m and n within the structure, i.e. to determine which layers are fully depleted. This is achieved by running the code in a loop, first calculating X_m and X_n for the layers closest to the junction, before considering the next layers whenever these values exceed the thicknesses of the layers under consideration. The order in which the layers are depleted is also important; this is determined by counting the charges within the layers on either side of the junction. Finally, the capacitance behaviour can be calculated from $C = \epsilon_0 \epsilon_r / d$ where d is the total thickness of the depleted volume. The electric field profile is then calculated by integration of the charge density over the depleted volume.

Once the electric field profile is known, standard integrals may be used to calculate multiplication for any structure if parameterised ionisation coefficients for the material(s) used are also known.⁹ The electric field profile is first broken down into small elements, inside which the electric field is taken to be uniform, and the ionisation coefficients calculated for each element. The following integrals are then evaluated using summations over the elements.

$$M_p = \frac{1}{1 - \int_0^w \beta(x) \exp\left(\int_x^w (\alpha(x') - \beta(x')) dx'\right) dx}$$

$$M_n = \frac{1}{1 - \int_0^w \alpha(x) \exp\left(-\int_0^x \alpha(x') - \beta(x') dx'\right) dx} \quad (4.16)$$

These integrals, together with the excess noise model of McIntyre, are predicated on the local model of impact ionisation, i.e. they neglect the effects of dead space. In order to model excess noise behaviour in a more realistic way, an RPL model with full field dependence was developed from the model of ref [10], which was discussed in Section (2). This was achieved by following the approach taken by Ng.¹¹ Once again, the electric field profile is first calculated and divided into elements. Ionisation coefficients are then calculated, in the same way as for the local model case of Equation 4.16. Enabled ionisation coefficients are then calculated, as described in Section (3) of this work. Next, the dead spaces associated with each element, for both electrons and holes, are calculated through integration of the electric field profile, again using a summation, according to

$$\sum_x^{x_k} \xi(x) \cdot dx = E_{th(e)} \quad \sum_{x_k}^x \xi(x) \cdot dx = E_{th(h)} \quad (4.17)$$

where $E_{th(e)}$ and $E_{th(h)}$ are the ionisation threshold energies for electrons and holes, respectively, ξ is the electric field, x is the position of the element and x_k is the location that the dead space associated with that element terminates. For each generated carrier, a loop is used to evaluate the ionisation probability as the carrier moves through the structure. A random number $0 < r < 1$ is first chosen. The probability of an electron ionising in a given element is found from $P_x = \alpha_x^* \cdot w_x$ where α_x^* and w_x are the enabled ionisation coefficient for and width of element x , respectively. The cumulative probability that the electron has ionised by a given position, j , C_j , is then found using a further summation as follows.

$$C_j = P_j \cdot \sum_x^{j-1} (1 - P_x) \quad (4.18)$$

When $C_j < r$ for the first time, an ionisation is determined to have taken place at j . An equivalent formula was used for holes. Over many trials, values for $\langle M \rangle$, $\langle M^2 \rangle$, $\langle M \rangle^2$ and excess noise, $F = \langle M^2 \rangle / \langle M \rangle^2$, are then determined using a further loop, as described in Section (3). A final loop is used to evaluate these parameters as a function of the applied bias, recalculating the electric field profile, ionisation coefficients and ionisation probabilities for each bias point.

References

- [1] T. H. Chiu and W. T. Tsang, *J. Appl. Phys.* 57, 10 (1985).
- [2] Eric Tournie, Institut d'Electronique du Sud (IES), Université Montpellier 2 (personal communication).
- [3] L. J. Van der Pauw, *Philips Research Reports*, 13, 1, (1958).
- [4] MicroChem, "LOR and PMGI Resists", Rev A.
- [5] Rohm and Haas Electronic Materials, "Microposit S1800 G2 Series Photoresists", Rev 0 (2006).
- [6] Vacuum Engineering and Materials, "Thin Film Evaporation Guide" (2008).
- [7] A. R. Clawson, *Mat. Sci. Eng.* 31, p1-438 (2001).
- [8] Keithley, "Low Level Measurements Handbook", 6ED.
- [9] G. E. Stillman and C. M. Wolfe, "Avalanche Photodiodes," in *Infrared Detectors II*, R. K. Willardson and A. C. Beer, Eds., vol. 12 of *Semiconductors and Semimetals*, pp. 291-393. Academic Press, New York 1977.
- [10] D. S. Ong, K. F. Li, G. J. Rees, J. P. R. David, and P. N. Robson, *J. Appl. Phys.* 83, 6, 3426 (1998).
- [11] Notes of B. K. Ng (personal communication).

(5) Results and Discussion I – Interfacial Misfit Arrays

In Section (1) a requirement for high-performance photodetector structures grown on lattice-mismatched substrates was identified. A review of literature surrounding lattice-mismatched growth was carried out in Section (3), with a view to making use of techniques developed by other groups to develop novel photodetector structures. In this section, interfacial misfit (IMF) arrays are used to grow GaSb p-i-n diodes on both Si and GaAs substrates, with an identical design further grown on a lattice-matched GaSb substrate to facilitate comparisons with the lattice-matched case. In subsequent sections, the IMF growth mode will be used to allow for lattice-mismatched nBn structures, and APDs based on previously-impossible (Al)GaAs/ GaSb heterostructures.

i) Growth of GaSb IMF p-i-n diodes

IMF arrays were used to grow GaSb p-i-n diode structures on both Si and GaAs substrates. An evaluation of material quality based on x-ray diffraction (XRD), transmission electron microscopy (TEM) and dark current measurements was then carried out. An identical structure was further grown on a GaSb substrate for the purposes of comparison, so that 3 wafers were grown in total. The epilayer structures are shown in Figure 5.1. For the sample grown on Si, a wafer miscut at 4° to [110] was used in order to reduce the formation of anti-phase domains during the growth of the GaSb overlayer, as commonly reported in the literature.¹ An AlSb buffer layer, an AlSb/GaSb superlattice (SL) threading dislocation filter and a GaSb buffer layer were grown first by workers at UCL. The native oxide was removed, through holding the substrate at 900 °C for 10 minutes. The substrate was then cooled down to 400 °C for the growth of the 10 nm AlSb nucleation layer, before being reheated to 510 °C for the growth of the GaSb buffer layer and 10-period 5nm AlSb / 5 nm GaSb SL. The SL layers act to filter

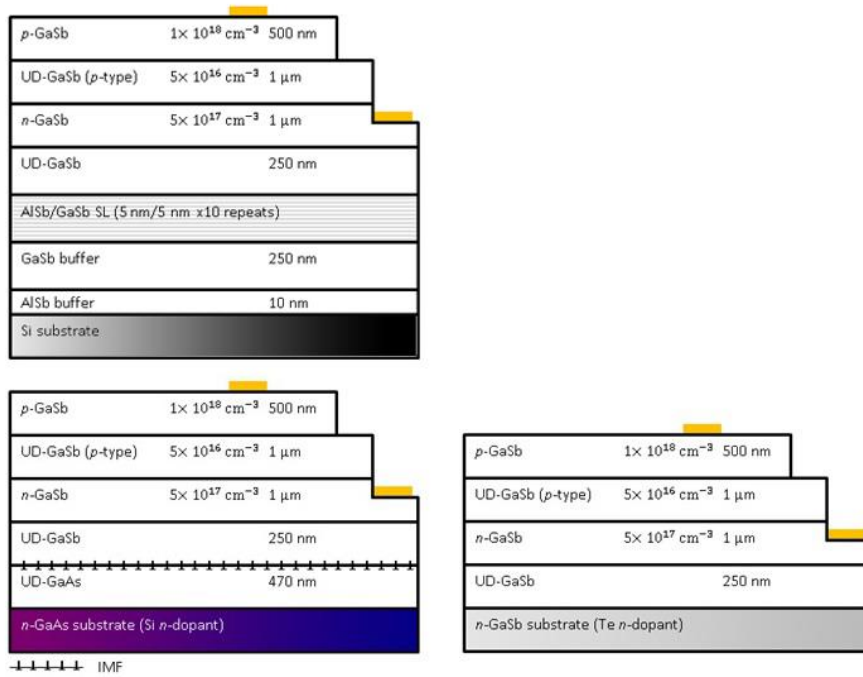


Figure 5.1: Layer profiles for the three samples. The upper three layers form a GaSb *p-i-n* structure in each case, common to the three samples.

threading dislocations. This occurs by encouraging movement of mobile threading dislocations (through additional strain applied between the layers of the SL), allowing them to react with each other and annihilate, rather than propagating into the electrically active overlayers. Growth of the GaSb *p-i-n* structure was then carried out at Lancaster. For the sample grown on GaAs, all growth was carried out at Lancaster. Oxide desorption was performed first, at 600 °C. A GaAs buffer layer was then deposited at 0.7 MLs⁻¹ and 570 °C. The IMF interface subsequently initiated, through a brief cessation of the incident As₂ flux followed by the application of Sb₂ flux. The formation of an IMF array was inferred from the observation of a 2 × 8 reflection high energy electron diffraction (RHEED) pattern. GaSb growth then proceeded. Figure 5.2 shows the evolution of the GaSb RHEED pattern from a “spotty” reconstruction, indicating 3D growth, to a streaked reconstruction, indicating a good quality, 2D epilayer. For the sample grown on native GaSb, again grown at Lancaster, oxide desorption took place at 560 °C, before growth of the *p-i-n* structure was carried out.

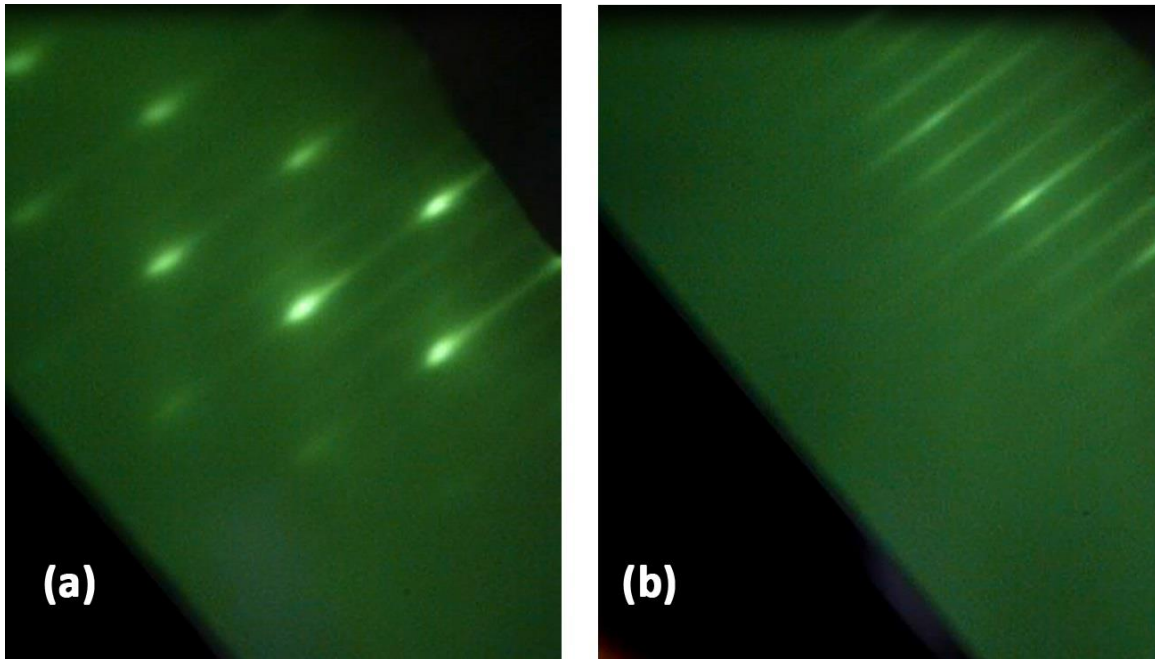


Figure 5.2: RHEED patterns for the sample grown on GaAs, after (a) 12 ML coverage of GaSb over the IMF array and (b) 48 ML coverage of GaSb over the IMF array.

Consecutive growths ensured similar growth chamber conditions for all three samples. The GaSb growth temperatures were calibrated to 510 °C through the temperature-dependent RHEED transition noted in Section (3), ensuring equal surface temperatures for the three samples (regardless of the varying thermal conductivity for the different substrates). Be *p*-type dopant and GaTe *n*-type dopant were used.

ii) XRD and TEM characterisation of GaSb IMF p-i-n diodes

XRD rocking curves are shown in Figure 5.3 for the samples grown on Si and GaAs. Figure 5.3(a) indicates a Bragg separation of 14,860 arcsec between the GaSb epilayer and Si substrate. For a fully relaxed epilayer, a separation of 15,128 arcsec is expected, i.e. the epilayer was determined to be 98.2% relaxed. Again referring to the data for the sample grown on Si, the shoulder to the left of the GaSb epilayer – around -15,000 arcsec – is due to the AlSb

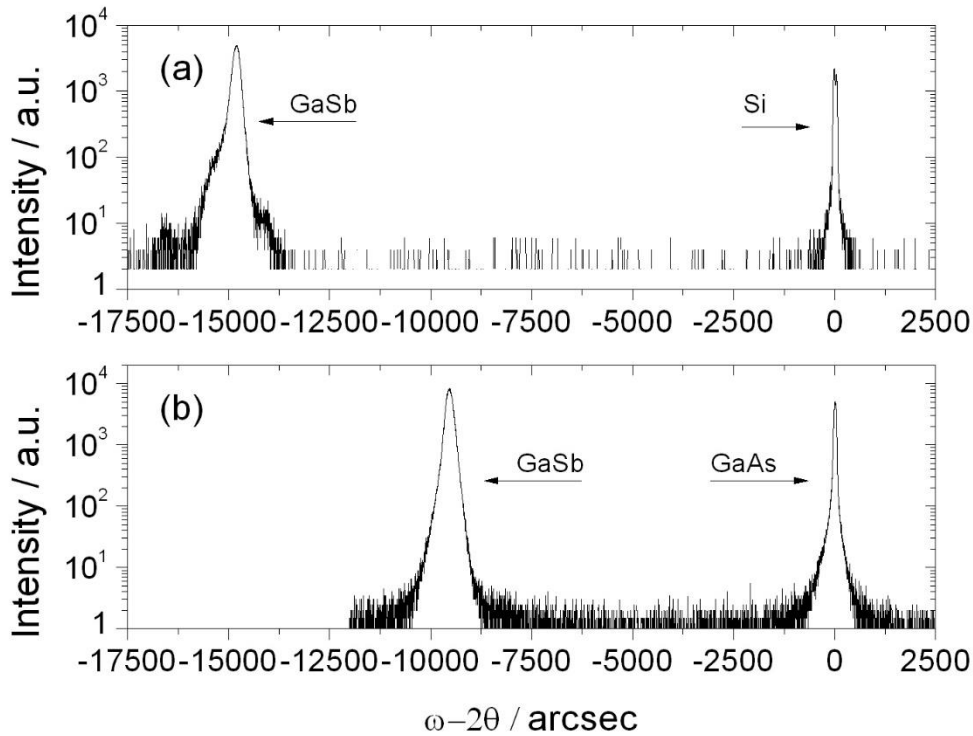


Figure 5.3: XRD data for GaSb *p-i-n* diode structures grown (a) on Si and (b) on GaAs.

buffer and SL layers. For the sample grown on GaAs – the rocking curve is shown in Figure 5.3(b) – the angular separation was 9,561 arcsec, whereas a fully relaxed epilayer would be expected to result in a separation of 9,582 arcsec – i.e. >99.7% relaxation was determined. Full widths at half maximum (FWHM) of the GaSb layers were found to be ~180 arcsec in each case. The similar FWHM in each case indicates similar crystalline quality for the two growths. Figures 5.4(a/b) and 5.4(c/d) show cross sectional transmission electron microscopy (TEM), carried out by workers at Warwick University, for the samples grown on Si and GaAs, respectively. These were based on a single specimen in each case. Inspecting part (a), it can be seen that an IMF array has been formed at the interface between the AlSb buffer and the Si substrate: a self-ordered repeating pattern consisting of 8 lattice sites of AlSb meshed with 9 lattice sites of the Si substrate. The additional lattice site is taken up by a 90° misfit dislocation. The periodicity noted can be understood in terms of the ratio $a_s : a_e$, where a_s is

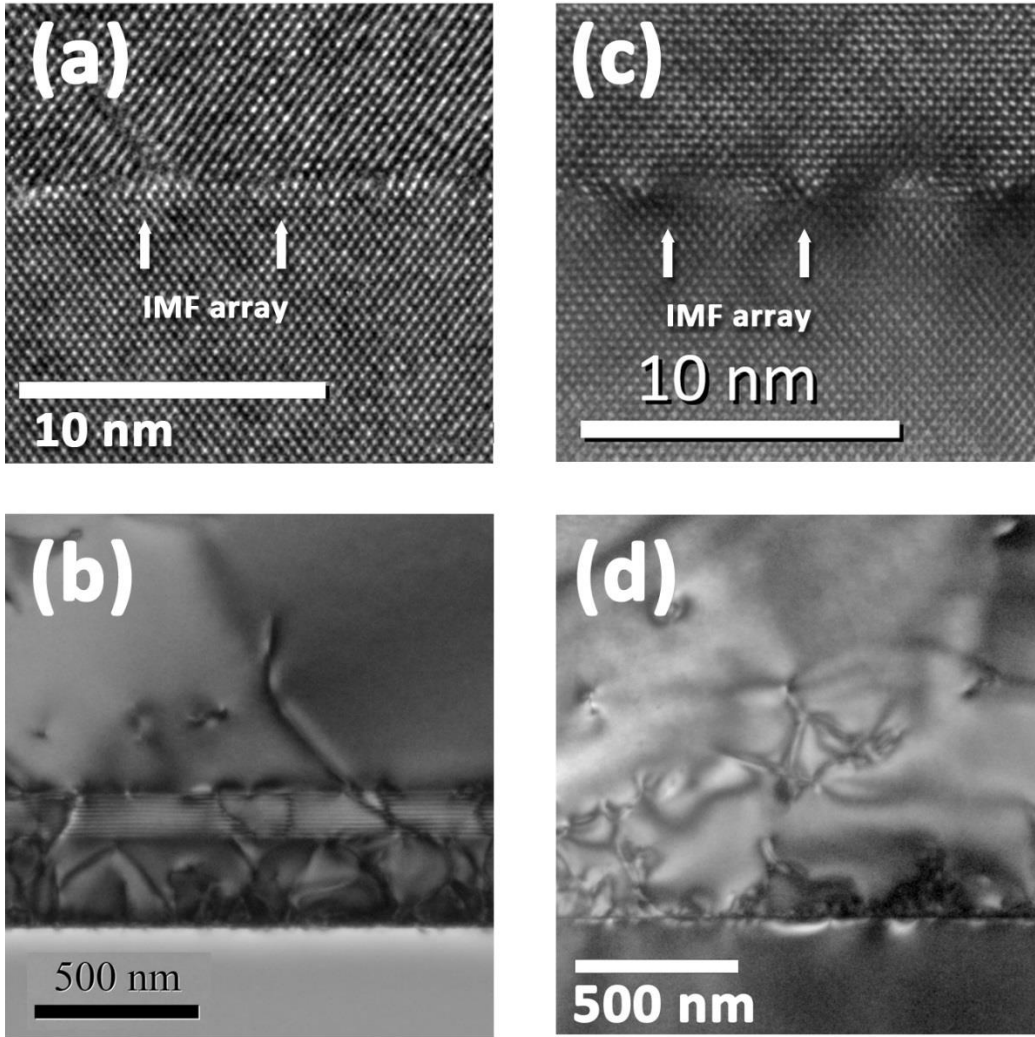


Figure 5.4: Cross-sectional TEM images of (a/b) the AlSb/Si and (c/d) the GaSb/GaAs IMF array interfaces. Parts (a/c) are presented at $400,000\times$ magnification, whereas (b/d) show the interfaces at a lower magnification ($5000\times$).

the lattice constant of the Si substrate and a_e is the lattice constant of the AlSb layer. This ratio is (almost) exactly 9:8. The separation between adjacent misfits should then be given by $9a_s/\sqrt{2} = 8a_e/\sqrt{2} = 3.47\text{nm}$. This can be compared with the spacing measured in Figure 5.4, which was found to be 3.32 nm. Part (c) illustrates the GaSb/GaAs IMF interface, and a periodicity of 14:13 can be seen, again in correspondence with $a_s:a_e$, i.e. the ratio

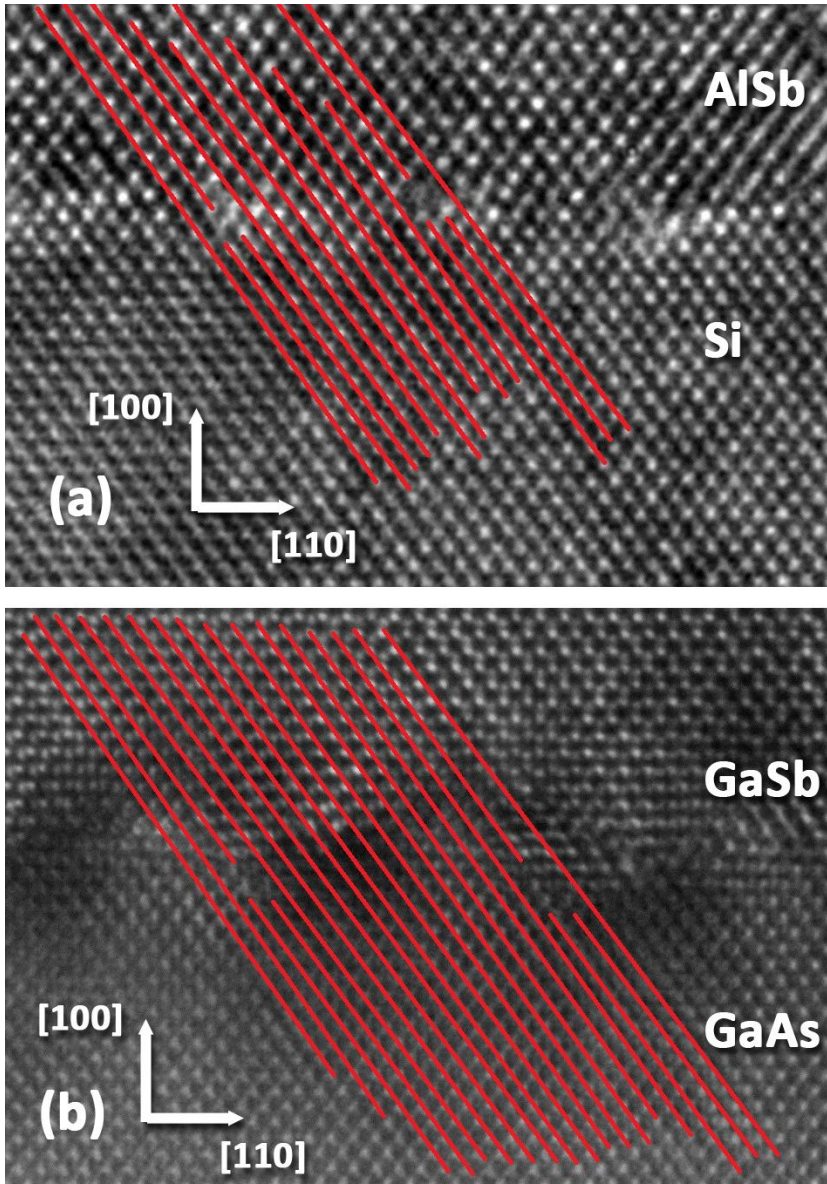


Figure 5.5: Enlarged view of Figure 4 (a/c), showing (a) the AlSb/Si and (b) the GaSb/GaAs IMF interfaces at $400,000 \times$ magnification, with the 9:8 and 14:13 periodicities highlighted.

of the lattice constants of GaSb and GaAs. The misfit spacing should be given by $14a_s/\sqrt{2} = 13a_e/\sqrt{2} = 5.6$ nm; this can be compared with a measured value of 5.4 nm (again from Figure 5.4). The periodicities are rather hard to visualise, and so are highlighted in Figure 5.5. Returning to Figure 5.4(b), the effect of the SL threading dislocation filter is evident, with the threading dislocation density (TDD) reduced by approximately one order of magnitude when comparing the GaSb regions above and below the SL. Based on counting threading disloc-

ations in tilted cross-sectional images, as illustrated in Figure 5.6, the TDD at the surface of the GaSb layer was estimated to be $\sim 1.3 \times 10^8 \text{ cm}^{-2}$. By inspection, the TDD in the buffer below the SL appears to be at least a factor of 10 greater. As illustrated in Figure 5.7, the sample grown on GaAs was calculated to have a TDD of $\sim 2.4 \times 10^8 \text{ cm}^{-2}$. In order to estimate a confidence level for these values, the number of threading dislocations occurring per area was taken to follow the Poisson distribution. The probability of 3 or fewer, and 6 or fewer, threading dislocations occurring within the specified areas, for the sample grown on Si and the sample grown on GaAs, respectively, was then plotted against a hypothetical “true”

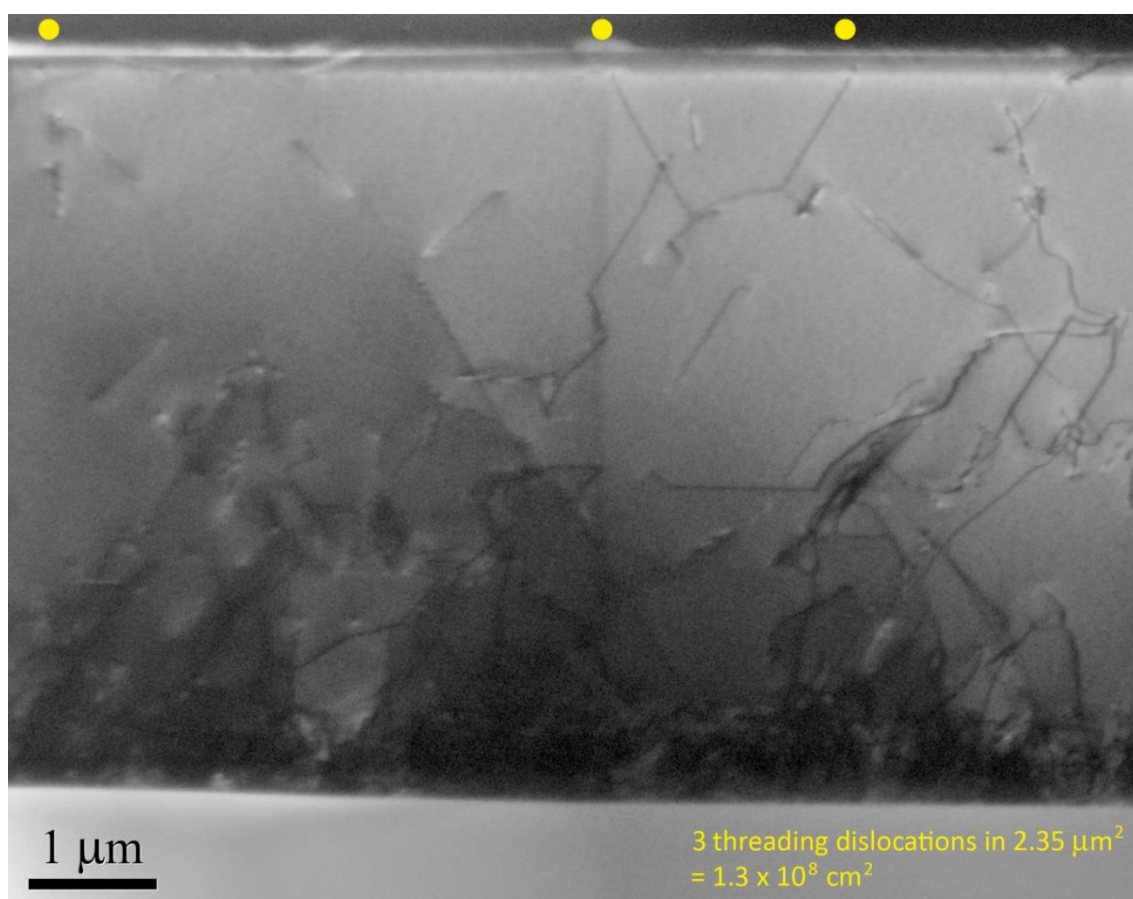


Figure 5.6: Tilted cross-sectional TEM image of the sample grown on Si, showing the propagation of threading dislocations from the AlSb/Si interface to the sample surface.

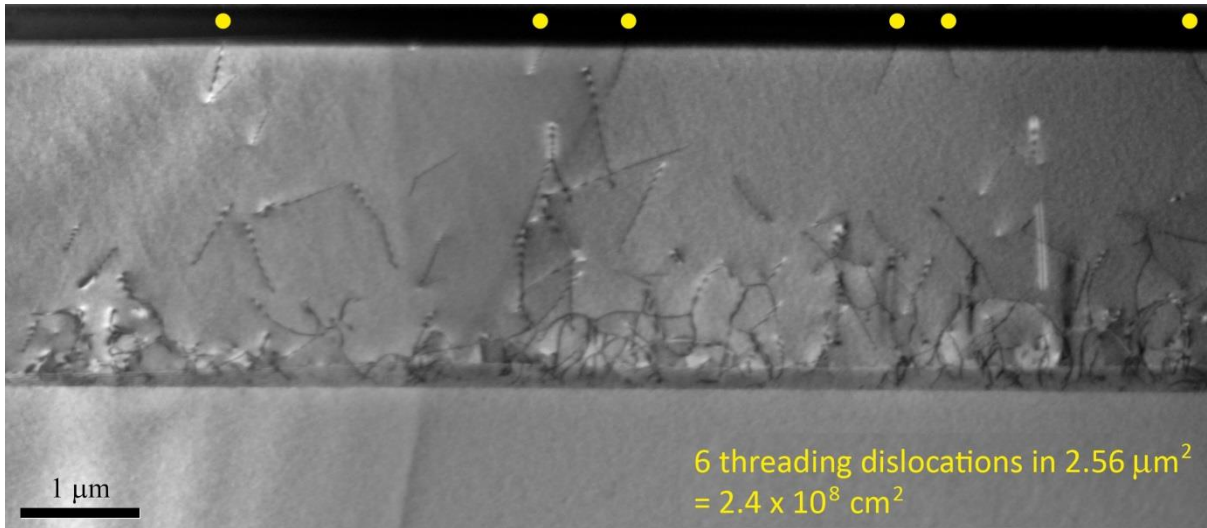


Figure 5.7: Tilted cross-sectional TEM image of the sample grown on GaAs, showing the propagation of threading dislocations from the GaSb/GaAs interface to the sample surface.

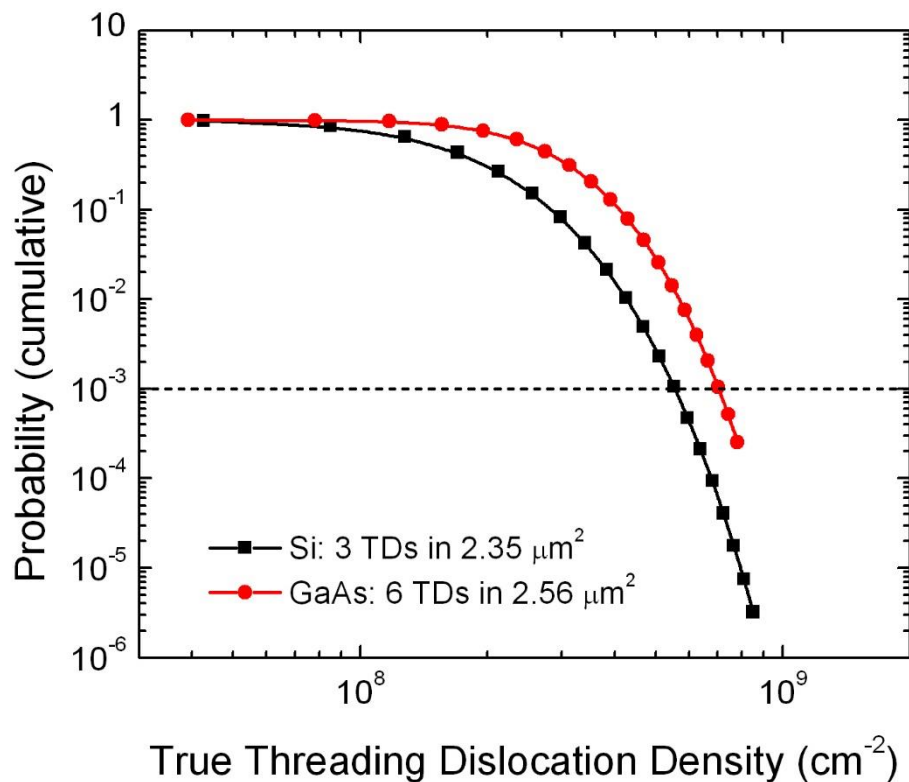


Figure 5.8: Probability of besting the quoted TDDs, from Poisson statistics, from the areas analysed in Figures 5.6 and 5.7 given a variable figure for the true TDD in each layer.

threading dislocation density, as shown in Figure 5.8. It can be seen that the probability of obtaining – at random – an area of $2.35 \mu\text{m}^2$ (on Si) or $2.56 \mu\text{m}^2$ (on GaAs) with fewer than 3, or 6, threading dislocations, for true TDDs respectively exceeding $5.6 \times 10^8 \text{ cm}^{-2}$ (on Si), and $7.1 \times 10^8 \text{ cm}^{-2}$ (on GaAs), is 10^{-3} (0.1%).

iii) Electrical and optoelectronic characterisation of GaSb IMF p-i-n diodes

Room-temperature electrical characterisation was carried out following processing (for one sample for each wafer). It was noted that the *n*-type GaSb (AuGe/Au) contacts were not quite Ohmic. However, the area of the contact was very large ($> 0.2 \text{ cm}^2$) so that the effects of any Schottky barrier should not affect the device current-voltage (IV) characteristics measured. A comparison of best current density – voltage (JV) characteristics for the three samples is shown in Figure 5.9. For the sample grown on Si, measurements were taken for many devices before analysis of data for $1 \times 100 \mu\text{m}$, $1 \times 200 \mu\text{m}$, and $3 \times 400 \mu\text{m}$ –diameter devices. The variation in the dark current density was always less than a factor of 2. The same set of device areas were analysed for the sample grown on GaAs, and a variation of less than a factor of 1.25 was exhibited. The noted area scaling of the dark currents indicates bulk-limited dark current performance for the two mismatched samples. For the sample grown on GaSb there was a significant level of variation between the dark current density for the different device diameters. Based on the best devices tested, for diameters of $100 \mu\text{m}$, $200 \mu\text{m}$ and $400 \mu\text{m}$, the dark currents were observed to scale with the perimeter length of the mesa, indicating surface limited dark currents. The best case device is shown in the figure ($400 \mu\text{m}$ diameter). It can be seen that the lowest dark currents measured were for the sample grown on native GaSb. These are compared with those of ref [2] in the figure, with the favourable comparison indicating that the quality of the other GaSb layers in this work was limited by the lattice mismatch, rather than by other factors particular to the quality of GaSb material

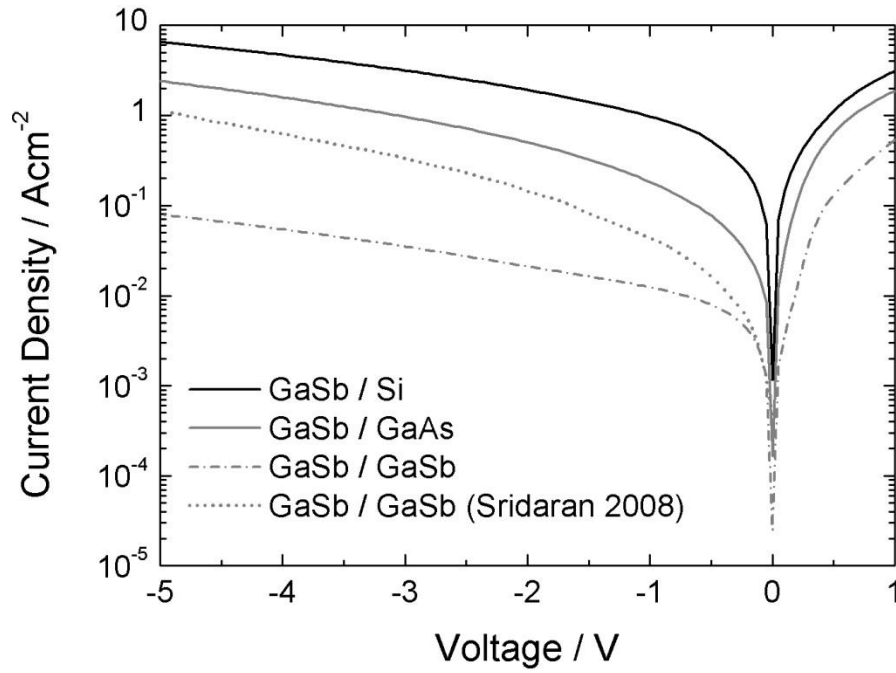


Figure 5.9: 300 K JV characteristics for the three GaSb *p-i-n* diode structures. A reference curve for lattice matched GaSb *p-i-n* diodes (grown by other authors) is also shown.

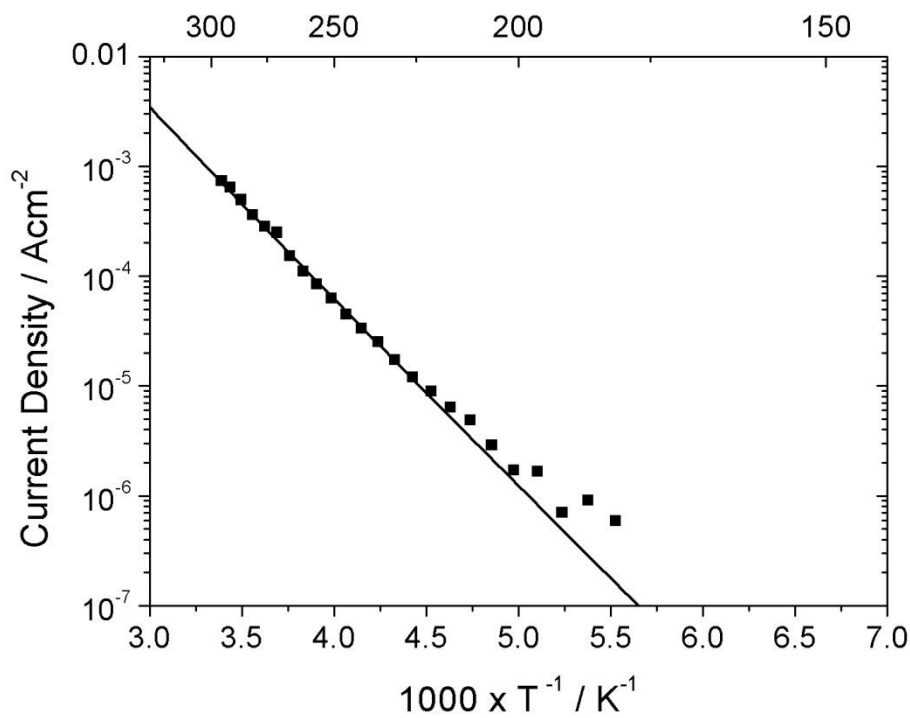


Figure 5.10: Arrhenius plot of the dark current density for the sample grown lattice-matched on GaSb, as measured for 200 μm diameter mesas at -0.1 V bias. An activation energy fitting is also shown, yielding 0.31 eV.

grown using our system (e.g. background pressure, source purity etc.). The dark current densities for the sample grown on Si and the sample grown on GaAs were both significantly greater: at -1.0 V and for 400 μm diameter mesas, current density figures of 0.9 Acm^{-2} and 0.18 Acm^{-2} , were measured, respectively. Temperature dependent JV curves (JVT) revealed weak temperature dependence for the mismatched (IMF) samples, perhaps associated with a trap assisted tunneling process. However, for the sample grown on GaSb, an activation energy of 0.31 eV – which is approximately half the GaSb low-temperature bandgap (0.812 eV) – was calculated, likely indicating SRH, bulk limited dark currents. The fitting is illustrated in Figure 5.10.

Figure 5.11 shows normalized spectral response curves for the three samples, along with fitted functions, generated using a model described in ref [3], with details given in Appendix II. Fits were carried out by first normalizing the curves so that experimental uncertainties in the total magnitude of the response did not affect the results. Chi-squared reduction was then carried out for the data between 400 – 1500 nm, using an evolutionary fitting algorithm to ensure the full parameter space was treated. The fitted parameters were then adjusted to establish confidence intervals whereby the average residual did not exceed 5%. It was found that the relative magnitude of the short-wavelength response was mainly influenced by the surface recombination velocity, which was determined to be $1.4 \times 10^5 \text{ cms}^{-1} < v_{\text{sr}} < 4.5 \times 10^5 \text{ cms}^{-1}$ (on GaSb), $3.2 \times 10^6 \text{ cms}^{-1} < v_{\text{sr}} < 4.1 \times 10^6 \text{ cms}^{-1}$ (on GaAs) and $1.1 \times 10^6 \text{ cms}^{-1} < v_{\text{sr}} < 2.7 \times 10^6 \text{ cms}^{-1}$ (on Si) – apparently correlating with the TDD values noted earlier. The minority carrier (electron) diffusion lengths were treated in the same manner and values of $1.6 \mu\text{m} < L_e < \infty$ (GaSb), $1.8 \mu\text{m} < L_e < \infty$ (GaAs) and $0.9 \mu\text{m} < L_e < \infty$ (Si) established for electrons. Note that the infinite upper bound exists as a result of the thickness of *p*-GaSb within the structure. The hole diffusion lengths were found to be

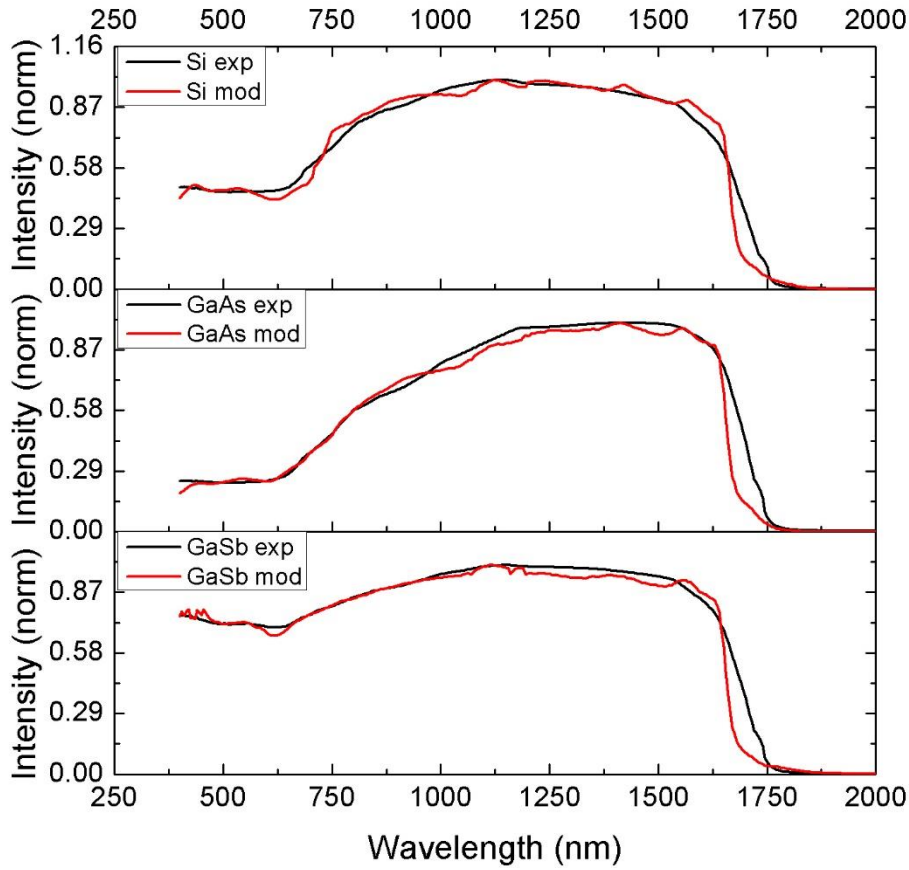


Figure 5.11: Measured and fitted response curves for the three samples, taken at zero bias. Carrier diffusion lengths and surface recombination velocities were inferred from the fittings.

$0.3 \mu\text{m} < L_h < \infty$ (on GaSb), $1.8 \mu\text{m} < L_h < \infty$ (on GaAs) and $L_h < 0.9 \mu\text{m}$ (on Si). The fact that the minimum bound for the electron and hole diffusion lengths were smaller for the sample grown on GaSb than the sample grown on GaAs was not thought to be significant in light of the infinite upper bound found from the sensitivity analysis, i.e. any value within the fitting tolerance cannot be ruled out. However, it is notable that, since the diffusion length is a function of material quality, these spectral response measurements suggest superior material in the sample grown on GaAs compared to the sample grown on Si. This is in agreement with the foregoing analysis of the dark current measurements, which showed higher dark currents for the sample grown on Si than for the sample grown on GaAs. It is further evident from the figure that the experimental cut-off wavelengths are slightly blue shifted from the modelled curves.

This was attributed to residual Moss Burstein shift in MBE-grown material. The shift was calculated to be ~ 20 meV corresponding to the Fermi Energy for an unintended doping level of $3 \times 10^{16} \text{ cm}^{-3}$. By comparison, MBE-grown GaSb is known to have a *p*-type unintended doping level of $\sim 2 \times 10^{16} \text{ cm}^{-3}$. [4] As a result, the region between 1.5 – 1.75 μm was excluded from the fitting detailed above.

iv) Discussion

A highly relaxed (98.2%) GaSb layer grown on Si using an AlSb nucleation layer was demonstrated via the IMF growth mode, exhibiting a misfit array with a periodicity as expected from the lattice constants of AlSb and Si. Streaked RHEED patterns confirmed the growth of 2D layers, as known to be promoted by the AlSb buffer layer from the Section (3). The use of a strained layer SL, which helps encourage mobile threading dislocations to travel and recombine, was shown to significantly reduce the TDD. It is noted that a similar SL could be used in the GaSb/GaAs case to reduce the propagation of residual 60° dislocations into the electrically active overlayers.

Highly relaxed, 2D GaSb films grown on GaAs substrates were confirmed through observation of RHEED patterns and XRD measurements. Furthermore, analysis of high-resolution TEM images indicated that the strain is relieved largely by an array of 90° misfit dislocations, i.e. an IMF array, with a periodicity as expected from the ratio of the lattice constants (for GaSb and GaAs). However, broad area cross-sectional TEM images have indicated higher TDDs than were reported by ref [5]: around 10^8 cm^{-2} , as compared with $\sim 10^5 \text{ cm}^{-2}$. It was also established that these values could be higher still ($>5 \times 10^8 \text{ cm}^{-2}$) if the areas analysed by TEM were highly atypical. It was noted that the same growth procedures that were detailed by ref [5] were used in this work, as carefully reproduced, including a calibrated growth temperature of 510°C , an As “desorption” step, and a “soak” under Sb_2 flux. The author feels

that the results presented in this chapter represent a fair account of the layer qualities achievable using IMF growth technique, as these results are the fruit of extensive optimisation carried out in correspondence with the group of Huang et. al. However, we have been unable to replicate the TDDs quoted in the literature. One explanation as to the higher TDDs measured – in Figures 5.6 and 5.7 – is that previous work has not reported broad area *cross-sectional* TEM results. Furthermore, ref [6] states that the misfit separation of 56 Å corresponds to exactly 13 lattice sites of GaSb and 14 lattice sites of GaAs. However, this is not exactly correct: according to ref [6] the room-temperature lattice constants GaSb and GaAs are 6.09593 Å and 5.65325 Å, respectively. Simple trigonometry then shows that 13 lattice sites of GaSb occupy ~56.0 Å along the [110] direction, whereas 14 lattice sites of GaAs occupy ~55.9 Å, i.e. an additional spacing is required for each misfit period. While the difference may be small, it is moreover noted that the thermal expansion coefficients for GaSb and GaAs differ significantly ($7.75 \times 10^{-6} \text{ }^\circ\text{C}^{-1}$ and $5.73 \times 10^{-6} \text{ }^\circ\text{C}^{-1}$, respectively)⁴ so that the lattice constants during growth (at 510 °C) differ from those at room temperature, and the additional misfit spacing noted almost doubles. Over a large epitaxial area, the additional spacing between misfits necessarily requires further dislocations to occur – possibly of the 60° type exhibited in Figures 5.6 and 5.7. Furthermore, on cooling additional strain will result, again possibly resulting in further dislocations. Another explanation for an increased threading dislocation density is island coalescence, i.e. that during the first few monolayers of growth, islands of GaSb are formed which do not necessarily have the same misfit “phase” when they meet and join together to form a 2D layer. It is noted that the area of the TEM analysis in ref [7] is narrow (250 nm cross section) so that it is possible that no 60° misfit dislocations occurred within this region. Ref [7] further shows a single *plan-view* TEM image of a GaSb/GaAs IMF sample, in support of ref [4]. Defect density figures of around $5 \times 10^{-5} \text{ cm}^{-2}$ were again reported. However, plan view

images fail to capture defects originating from the interface which reach the electrically active layers, but do not propagate to the surface.

Electrical characterisation of GaSb *p-i-n* diodes grown on GaAs substrates at Lancaster showed dark current densities higher than those observed for lattice matched devices by more than an order of magnitude: an effect potentially attributable to threading dislocations present due to the lattice mismatch with the GaAs substrate. However, there was no clear evidence in the foregoing TEM results for a higher TDD in the sample grown on Si than the sample grown on GaAs. In particular, electrical performance for the sample grown on Si was found to be weaker than for GaSb/GaAs epitaxy, with dark current densities greater by approximately a factor of 4. While analysis of the minority carrier diffusion lengths via spectral response measurements suggested longer diffusion lengths for the same grown on GaAs when compared to the sample grown on Si (through minimum bounds established for the electron diffusion length in each case) there was still an infinite upper bound in each case, as compelled by the thickness of the structure, limiting the interpretation of the data.

Figure 5.12 shows a comparison of the TDDs quoted in the literature (for GaSb grown on GaAs) from Section (3) of this work with the results obtained in this chapter. It can be seen that the results presented in this chapter are approximately in line with those of other authors who grew without a TD filter.

The above discussion might seem to reflect negatively on the potential for new photodetector structures based on IMF growth. However, it should be pointed out that the TDDs noted are not necessarily prohibitive to appropriately-designed detector structures. In particular, *p-i-n*

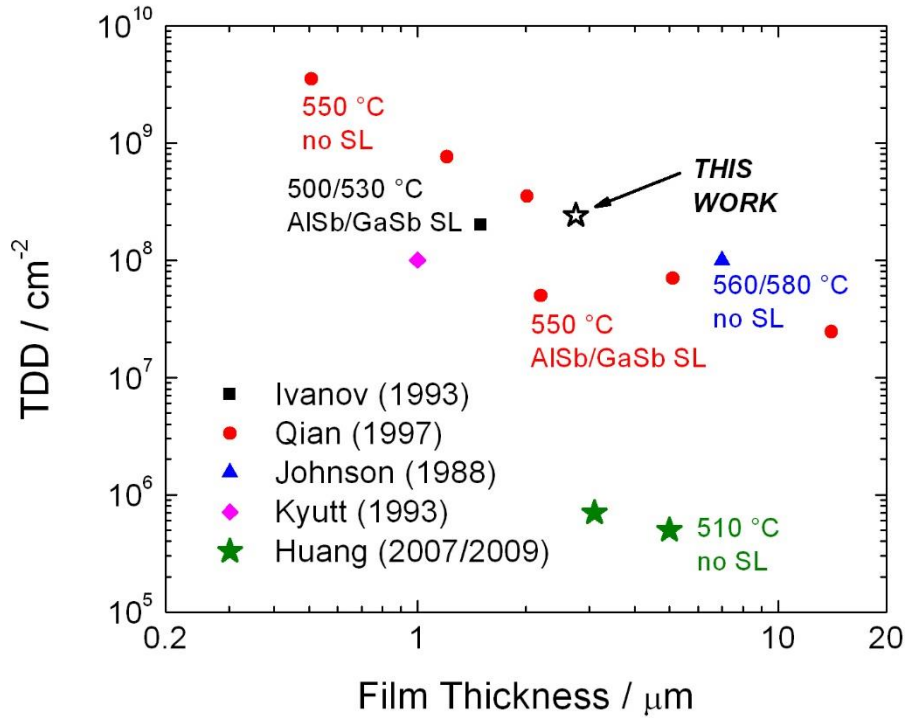


Figure 5.12: Comparison of TDDs obtained in this work (for GaSb grown on GaAs) with those from the literature. References for the above data were given in Section (3).

diodes based binary GaSb bulk-material are probably a poor choice, due to higher dark currents (by as many as 6 orders) than $\text{In}_{0.53}\text{Ga}_{0.47}\text{As}$ -based devices (for the same bandgap), even for the lattice matched case.⁸ On the other hand, detectors based on InGaAsSb quaternary material operating at $2.2 \mu\text{m}$ grown on GaAs were noted in Section (2) [Nunna] to exhibit levels of performance similar to equivalent detectors grown on native GaSb substrates. Evidently, the choice of the absorption material and the detector structure are important in designing a lattice-mismatched detector, so that the effects of threading dislocations are reduced. It was therefore decided that, in the following chapters, novel structures would be investigated with the aim of delivering photodetectors suited to lattice mismatched growth.

Substrate Material	Threading dislocation density (cm^{-2})	Dark current density at 300 K and -1.0 V (Acm^{-2})	Minority carrier electron diffusion length (μm)
Si (IMF)	1.3×10^8	0.9	> 0.9
GaAs (IMF)	2.4×10^8	0.18	> 1.8
GaSb (lattice matched)	Not measured	0.012	> 1.6

Table 5.1: Shows a summary of key figures of merit determined in this section for GaSb *p-i-n* diodes grown on Si and GaAs (via IMF) and on a native GaSb substrate.

References

- [1] J. R. Reboul, L. Cerutti, J. B. Rodriguez, P. Grech and E. Tournié, Appl. Phys. Lett 99, 121113 (2011).
- [2] S. Sridaran, A. Chavan and P. S. Dutta, J. Cryst. Growth 310, 1590 (2008).
- [3] S. M. Sze, Physics of Semiconductor Devices, 2nd ed. (Wiley Interscience, New York, 1981).
- [4] P. S. Dutta, H. L. Bhat and V. Kumar, J. Appl. Phys. 81, 9 (1997).
- [5] S. H. Huang, G. Balakrishnan, A. Khoshakhlagh, A. Jallipalli, L. R. Dawson, and D. L. Huffaker, Appl. Phys. Lett. 88, 131911 (2006).
- [6] Ioffe Institute website at <http://www.ioffe.ru/SVA/NSM/Semicond/>
- [7] S. Huang, G. Balakrishnan, and D. L. Huffaker, J. Appl. Phys. 105, 103104 (2009).
- [8] Y.-W. Chen, W.-C. Hsu, R.-T. Hsu, Y.-H. Wu and Y.-J. Chen, Jpn. J. Appl. Phys. 42, 4249 (2003).

(6) Results and Discussion II – nBn detectors for mid-infrared applications

In the previous section, IMF growth procedures were studied and the growth of relaxed, 2D GaSb layers on GaAs substrates was demonstrated. Once such a layer has been deposited, it is possible to grow further layers which are lattice matched to GaSb, such as InAs_{0.91}Sb_{0.09} – i.e. to use the GaSb layer as a virtual substrate. Novel structures based on III-Sb layers are possible as a result. In this section, the IMF growth mode was used to grow nBn detector structures on GaAs substrates. In particular, the nBn detector design was found to be suited to lattice-mismatched growth, owing to an inherent suppression of SRH recombination. When comparing nBn detector samples grown on GaAs and on native GaSb, the dark current densities measured at 200 K showed a difference of just a factor of 5. At 300 K, this was further reduced to a factor of 2. This can be contrasted with the p-i-n devices in the previous chapter, which showed a difference of 15 × at 300 K.

i) Growth of nBn detector samples

A primary nBn detector structure, as illustrated in Figure 6.1, was grown on both GaAs and on native GaSb substrates. Growth was performed at Lancaster, using a VG V80-H MBE reactor. For the sample grown on GaAs, oxide desorption was performed first, at 600 °C. A GaAs buffer layer was then deposited at 570 °C. The IMF interface was next initiated through a brief (~5 sec) cessation of group-V overpressure – allowing desorption of As from the growth surface and leaving it Ga terminated – followed by the application of Sb₂ flux. The growth temperature was then reduced to 510 °C and the sample exposed to Ga flux so that GaSb growth proceeded. The absorption layer was grown lattice matched to the GaSb buffer, at 450 °C with an extrinsic (GaTe) doping level of $4 \times 10^{17} \text{ cm}^{-3}$. The barrier layer was grown at 490 °C and included a small Ga mole fraction in order to suppress oxidation. The barrier layer was not intentionally doped; samples grown using a doped barrier layer were found to exhibit

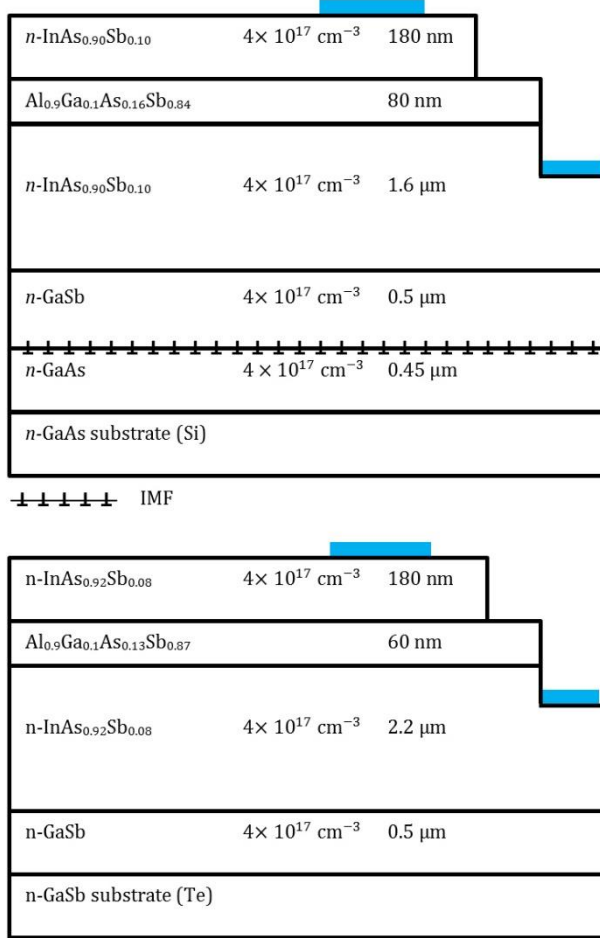


Figure 6.1: Epilayer structure for the primary samples. Top: growth on GaAs, lower: on GaSb.

electrical cross-linking between the mesas, in conflict with the analysis of Klipstein noted in Section (3). The crystalline quality of the absorption and barrier layers was monitored using reflection high energy electron diffraction (RHEED) to ensure that relaxation – which could affect the bandstructure – did not occur. This was verified through the observation of sharp, streaked RHEED patterns throughout the growth of all layers. The contact layer was grown with the same composition and doping level as the absorption layer. For the sample grown on native GaSb, oxide desorption was carried out at 540 °C, followed by the growth of a GaSb buffer layer. The nBn overlayers were then grown under the same conditions that were used for the sample grown on GaAs. Total growth rates were all approximately 1.0 MLs^{-1} . Group-V compositions were controlled using valved cracker cells. The valve positions were set based

upon calibration data collected using RHEED oscillation measurements, as detailed in Section (4). These calibrations consisted of growth rates for each valve position. Layers could then be grown with a given group-V growth rate ratio in a repeatable fashion. While the group-V composition depends primarily on the flux ratio (which is constant for a given growth rate ratio), it also depends on the growth temperature, and competition between the dimers (As_2 and Sb_2) on the growth surface. Initial growth rate ratios were 6:1 (As:Sb) for the absorption layer and 13:1 (Sb:As) for the barrier layer. X-ray diffraction measurements were then used to determine the sample composition, and a linear interpolation applied to the set growth rate ratio based upon the measured composition. Through repetition, final flux ratios of 9:1 (As:Sb) for the absorption layer and (in fact) 13:1 (Sb:As) for the barrier layer were found to yield the compositions given in Figure 6.1, which shows the two final primary wafers. Lattice matching of the barrier layer was found to be less critical than that for the absorption layer: in particular, As mole fractions in the range $0.08 < x < 0.16$ were calculated to result in a valence band offset between the absorption and barrier layers between $-16 \text{ meV} < \Delta E_v < 31 \text{ meV}$, i.e. $< 2kT$ at 200 K. Any potential barrier is also smaller than the applied operating voltage (100 – 200 mV) so that photogenerated carriers can in principle overcome any discontinuity in the valence band. Calculations were made using the model of Krijn, as detailed in Section (2). Furthermore, the change in the lattice constant over this narrow range of compositions is small enough that any residual strain is easily accommodated by the thin barrier layer. A figure showing the bandstructure for the target composition is shown in Figure 6.2. It should be noted that while compositions were repeatable for growths carried out within a few weeks of one another, some variation may occur (e.g. due to depletion of the source materials), especially over longer periods, so that recalibration may be necessary. The total group-V flux is also important, with low fluxes and/or incorrect growth temperatures sometimes resulting in defective samples (usually samples with “milky” surfaces). Growth temperatures were therefore calibrated using

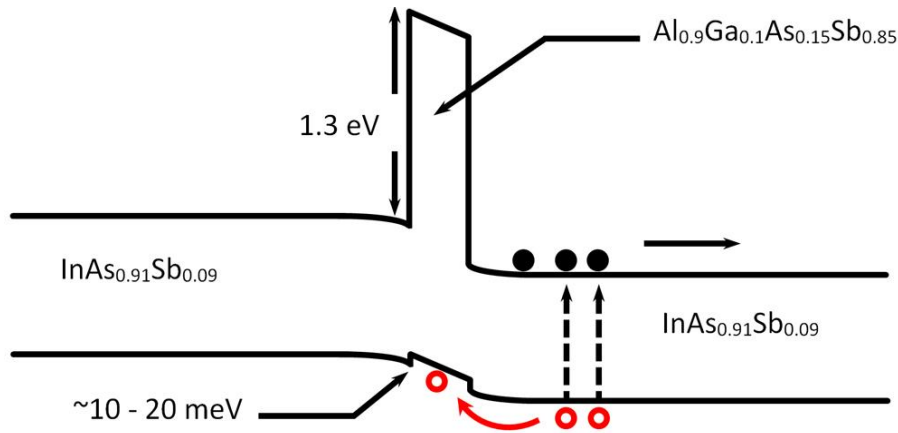


Figure 6.2: Band diagram for the primary *nBn* samples, as calculated using the model of Krijn.¹

the flux-dependent GaSb RHEED transition noted in Section (4). The true temperature of the growth surface varied from that measured by the substrate holder thermocouple depending on the type of substrate holder (2" wafer or ¼ 2" wafer), and substrate material used.

Processing was carried out using standard photolithography and wet-chemical etchants. For the wafer grown on GaAs, three samples were processed from the wafer grown, whereas two samples were processed from the wafer grown on GaSb. The processing steps were covered in the previous chapter, but the steps specific to *nBn* detectors are given here. Photoresist is first applied to the InAsSb contact layer and patterned. A metallisation (Ti/Au) was then evaporated and tested to establish that the contacts were Ohmic and had a low resistance. A further layer of photoresist was next applied and $C_6H_8O_7:H_2O_2$ (2:1) used to etch away the contact layer to define the mesas. The etchant is selective for InAsSb over AlGaAsSb for the range of compositions used, so that the barrier layer was not etched when defining the mesas. The photoresist was then removed (using acetone) and a further layer of photoresist deposited and patterned to form the lower contact. Positioned away from the mesas, this was made to the absorption layer, which was exposed by using $HCl:H_2O_2:H_2O$ (1:1:5) to penetrate the barrier layer. A further $C_6H_8O_7:H_2O_2$ step was used before evaporation to improve the quality of the InAsSb surface. The exact depth of the etching into the InAsSb absorption region was found to be unimportant

since the absorption layer experiences very little depletion. The lower contact was then evaporated, once again using Ti/Au. The contacting scheme is illustrated in Figure 6.1, with Ti/Au contact layers indicated by the blue rectangles. The separation between the mesas and the lower contact provided by the barrier layer acts as a “built-in” passivation to surface currents, as described in Section (3). It was noted that only slight oxidation of the barrier layer (with 10% Ga mole fraction) occurred, even months after processing. Oxidation could plausibly be eliminated through the use of an encapsulation layer, e.g. SU-8, further improving long term reliability.

ii) Characterisation of nBn detector samples

XRD measurements for both primary samples are shown in Figure 6.3 and Figure 6.4. The fitted curves correspond to the compositional information given in Figure 6.1. When fitting, the absorption layers were assumed to be fully strained. This is reasonable since the angular separation from the GaSb buffer layer (or GaSb substrate) is less than 250 arcsec in each case. For the sample grown on GaAs, there are no features due to the GaSb buffer layer, since it is thin and buried beneath the absorption layer. However, its position is known to be -9,580 arcsec (from the lattice constants of GaAs and GaSb). Features due to the barrier layers are visible, at around -8,000 arcsec for the sample grown on GaAs, and around 1,000 arcsec for the sample grown on GaSb. For both samples, relaxation of the barrier layer can be considered unlikely based on the model of People and Bean, as discussed in Section (2), which predicts a critical thickness $\gg 80$ nm in each case. While it is in theory possible to determine relaxation using simulated XRD curves, this is dependent on prior knowledge of the layer composition, i.e. the XRD Bragg spacing can be used to determine the relaxation if the composition is known, or the composition can be determined if the layer is known to be fully strained.

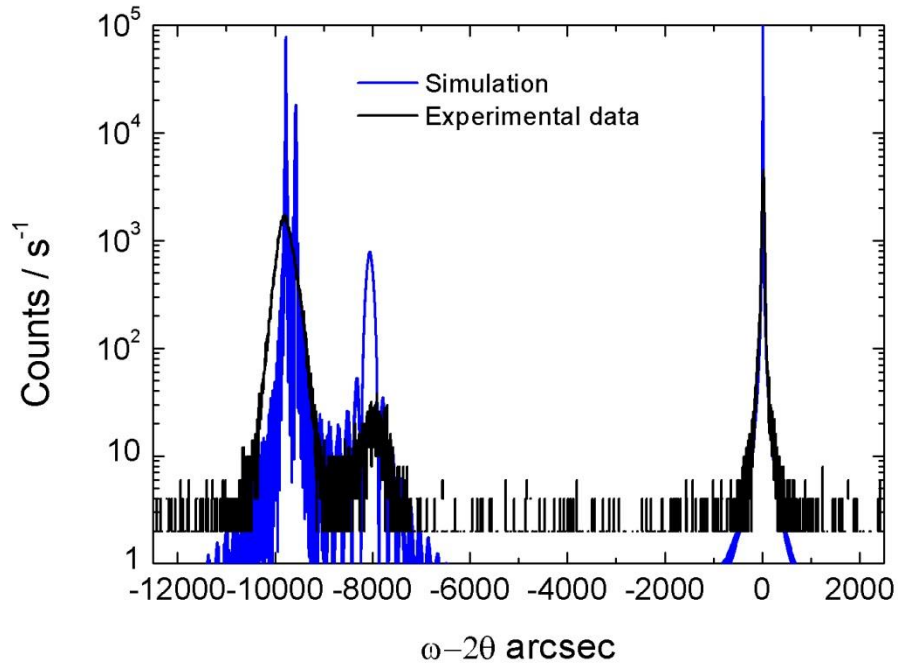


Figure 6.3: Experimental and fitted XRD curves for the primary *nBn* sample grown on GaAs.

The absorber is visible at around -9,800 arcsec. The barrier layer is visible at -8,000 arcsec.

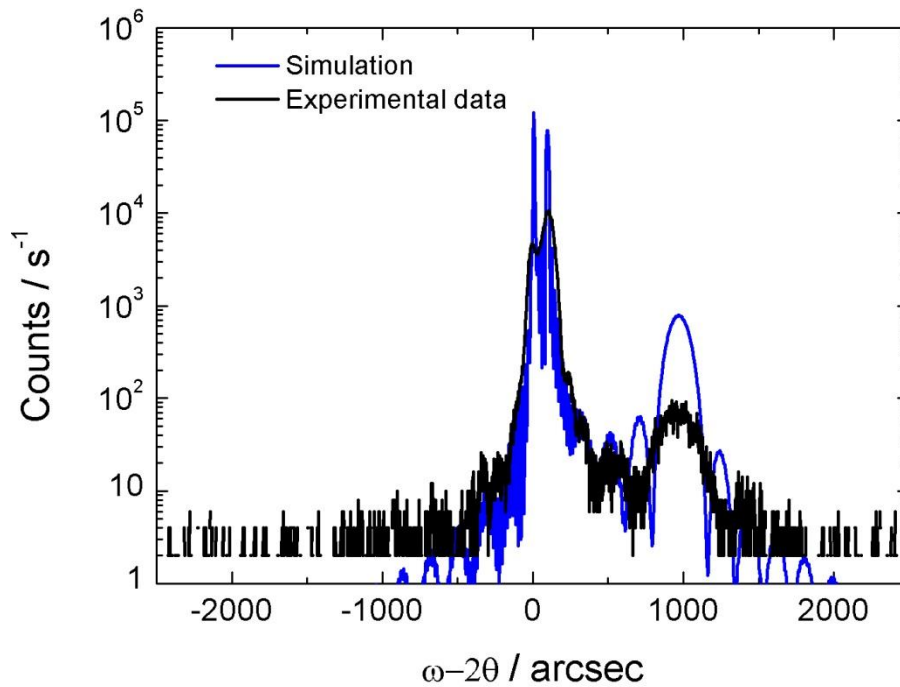


Figure 6.4: Experimental and fitted XRD curves for the primary *nBn* sample grown on GaSb.

The absorber is visible at 100 arcsec. The substrate peak has been centred.

In the case of our devices, relaxation of the barrier layer was ruled out based upon RHEED analysis and critical thickness modelling, so that the composition could be determined from the fitted XRD scans.

After cooling to 77 K, between 40 – 50 devices of 800 μm diameter were first screened to exclude defective devices. Best-case temperature-dependent (Arrhenius) plots of the dark currents for both samples are given in Figure 6.5. The fact that similar levels of performance were established for both devices is immediately striking. In particular, at 200 K, dark currents of $1.6 \times 10^{-5} \text{ Acm}^{-2}$ and $3 \times 10^{-6} \text{ Acm}^{-2}$ were measured, for the sample grown on GaAs and the sample grown on native GaSb, respectively. There was therefore around a factor of 5 difference in the dark currents resulting from the change of substrate at 200 K (and a factor of just 2 at 300 K). This can be compared with results for GaSb *p-i-n* diodes in the previous chapter, where a factor of 15 existed at 300 K. Furthermore, the 200 K dark current density is similar to that of the *p-i-n* diodes ($1.7 \times 10^{-6} \text{ Acm}^{-2}$) despite the longer cut off wavelength (3.5 μm for the *nBn* detectors compared with 1.7 μm for GaSb *p-i-n* diodes). Finally, the compositions of the two *nBn* samples are slightly different ($\text{InAs}_{0.90}\text{Sb}_{0.10}$ vs $\text{InAs}_{0.92}\text{Sb}_{0.08}$) so that some portion of the difference in the dark currents is simply due to the change in the absorption layer bandgap. Through full temperature-dependent datasets taken from 6 separate devices, an activation energy of $0.37 \pm 0.02 \text{ eV}$ was established for the sample grown on GaAs. Through datasets for 3 separate screened devices, the activation energy for the sample grown on GaSb was found to be $0.41 \pm 0.02 \text{ eV}$. These values are greater than, but close to, the low-temperature bandgap of the absorber (0.34 eV for $\text{InAs}_{0.9}\text{Sb}_{0.1}$ and 0.35 eV for $\text{InAs}_{0.92}\text{Sb}_{0.08}$),² i.e. diffusion limited dark currents were established. For both samples, the difference may be accounted for in terms of band filling effects due to the doped absorption layer. These will be discussed shortly. A line indicating the performance of an optimised HgCdTe *p-i-n* diode (via Rule 07

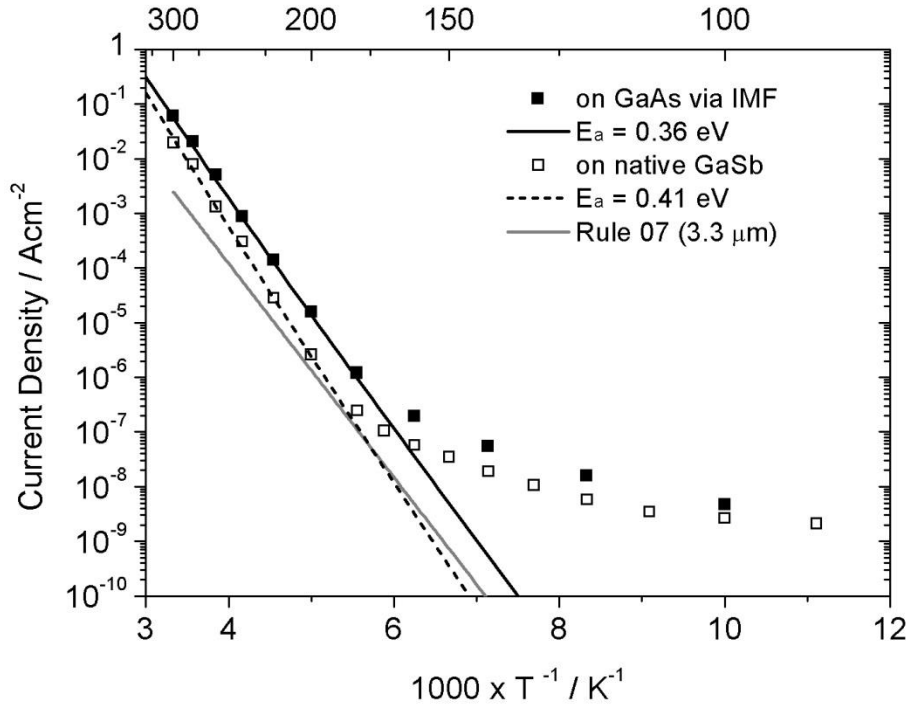


Figure 6.5: Arrhenius plots of the dark currents for both primary samples, as measured with background radiation from the 300 K scene excluded. The applied bias voltage was -0.1 V.

is also shown.³ The cut-off wavelength parameter for the Rule 07 line was set at 3.3 μm ; this corresponds to the 50% cut-off wavelength of the devices presented in this chapter (as specified by the reference). At 200 K, Rule 07 yields a dark current density of $1.3 \times 10^{-6} \text{ Acm}^{-2}$, which is close to the leakage current for the sample grown on GaSb. A second gradient is apparent for both samples in the range 125 – 175 K. In *p-i-n* diodes, this region is generally associated with Shockley Read Hall (SRH) generation in the depletion region. However, this can be ruled out (for both samples) since the associated activation energies are around 0.1 eV, i.e. significantly less than the value of $E_g/2$ which would be expected for SRH generation. These gradients are therefore likely to be associated with residual band-to-band tunnelling (in a small depleted volume of absorption material) or a shunt resistance effect associated with the barrier layer. Photocurrent due to background radiation from the 300 K scene can further be ruled out, owing to the use of a radiation shield.

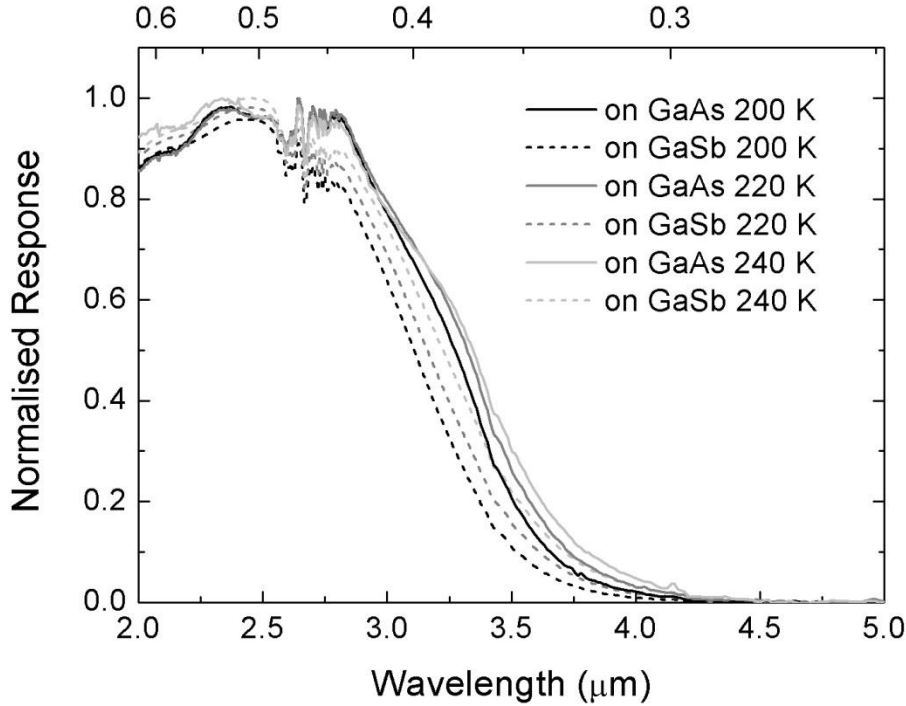


Figure 6.6: Normalised spectral response curves for the primary *nBn* samples, at temperatures between 200 and 240 K.

Spectral response curves for both samples are shown in Figure 6.6. It can be seen that the cut-off wavelengths are somewhat shorter than expected for $\text{InAs}_{0.91}\text{Sb}_{0.09}$ layers (lattice matched to GaSb) – a cut off wavelength of around $4.1 \mu\text{m}$ has been reported elsewhere for *nBn* detectors with $\text{InAs}_{0.91}\text{Sb}_{0.09}$ absorption layers at 200 K.⁴ This effect can be attributed to band filling, i.e. the population of the lowest energy states in conduction band by electrons from ionised impurities. Based upon a doping level of $4 \times 10^{17} \text{ cm}^{-3}$ a Fermi energy of 86 meV was calculated. This can be compared with the unintentionally doped case, i.e. ref [4], which is expected to have a background *n*-type doping level of around $2 \times 10^{16} \text{ cm}^{-3}$ (assuming a similar residual carrier concentration to binary InAs), and hence a Fermi energy of around 11 meV. The difference, $\Delta = 75 \text{ meV}$, is roughly in agreement with the shift in the cut-off wavelengths as predicted by ref [5]. In particular, cut-off wavelengths for the samples presented here of around $3.5 \mu\text{m}$ (on GaAs) and $3.4 \mu\text{m}$ (on GaSb) at 200 K correspond to bandgaps of 0.35 eV (on GaAs)

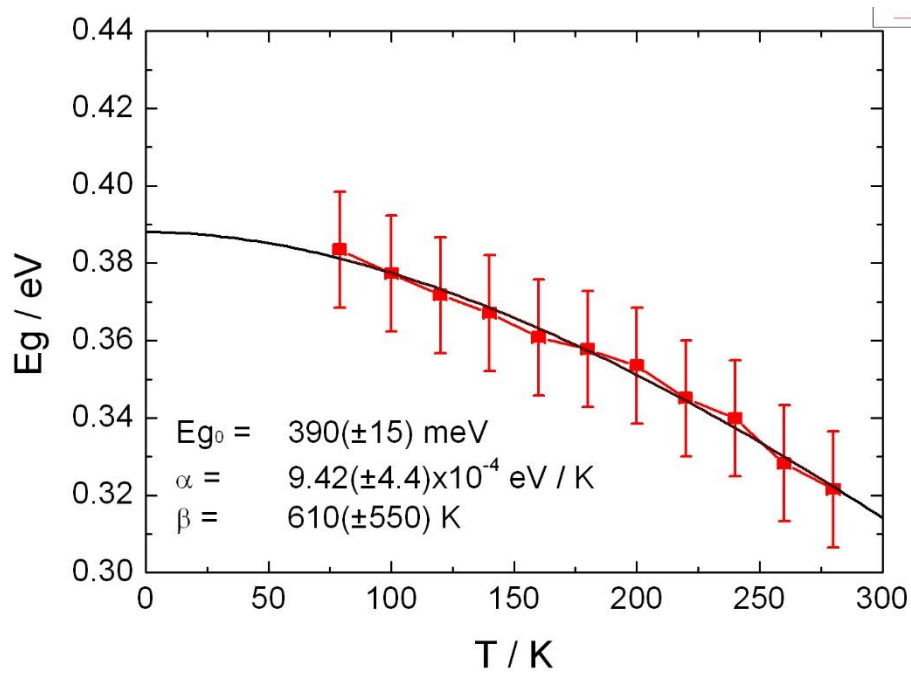


Figure 6.7: Temperature dependence of the bandgap for the primary nBn detector sample grown on GaAs (as inferred from the cut-off wavelength) with a fitted Varshni curve.

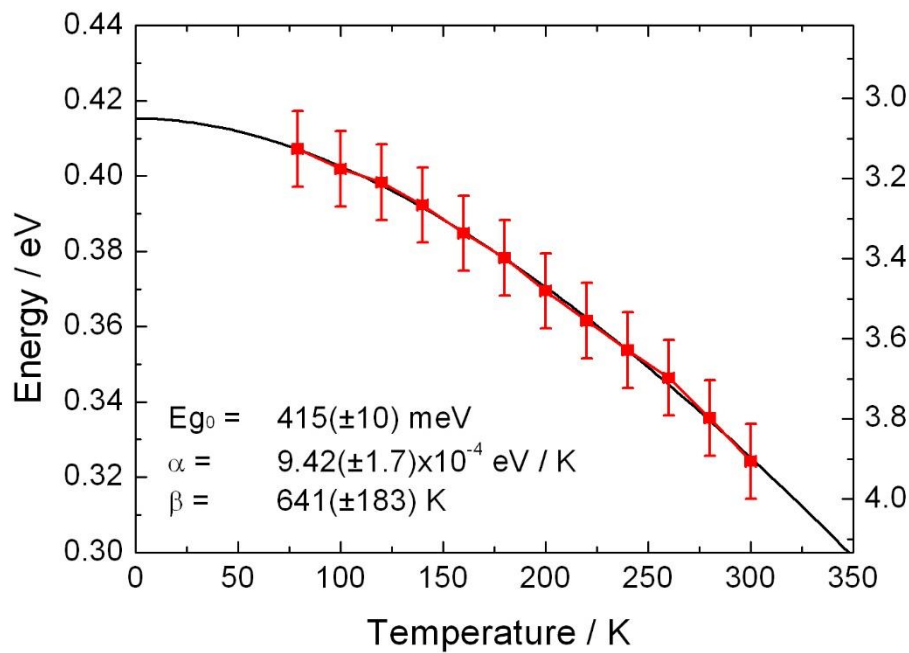


Figure 6.8: Temperature dependence of the bandgap for the primary nBn detector sample grown on GaSb (as inferred from the cut-off wavelength) with a fitted Varshni curve.

and 0.37 eV (on GaSb), whilst the noted 4.1 μm cut-off wavelength for unintentionally doped devices corresponds to a bandgap of 0.3 eV, i.e. $\Delta \approx 50$ meV and $\Delta \approx 70$ meV, respectively. All cut-off wavelengths were determined by plotting the square of the photoresponse against energy and then extrapolating the low energy region to zero. The slightly shorter cut off wavelength for the sample grown on GaSb, when compared to the sample grown on GaAs, can be attributed to its lower Sb content. Figure 6.7 and Figure 6.8 show the temperature dependence of the bandgap for the two samples, as inferred from the spectral response measurements. The error in the fitted cut-off wavelength (and hence the inferred bandgap energy) was inferred by refitting several times to determine the range of values which correspond to a perceived good quality fit. The errors shown in the figure represent this systematic fitting uncertainty. The error in the measured temperature was estimated to be ± 2.5 K since the cryostat temperature was left to stabilise for ~ 15 minutes between measurements. Whilst the fitted α and β values for the sample grown on GaAs were not known precisely, the effect of varying these parameters (across the range of the errors given) led to a variation in the low-temperature bandgap, E_{g0} , of ± 7 meV. On the other hand, the potential for a systematic error in the fitted cut-off wavelengths led to an uncertainty of 15 meV, and so the latter was taken to dominate. The larger error and reduced quality of fit for the sample grown on GaAs can be attributed to the weaker signal strength for this sample. It can be seen that the fitted low-temperature bandgaps are greater than expected for an intrinsic layer: using the bowing parameter recommended by ref [2] (0.67 eV) the low temperature bandgap is expected to be 0.34 – 0.35 eV. This can be understood in terms of band-filling, and further accounts for the larger-than-expected activation energy noted in Figure 6.5 for the sample grown on GaSb: the activation energy measured from the dark currents (0.41 ± 0.02 eV) is in good agreement with the Varshni-fitted value from Figure 6.8 (0.415 ± 0.01 eV). Finally, for the sample grown on GaAs, the dark current activation energy from Figure 6.5 (0.37 ± 0.02 eV) again agrees closely with the fitted low

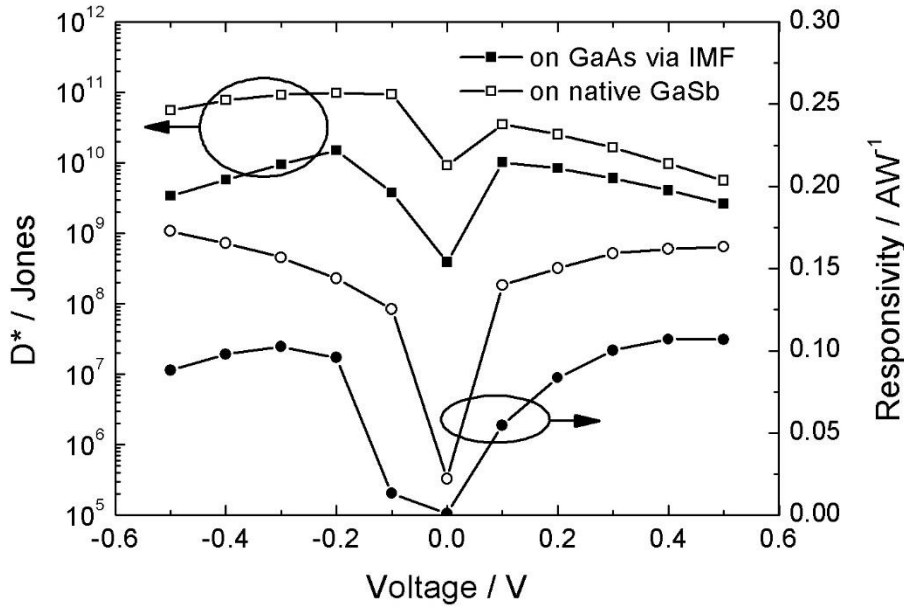


Figure 6.9: Specific detectivity (D^*) and responsivity (R_i) measurement for the two primary *nBn* detector samples, as measured at 200 K using a blackbody source with a 2.33 μm filter.

temperature bandgap (0.39 ± 0.015 eV) in Figure 6.7.

Specific detectivity (D^*) figures were then calculated based upon responsivity measurements taken at 2.33 μm wavelength, for best-case devices. The dark current density and R_dA were taken from the dataset of Figure 6.5. Thermal and shot noise were taken to be the dominant noise sources (which may not strictly be true at lower frequencies). The low-frequency $1/f$ noise contribution will be investigated at the end of this chapter. Figure 6.9 shows both D^* and responsivity (R_i) values for both samples at 200 K. Peak D^* values of 1.5×10^{10} Jones (on GaAs) and 9.8×10^{10} Jones (on GaSb) were recorded. Further inspecting Figure 6.9, it can be seen that R_i peaks at around 0.1 AW^{-1} at -0.3 V bias for the sample grown on GaAs. For the sample grown on native GaSb, R_i continues to increase with bias, even beyond -0.5 V. However, D^* peak values occur for lower bias values of around -0.2 V for the sample grown on GaAs. This is due to reduced dark current levels at lower bias voltages: at 200 K, the dark currents increase from $\sim 2 \times 10^{-5} \text{ Acm}^{-2}$ at -0.1 V to $\sim 2 \times 10^{-4} \text{ Acm}^{-2}$ at -0.3 V.

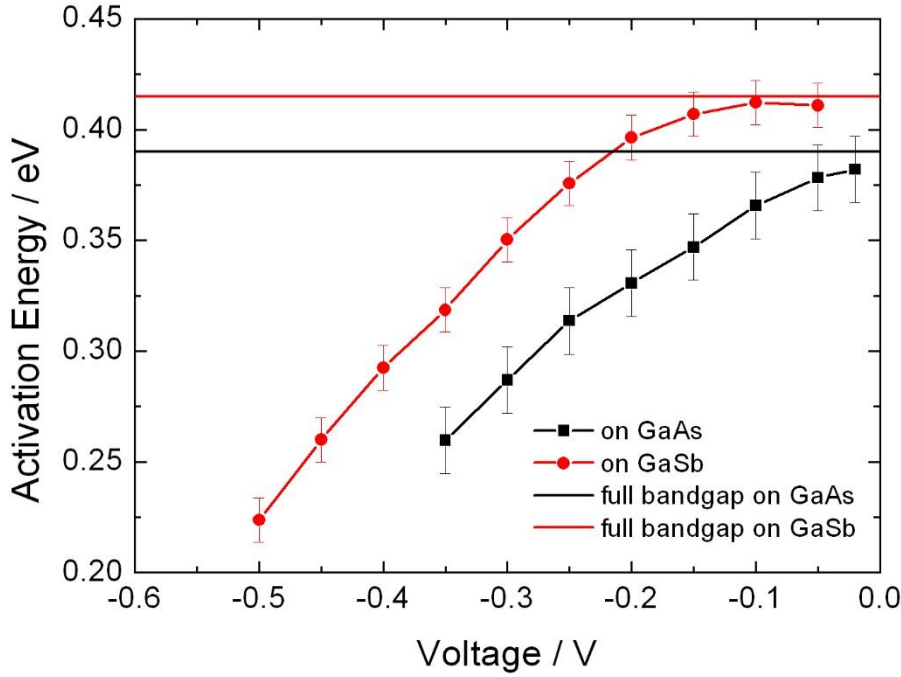


Figure 6.10: Dark current activation energies as a function of bias voltage, for both samples.

These were fitted using data for temperatures between 200 and 300 K.

Figure 6.10 shows dark current activation energies as a function of bias. It can be seen that both samples operate in the diffusion current limited regime for small reverse bias conditions, as indicated by activation energies close to the full bandgap of the absorption layer material. For larger reverse bias conditions, the absorption layer starts to experience depletion, and the activation energy falls, corresponding to the presence of some degree of SRH generation. This helps to explain the fact that the D^* figures are optimal at small reverse bias, in spite of superior responsivities at higher reverse bias.

Temperature dependent dark current density characteristics are shown (for best-case devices) for both samples in Figure 6.11 and Figure 6.12. For the sample grown on GaSb, it can be seen that, after experiencing a steep initial rise as reverse bias is applied, the dark currents are somewhat bias independent at intermediate bias voltages (between -0.1 V and -0.3 V) before

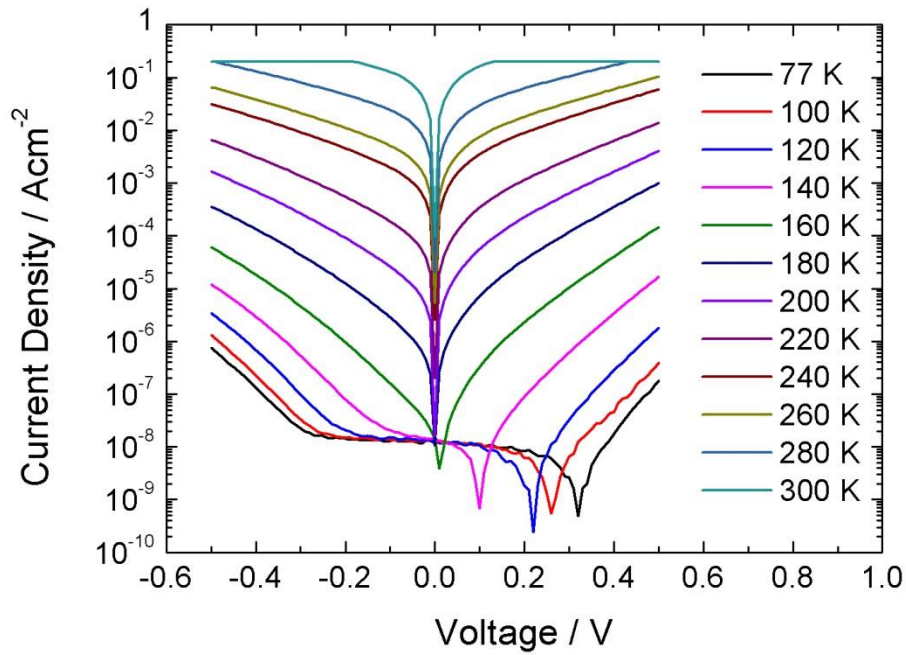


Figure 6.11: Temperature dependent dark currents for the sample grown on GaAs 800 μm diameter mesas were used for the measurement. The data is limited by the noise floor of the Sourcemeter below ~ 140 K.

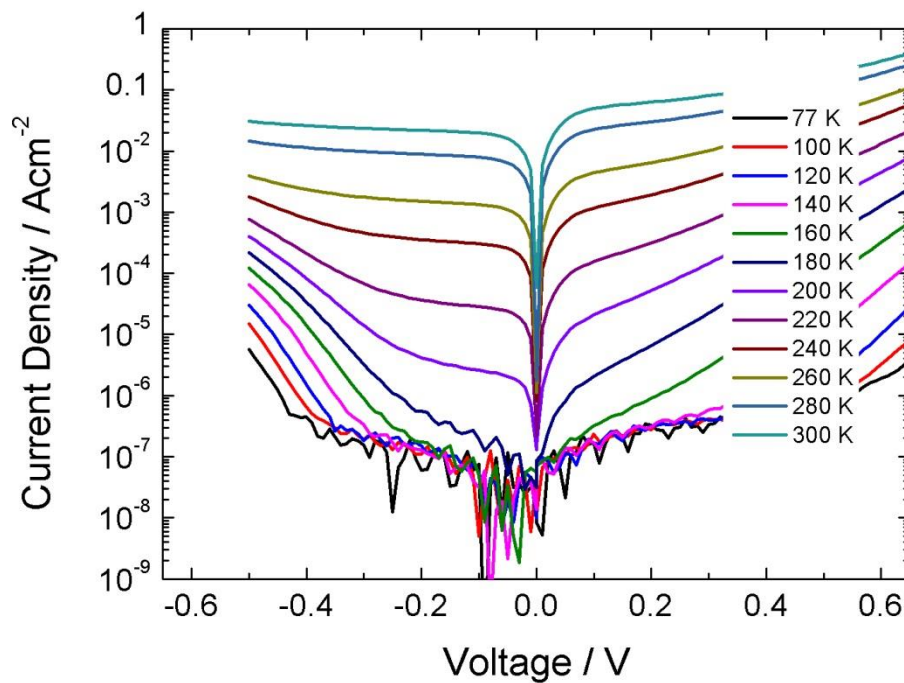


Figure 6.12: Temperature dependent dark currents for the sample grown on GaSb. 800 μm diameter mesas were used for the measurement. The data is limited by the noise floor of the Sourcemeter below ~ 180 K.

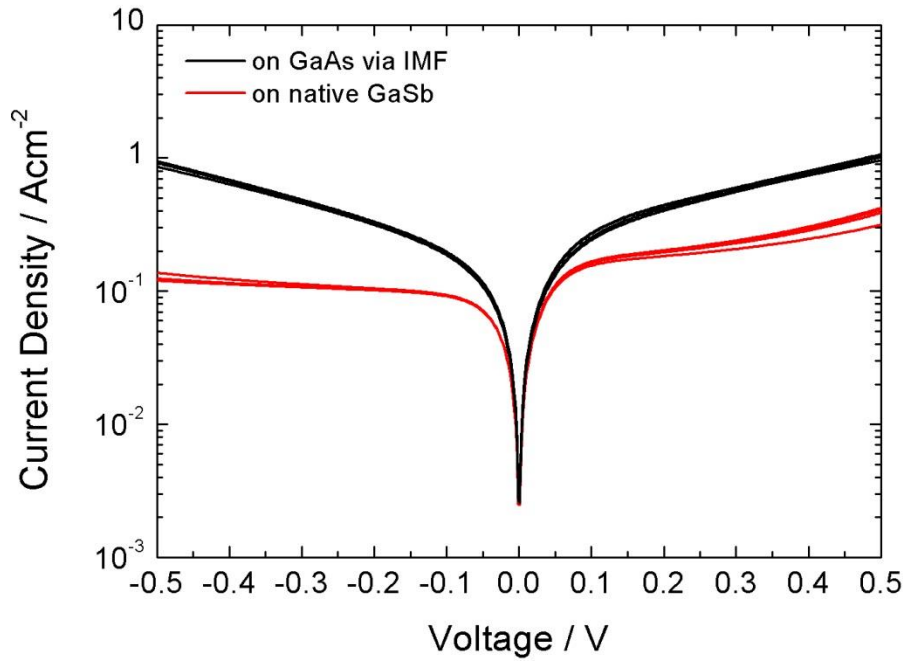


Figure 6.13: Dark current density measurements plotted for mesa diameters mesa between 25 μm and 800 μm for both primary samples, at 300 K.

rising more steeply at larger bias voltages. This intermediate region is characteristic to diffusion limited dark currents: since there is no dependence on the depletion width for the diffusion current, applying additional bias voltage does not result in increased dark currents.⁶ At higher bias voltages, the absorber begins to deplete and the bias dependence returns, corresponding to reduced activation energies exhibited in Figure 6.10 for larger reverse bias. For the sample grown on GaAs, the presence of some residual SRH generation (or trap assisted tunnelling) is indicated by the bias dependence of the dark currents. This can also be seen in Figure 6.10, where the activation energy decreases with additional bias. Nevertheless, the activation energies shown for small operating bias are consistent with diffusion current as the dominant dark current source.

Figure 6.13 illustrates dark current density curves for both samples at 300 K. Data is plotted for six mesa diameters, between 25 μm and 800 μm . It can be seen that the dark currents scale

very closely with the mesa area, indicating bulk leakage currents dominated and surface leakage currents were absent (or at least very small).

*iii) The effects of absorption layer doping upon *nBn* detector performance*

Two further *nBn* detector wafers were grown, on GaAs and on native GaSb, once again, but with reduced absorption layer doping, of $9 \times 10^{16} \text{ cm}^{-3}$. Compositions of $\text{InAs}_{0.90}\text{Sb}_{0.10}$ (on GaAs) and $\text{InAs}_{0.91}\text{Sb}_{0.09}$ (on GaSb) were determined through fitted XRD rocking curves, using the same method as for the two primary samples. Spectral response for these samples is compared with the two primary samples in Figure 6.14. 200 K Cut-off wavelengths of $4.1 \mu\text{m}$ and $4.2 \mu\text{m}$ were determined for the sample grown on GaAs and the sample grown on GaSb, respectively. These values compare closely to those reported elsewhere for $\text{InAs}_{0.91}\text{Sb}_{0.09}$ layers,⁴ providing further evidence that the shortened cut-off wavelengths noted for the primary samples are attributable to band filling. Best-case Arrhenius plots for the two samples are

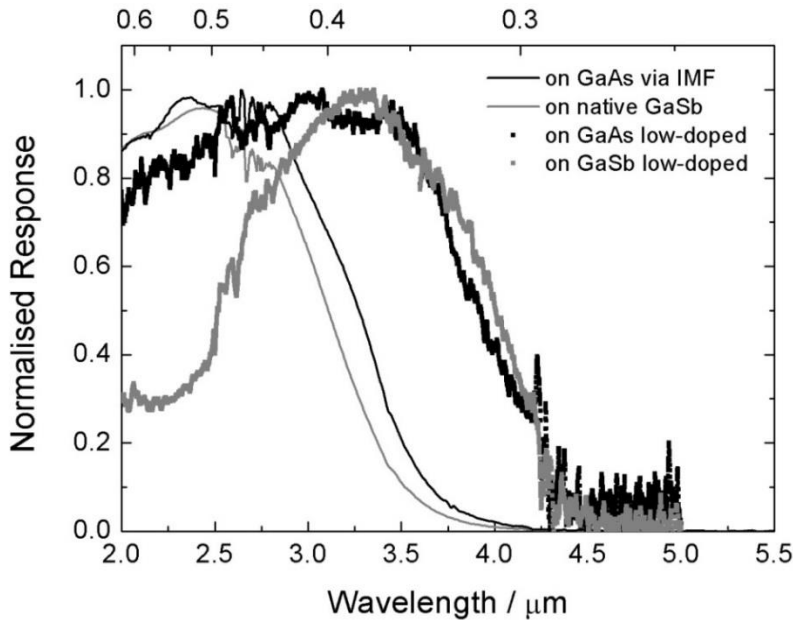


Figure 6.14: Normalised spectral response results for the *nBn* detector samples with low-doped ($9 \times 10^{16} \text{ cm}^{-3}$) absorption layers, and a comparison with data for the primary *nBn* detector samples with heavily doped ($4 \times 10^{17} \text{ cm}^{-3}$) absorption layers. The temperature was 200 K.

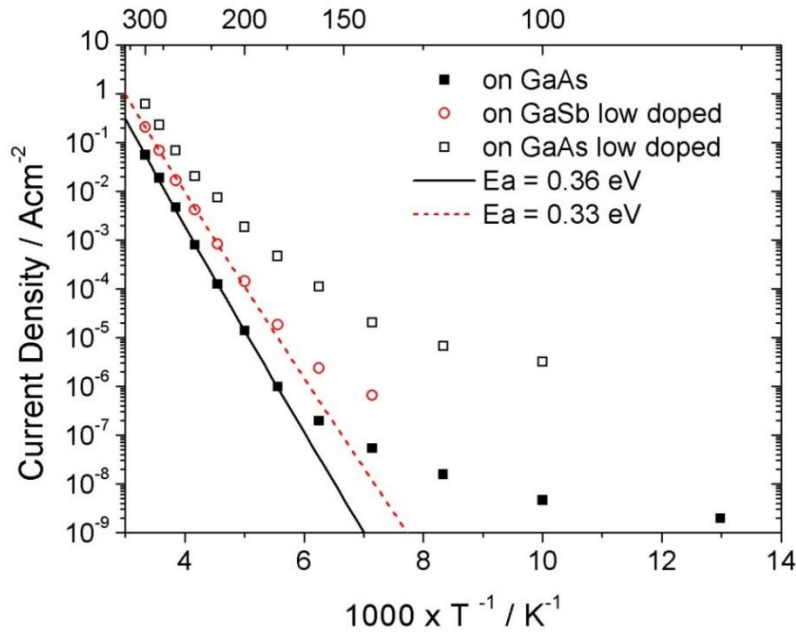


Figure 6.15: Arrhenius plots of the dark current density, as measured with 300 K background radiation excluded, for the two samples with reduced ($9 \times 10^{16} \text{cm}^{-3}$) absorption layer doping. Data is reproduced for the primary sample on GaAs, for comparison.

shown in Figure 6.15. It can be seen that the data for the low-doped sample grown on GaAs does not follow a straight line, i.e. the dark currents do not reduce with temperature as expected for a diffusion limited *nBn* detector. Since the dark current performance was significantly compromised, no activation energy could be extracted. In contrast, the dark current performance of the low-doped sample grown on GaSb exhibits a temperature dependence with an activation energy of the full bandgap (0.33 eV). In this case, the diffusion limited regime was not compromised by the lower absorption layer doping. The slight reduction in the activation energy – when compared to that for the higher-doped primary samples (0.36 – 0.41 eV) – is likely the result of reduced band-filling due to the lower absorption layer doping level.

iv) Longer-wavelength nBn detector sample

In the process of optimising group-V growth conditions for the primary samples, a particularly interesting wafer was grown where the absorption layer had been grown lattice-mismatched with respect to the GaSb buffer layer. The absorption layer composition was determined using XRD fitting to be $\text{InAs}_{0.79}\text{Sb}_{0.21}$, yielding a cut-off wavelength around $5.4 \mu\text{m}$ at 200 K. The sample epilayer structure is shown in Figure 6.16. Arrhenius plots of the best-case dark current densities are shown in Figure 6.17. It can be seen that the activation energy (0.29 eV) again agrees with the full low temperature bandgap of the absorption layer, which found by fitting the spectral response (0.26 eV). However, larger bias was required to obtain a spectral response curve – shown in Figure 6.18 – and it can be seen that the signal is no longer resolved above 160 K due to a weak signal and/or poor signal to noise ratio. This may be attributed to relaxation of the barrier layer, resulting in an additional valence band offset with respect to the absorption layer, impeding the flow of photogenerated carriers. Responsivity was measured using a 1.55

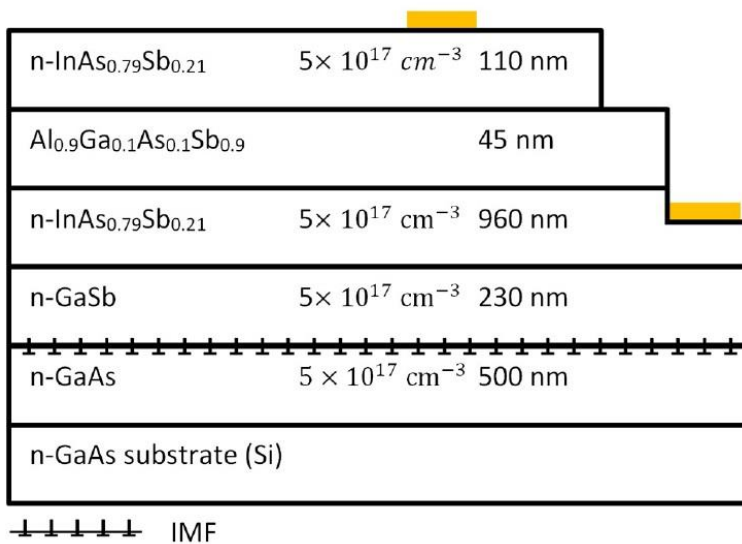


Figure 6.16: Epilayer structure for the longer-wavelength nBn detector structure, showing the mismatched absorption layer composition, as determined using XRD curve fitting.

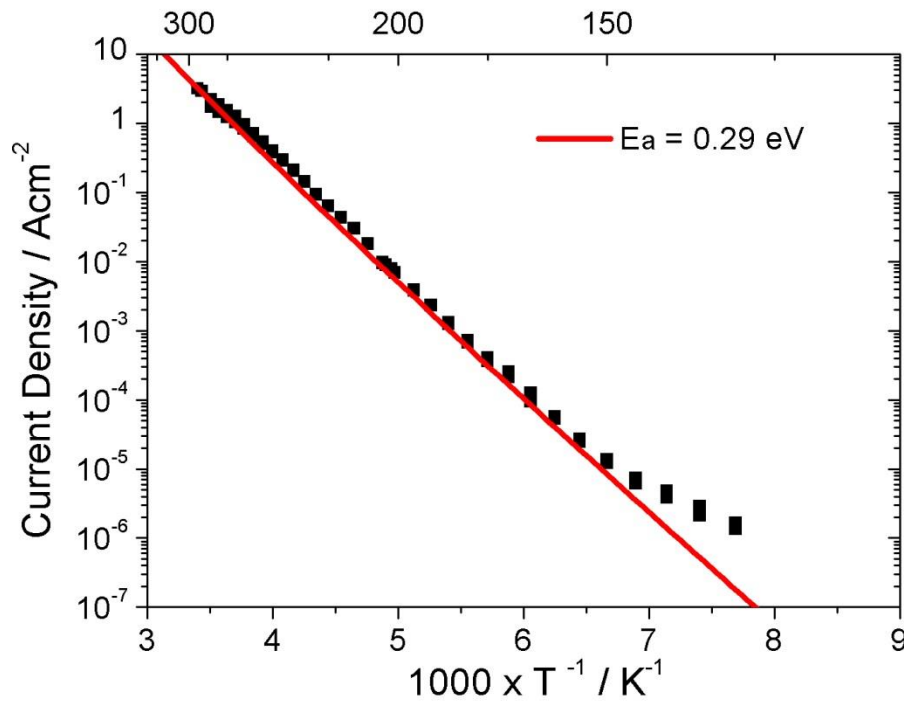


Figure 6.17: Arrhenius plot of the dark current density (at -0.5 V bias) for the longer-wavelength *nBn* sample. An activation energy fitting is also shown.

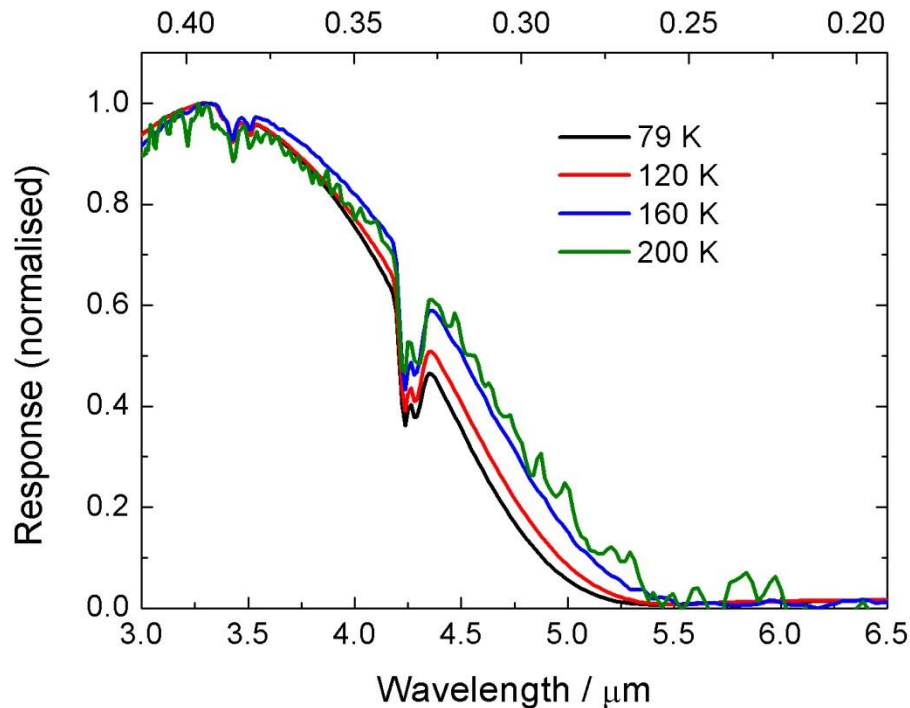


Figure 6.18: Spectral response curves for the longer-wavelength *nBn* sample. It can be seen that the signal becomes weak for the data at 160 K.

μm laser, and found to be 0.15 AW^{-1} at -0.5 V . It was noted in particular that diffusion limited dark currents were still demonstrated, even below 200 K , in spite of the lattice mismatch between the GaSb layer and the InAsSb absorption layer (the Bragg peak separation was more than $1,000 \text{ arcsec}$). This again highlights the suppression of SRH generation by the *nBn* design.

v) 1/f noise characterisation of the primary nBn detector samples

1/f noise is known to be a significant problem when interfacing with read-out integrated circuits for focal plane arrays (FPAs). 1/f noise has been attributed to tunneling through trap states and local modulations of carrier mobility.⁷ Characterisation of the noise behaviour was carried out for both primary samples, with a view to determining their merit for FPA applications. A Stanford Research Systems SR570 preamplifier was employed for the measurements. The use of a “high-bandwidth” mode was necessary to prevent RC roll-off above 10 kHz . Gain was also limited to $1 \mu\text{A/V}$ due to bandwidth considerations.⁸ The instrumentation was first checked by verifying the thermal noise across a 100Ω resistor. Figure 6.19 shows the noise behaviour of the sample grown on GaAs for a bias voltage of -0.2 V at 240 K . The noise knee frequency was determined by the intersection of linear fits for the low frequency and high frequency regimes. Following screening (based on the dark current density) of a number of devices, measurements were taken for three different devices, for which values of $2.9 \text{ kHz} < f_{\text{knee}} < 4.2 \text{ kHz}$. It was verified that noise measured at higher frequencies was due to Shot Noise (rather than a noise floor due to the equipment) by reducing the bias voltage and observing the change in the noise magnitude associated with the change in the dark current. It was found that the minimum signal level distinguishable was $\sim 0.5 \times 10^{-12} \text{ AHz}^{1/2}$ and this was taken to be the noise floor. While the stated noise knee frequencies are significantly greater than that expected for photovoltaic HgCdTe, with values of $10 \text{ Hz} < f_{\text{knee}} < 150 \text{ Hz}$ reported for devices sensitive

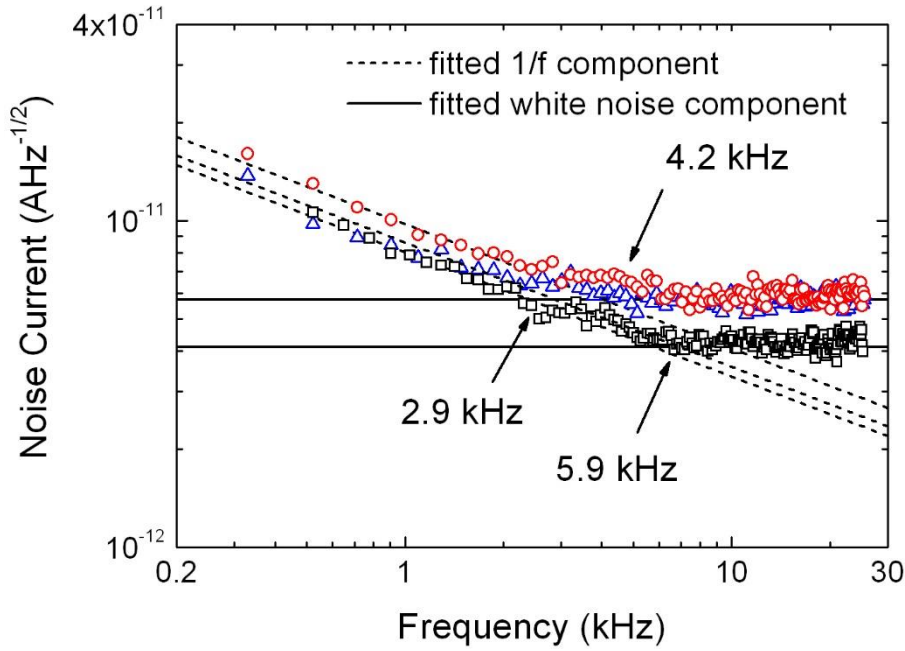


Figure 6.19: Noise behaviour for the primary *nBn* sample grown on GaAs, for 200 μm diameter mesas, again at 240 K.

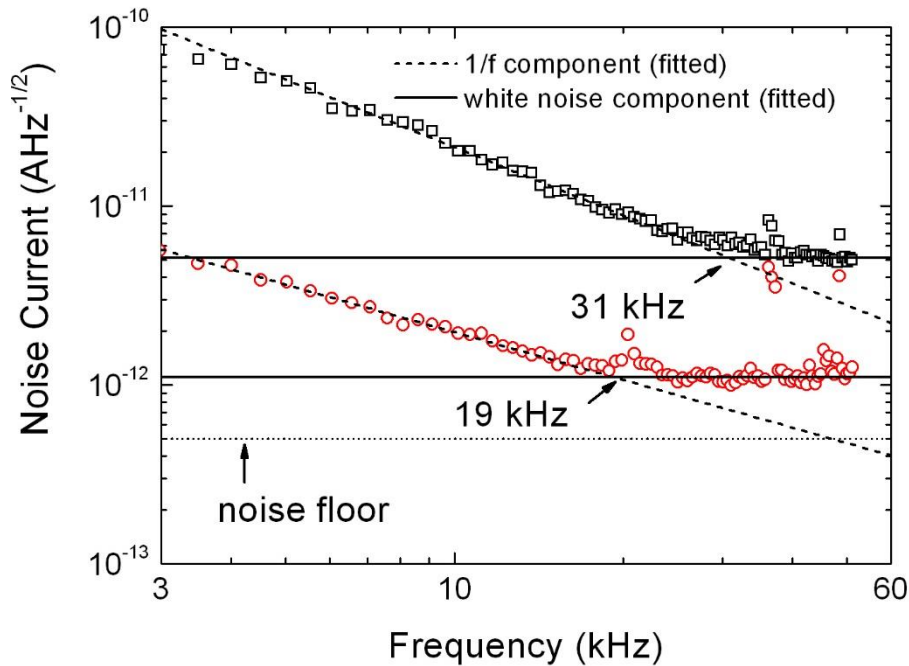


Figure 20: Noise behaviour for the primary *nBn* sample grown on GaSb, for 200 μm diameter mesas, again at 240 K.

between 3.0 – 5.5 μm [9], these values can also be compared with values from the literature for optimised photoconductive HgCdTe. For this case, values of 1 – 2 kHz are typical, e.g. ref [10]. Finally, Figure 6.20 shows the results of an equivalent measurement carried out on the primary sample grown on GaSb. It can be seen that the 1/f noise knee frequencies of the devices measured were larger than those for the sample on GaAs – 19 kHz and 31 kHz, respectively. This was thought to be attributable to the lower absolute magnitude of the Shot noise, due to the lower dark current density, making the 1/f component relatively more significant.

vi) Discussion

nBn detector structures were implemented on both a GaAs substrate, via an IMF array, and on native GaSb. The absorption layers were grown lattice matched to GaSb (6.09 Å), whether via a buffer layer, for growth on GaAs, or directly onto the native GaSb substrate. Pseudomorphic growth of the barrier layers was established via RHEED reconstruction and critical thickness modelling, and a minimal valence band offset calculated, using the model of Krijn.¹ However, one limitation of the work carried out was that the temperature dependence of the band offsets could not be readily calculated, and so it is possible that device responsivity could be further optimised by tuning the barrier layer composition to achieve the zero-offset condition exactly at the 200 K operating temperature (and/or allow for the operating temperature to be raised to 240 K). Further iterations of the devices presented in this chapter could allow for the band offset to be optimised experimentally. Furthermore, it should be possible to grow the barrier layer exactly lattice matched to the $\text{InAs}_{0.91}\text{Sb}_{0.09}$ absorption layer, i.e. $\text{Al}_{0.9}\text{Ga}_{0.1}\text{As}_{0.08}\text{Sb}_{0.92}$, so that relaxation could be ruled out entirely. This was not achieved for the current samples due to time constraints: concurrent optimisation of the two mixed group-V layers is particularly challenging. This is due to the requirement for very low Sb_2 flux for the absorption layer, but very high Sb_2 flux for the barrier layer, necessitating time-consuming changes to the Sb cell temperature. In spite of the slight lattice mismatch that occurred for the barrier layer, RHEED

reconstruction patterns and critical thickness modelling suggested relaxation did not occur. This was further verified through dark current activation energies, which were in agreement with the low-temperature bandgap of the absorption layer, as determined using spectral response. It is well known that additional valence band offsets – which would necessarily result from relaxation of the barrier layer – lead to increased activation energies, i.e. activation energies in excess of the low-temperature bandgap.¹¹ Notably, *n*-type doping of the barrier layer was noted to result in electrical cross-linking between the mesas, in conflict with the analysis of ref [6]; however, it is still possible that such doping needs to be very carefully optimised in order that the barrier layer should remain fully depleted. In processing, the addition of a small Ga mole fraction to the barrier layer was found to suppress oxidation. This should be beneficial to long term reliability, since ternary AlAsSb layers readily oxidise when exposed to air.

At 200 K, D^* figures of $1.5 \times 10^{10} \text{ cmHz}^{1/2}\text{W}^{-1}$ and $9.8 \times 10^{10} \text{ cmHz}^{1/2}\text{W}^{-1}$ were calculated, for growths on GaAs and GaSb, respectively. These compare favourably with figures reported for type-II InAs/GaSb superlattice *nBn* structures. In particular, refs [10] and [11] report that values around $10^{11} \text{ cmHz}^{1/2}\text{W}^{-1}$ were measured at 77 K. This value roughly compares with that of the primary *nBn* structure grown on GaSb for a temperature of 200 K, although it should be noted that the superlattice structures in refs [10] and [11] operate at longer wavelengths – 4.3 μm and 5.2 μm , respectively – so that higher dark currents are expected for devices in the reference. Values for responsivity (of around 0.1 – 0.15 AW^{-1}) were weaker than those reported for InAsSb *nBn* detectors in Section (3) [Klipstein]. This could be due to the high doping in the absorption layer, which has the effect of reducing the hole diffusion length, and/or the band alignment, as commented above. It is a limitation of the current work that the two effects cannot be separated. This limitation could be overcome by further experimental investigation, though measurements of minority carrier hole diffusion lengths using an area dependent analysis of the dark currents. It should be pointed out that heavy doping

also reduces the dark currents, both due to the inhibition of depletion in the absorption layer and due to pinning of the Fermi level at the conduction band edge, away from mid-gap SRH centres. A trade-off is therefore required, particularly for *nBn* structures grown on GaAs (which are susceptible to dark currents associated with threading dislocations). In spite of the weak responsivity, the above noted 200 K D^* figures compare favourably with those from the literature for the same temperature: in particular Soibel et. al. [5] reported figures of around $5 \times 10^{10} \text{ cmHz}^{1/2}\text{W}^{-1}$ for InAsSb devices grown on native GaSb substrates. Results were presented for the primary samples for a temperature of 200 K, which is roughly equivalent to the minimum temperature which can be obtained using a 3-stage thermoelectric cooler.¹² It would be preferable to operate at 240 K (due to reduced power requirements). Soibel et. al. [5] reported InAsSb *nBn* detectors on GaSb with D^* values of $5 \times 10^9 \text{ cmHz}^{1/2}\text{W}^{-1}$ at 250 K. In comparison, results for the primary *nBn* sample grown on GaSb peaked at around $10^{10} \text{ cmHz}^{1/2}\text{W}^{-1}$ at 240 K. However, for the sample grown on GaAs this figure drops to around $5 \times 10^8 \text{ cmHz}^{1/2}\text{W}^{-1}$ at 240 K, largely owing to reduced responsivity (0.02 AW^{-1}) at this temperature – a key limitation to be addressed in future work.

Two further *nBn* samples were grown with a lower absorption layer doping density of $9 \times 10^{16} \text{ cm}^{-3}$. For the sample grown on GaAs, the dark currents were no longer diffusion limited. This may be attributed to the large number of SRH centres in IMF-array-based material, which then influence the dark currents if the absorption material depletes – even a little. Cut off wavelengths were also lengthened for both low-doped samples, due to reduced band filling effects.

A longer-wavelength *nBn* sample was also demonstrated, exhibiting diffusion-limited dark current behaviour in spite of a lattice-mismatched absorption layer. However, responsivity was weak, likely owing to relaxation of the barrier layer, resulting in a valence band offset between the two layers. Nevertheless, careful optimisation of the barrier layer composition, so that it is

exactly lattice matched to the absorption layer, would likely yield improved performance. It is noteworthy that SRH recombination was still suppressed by the *nBn* design in spite of the significant lattice mismatch between the absorption and GaSb buffer layers (which is necessarily relieved through threading dislocations).

Substrate Material	Dark Current Density (Acm^{-2})	Specific Detectivity ($\text{cmHz}^{1/2}\text{W}^{-1}$)	Cut-off wavelength (μm)
GaAs (IMF)	1.6×10^{-5}	1.5×10^{10}	3.5
GaSb (lattice matched)	3.0×10^{-6}	9.8×10^{10}	3.3

Table 6.1: Shows a summary of key figures of merit determined in this section for *nBn* detectors grown on GaAs (via IMF) and native GaSb substrates. All the tabulated data was measured at 200 K.

References

- [1] M. P. C. M. Krijn, *Semicond. Sci. Technol.* 6, 27 (1991).
- [2] I. Vurgaftman, J. R. Meyer, and L. R. Ram-Mohan, *J. Appl. Phys.*, Vol. 89, 11 (2001).
- [3] W. E. Tennant, D. Lee, M. Zandian, E. Piquette and M. Carmody, *J. Electron. Mater.* 37, 9 (2008).
- [4] A. Soibel, C. J. Hill, S. A. Keo, L. Hoglund, R. Rosenberg, R. Kowalczyk, A. Khoshakhlagh, A. Fisher, D. Z.-Y. Ting, and S. D. Gunapala, *Appl. Phys. Lett.* 105 023512 (2014).
- [5] P. K. Basu, “Theory of Optical Processes in Semiconductors”, Oxford University Press (2007).
- [6] P. Klipstein, in *Proc. SPIE 6940, Infrared Technology and Applications XXXIV*, 69402U (2008).
- [7] F. N. Hooge, *IEEE Trans. Electron Dev.* 41, 11 (1994).
- [8] Stanford Research System SR570 Low Noise Current Preamplifier (user manual) rev 1.6.
- [9] M. S. Nikitine, G. V. Chekanova, *Proc. SPIE*, 17 454 (2013).
- [10] R. Sewell, C.A. Musca, J.M. Dell, L. Faraone, K. Jozwikowski and A. Rogalski, *J. Electron. Mater.* 32, 7 (2003).
- [11] J. R. Pedrazzani, *Characteristics of InAs-Based nBn Photodetectors Grown by Molecular Beam Epitaxy*, (thesis) (2010).
- [12] Thor Labs, TED200C Thermoelectric Temperature Controller Manual, <http://www.thorlabs.de/thorcat/15900/TED200C-Manual.pdf> (2014).

(7) Results and Discussion III – Extended wavelength avalanche photodiodes

In the previous chapter, the IMF growth mode was exploited to allow for the growth on nBn detectors on GaAs substrates. Continuing the theme of lattice-mismatched epitaxy, the present chapter presents two novel SAM-APD structures, each with an IMF interface inserted into the electrically active region of the device. Through this, GaSb absorption regions were combined directly with GaAs and Al_{0.8}Ga_{0.2}As multiplication regions to create hitherto-imp-ossible device structures. While the GaSb absorption regions offer detection up to 1.7 μm, the design could easily be extended to longer wavelengths using other absorption materials (or indeed SLS layers) which are lattice matched to GaSb.

i) Growth of extended wavelength avalanche photodiodes

Two separate-absorption-and-multiplication (SAM) APD wafers were grown, and processed once, by workers at UCLA in California. These are illustrated in Figure 7.1. IMF arrays were used to directly combine GaAs and Al_{0.8}Ga_{0.2}As multiplication layers with GaSb absorption material. The *GaAs design* represents the simplest case and a proof-of-principle. This was developed in the *AlGaAs design* to allow for lower excess noise, a thinner structure and a further suppression of the dark currents. In both designs, the narrow-bandgap GaSb absorption region allows for sensitivity at wavelengths up to 1.7 μm. Growth was carried out using a Veeco Gen 930 MBE reactor. For both wafers, oxide desorption from the GaAs substrate was performed first, at 600 °C. The substrate temperature was subsequently reduced to 580 °C for the growth of the n⁺-GaAs cladding regions. For the *GaAs design*, a p⁻ multiplication was grown next. In the *AlGaAs design* this was replaced with a short, unintentionally doped Al_{0.8}Ga_{0.2}As multiplication region and a p⁺ charge sheet. The function of the charge sheet is to confine the electric field to the multiplication region. For the GaAs design, the fields

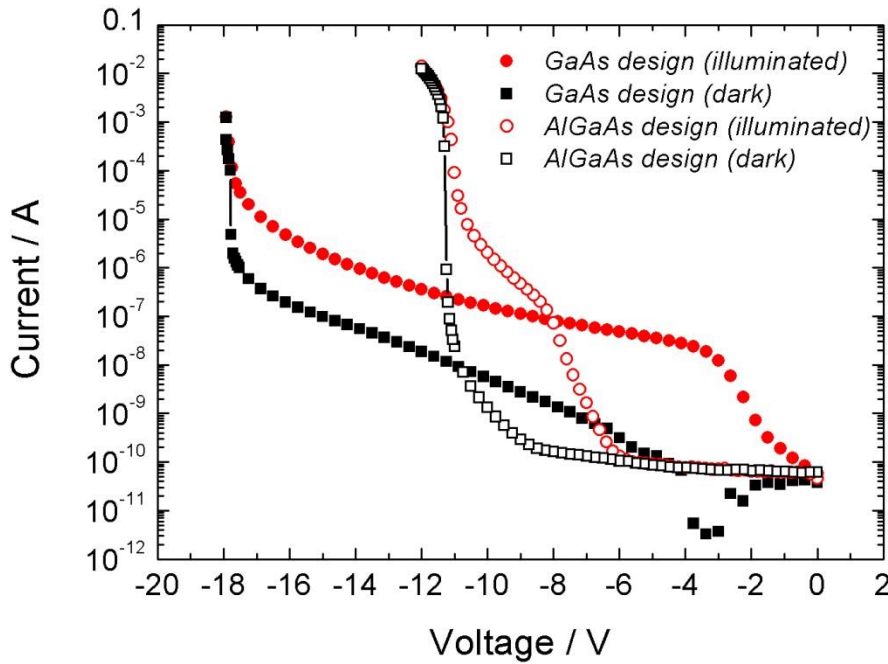


Figure 7.2: IV curves, for 200 μm diameter mesas, for both the *GaAs design* and the *AlGaAs design*. The solid lines are guides to the eye.

power of 14 mW. It can be seen that lower dark currents and a higher photocurrent to dark current ratio were exhibited by the *AlGaAs design* sample, as expected given the wider bandgap of the *p-n* junction material (2.09 eV for $\text{Al}_{0.8}\text{Ga}_{0.2}\text{As}$ compared with 1.4 eV for GaAs). The dark currents recorded below the respective breakdown voltages were noted to be greatly reduced compared with those expected for GaSb *p-i-n* diodes: at 90% of breakdown voltage measured dark current densities of $5.7 \times 10^{-4} \text{ Acm}^{-2}$ and $5.1 \times 10^{-6} \text{ Acm}^{-2}$ were recorded, for the *GaAs design* and *AlGaAs design*, respectively. (This can be compared with data from ref [2], which reports $7 \times 10^{-3} \text{ Acm}^{-2}$ at -1.0 V for a homojunction GaSb *p-i-n*.) Since electric field is excluded from the absorption layers, the transport of photogenerated electrons takes place by diffusion across the IMF heterojunctions. Spectral response for the two samples is shown in Figure 7.3. Cut-off wavelengths were obtained by plotting the square of the photoresponse against energy and extrapolating the low-energy region to zero, using a linear fit. Figures of 1.70 μm and 1.75 μm were found, for the *GaAs design* and the *AlGaAs design*,

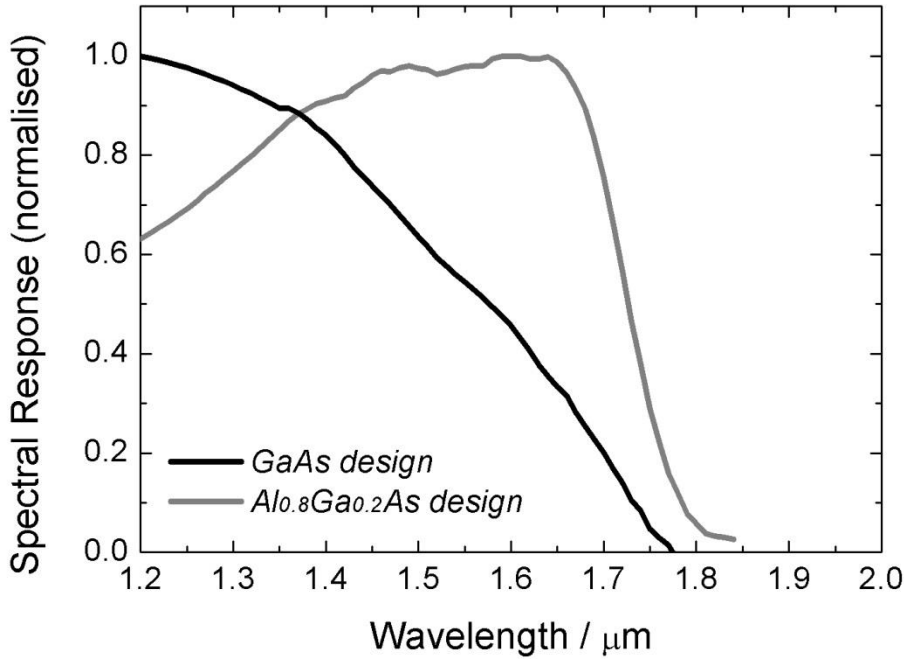


Figure 7.3: Normalised spectral response curves for both designs. The cut-off wavelength is slightly lengthened for the AlGaAs design, owing to a thicker absorption region.

respectively. The marginally longer cut-off wavelength of the latter was attributed to the increased thickness of the absorption layer, which results in a higher absorption probability for longer-wavelength photons. The increased absorbance exhibited at intermediate wavelengths was also attributed to this effect.

Fitted capacitance-voltage (CV) profiles for both structures are shown in Figure 7.4. These were modelled with the electrostatic model of Section (4), using the layer thicknesses and doping densities given in Figure 7.1. Through optimisation, close agreement between the measured and modelled curves was achieved. Accurate knowledge of the device layer structures was therefore confirmed. In particular, the plateau between -2.0 V and -14.0 V for the GaAs design indicates the pinning of the depletion edge by the charge sheet associated with the IMF array. For the AlGaAs design, the depletion edge is pinned by the IMF array between approximately -6.0 V and -7.0 V. Beyond -7.0 V, the CV data terminates owing to

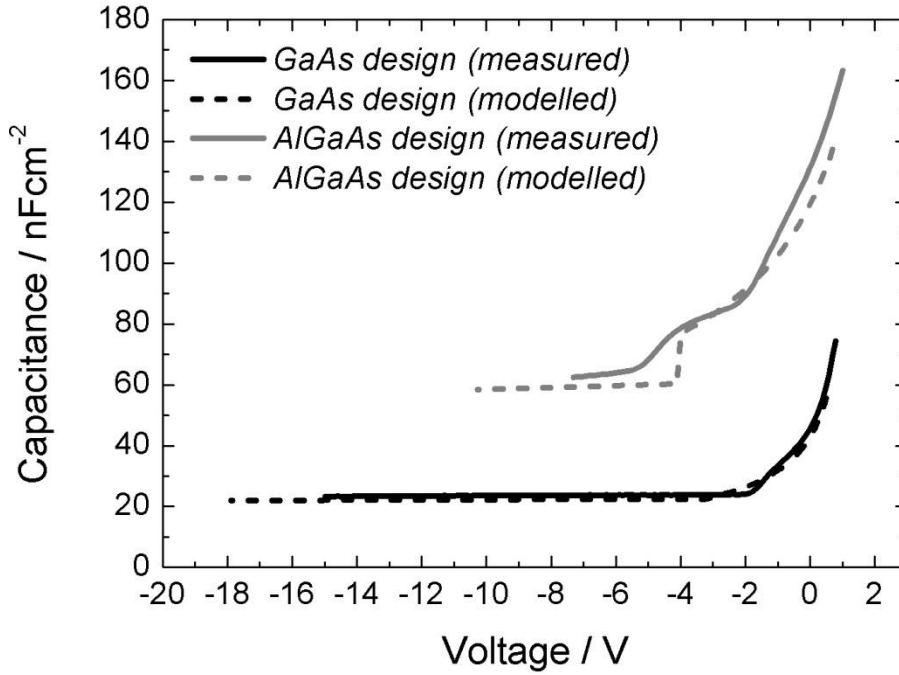


Figure 7.4: Capacitance-voltage (CV) profiles for both designs, together with fitted curves generated using the modelling detailed in Section (4).

interference from the avalanche multiplication process. The fitted curve for the *GaAs design* can be seen to agree almost exactly with the experimental data. However, for the *AlGaAs design* there are additional features between -2.0 V and -5.0 V. These are likely due to the redistribution of charges forced by the band offsets around the AlGaAs/GaAs interface. Though these features are not taken into account by the electrostatic model, the multiplication and excess noise behaviours were still in good agreement with the measured data, as detailed in the following sections (the AlGaAs/GaAs interface is fully depleted at operational bias).

iii) Determination of multiplication

It is customary, e.g. ref [3], to determine multiplication, M , as a function of voltage by first extrapolating the primary photocurrent, I_{pr} , from low bias before dividing the measured photocurrent, I_{meas} , by the extrapolated value, i.e. $M = I_{meas}/I_{pr}$. This method assumes the primary photocurrent is proportional to the applied voltage via the dependence on the depletion

width. However, for the devices presented in this chapter the field is excluded from the absorption material – as noted above – so that the bias dependence exists due to the lowering of potential barriers at the device’s heterointerfaces (rather than due to the dependence on the width of the depletion region). Photogenerated electrons can then travel from the absorption regions to the GaAs or AlGaAs multiplication region. This is visualised in Figure 7.5 and Figure 7.6, which show sections of the band diagrams close to the interface between the absorption and multiplication regions at 90% of breakdown voltage, as generated using Simwindows software. The IMF array has been represented by a p -type sheet of charge with density $3 \times 10^{12} \text{cm}^{-2}$.¹ It can be seen that potential barriers are still present adjacent to the absorption region, even under operating voltage. The barrier is slightly smaller in the *GaAs design* – 140 meV compared with 170 meV – however the accuracy of the bandstructure model is probably not good enough to make a comparison. Both devices will have photocurrent depending exponentially on bias, since emission over the barrier is exponentially dependent

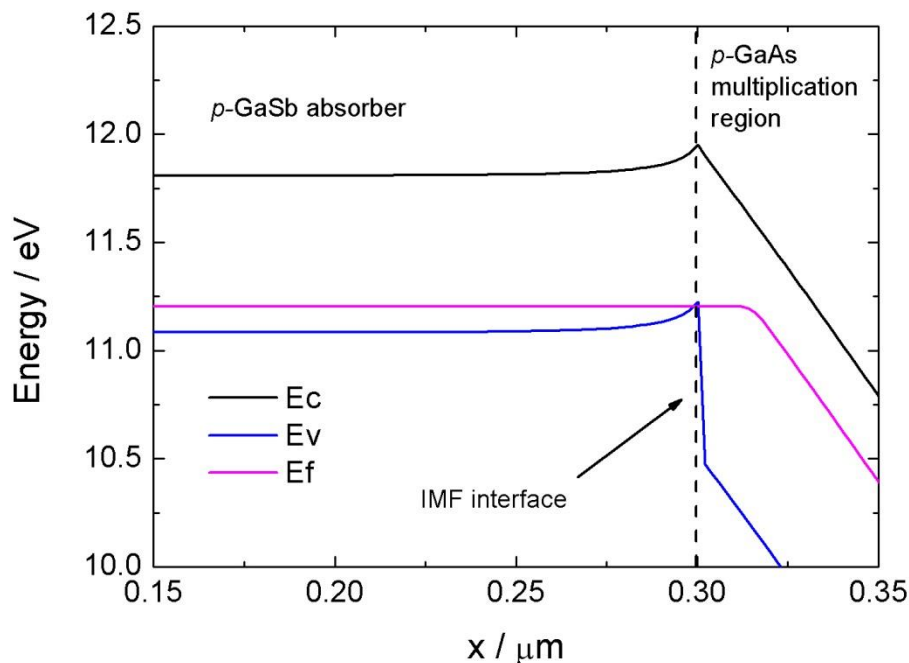


Figure 7.5: Approximate band diagram for the *GaAs design* at 90% of breakdown voltage (-16.0 V). A potential barrier is visible in the conduction band at $x = 0.3 \mu\text{m}$.

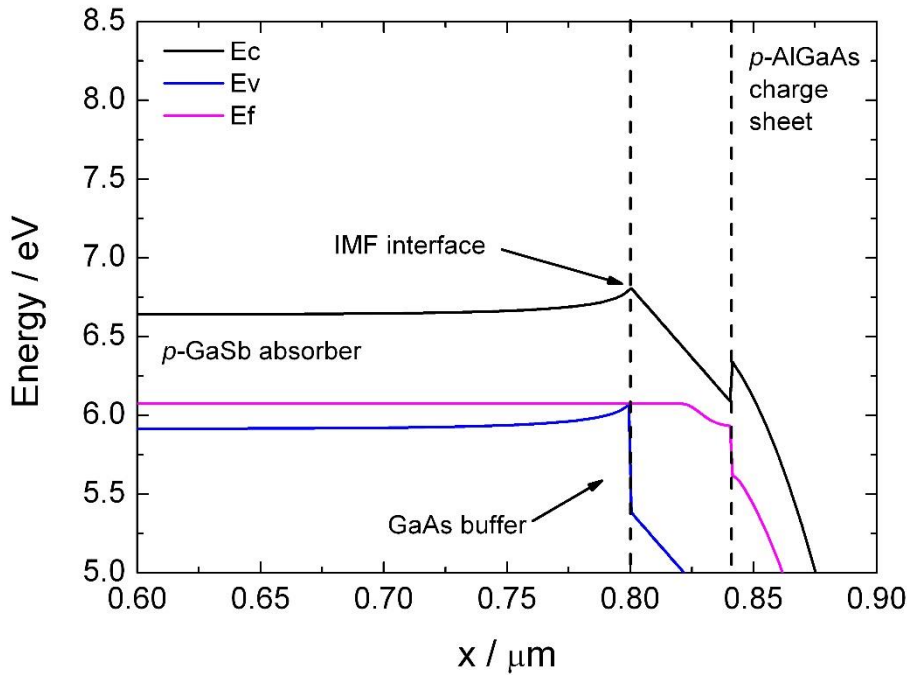


Figure 7.6: Approximate band diagram for the *AlGaAs* design at 90% of breakdown voltage (-10.1V). A potential barrier is visible at $x = 0.95 \mu\text{m}$ in the conduction band.

on the barrier height, and since there is no change in the depletion width (since the IMF array pins the depletion). However, inspecting Figure 7.7, it was still not possible to conventionally extrapolate the primary photocurrent from the low voltage ($M \approx 1$) region for the *AlGaAs* design sample due to irregular dependence on the applied voltage, i.e. the shape of the photocurrent curve between -7.0 V and -9.0 V. This likely results from the movement of the depletion front across the GaAs buffer layer. A similar effect was present in the *GaAs* design sample. Therefore, another method was needed to determine the multiplication. It was decided that the primary photocurrents could be determined from the measured photocurrents through the use of modelled multiplication profiles. These were calculated using electric field profiles from the CV model of Section (4) with the aid of the measured CV profiles (Figure 7.4). Parameterised ionisation coefficients for GaAs and $\text{Al}_{0.8}\text{Ga}_{0.2}\text{As}$ were obtained from refs

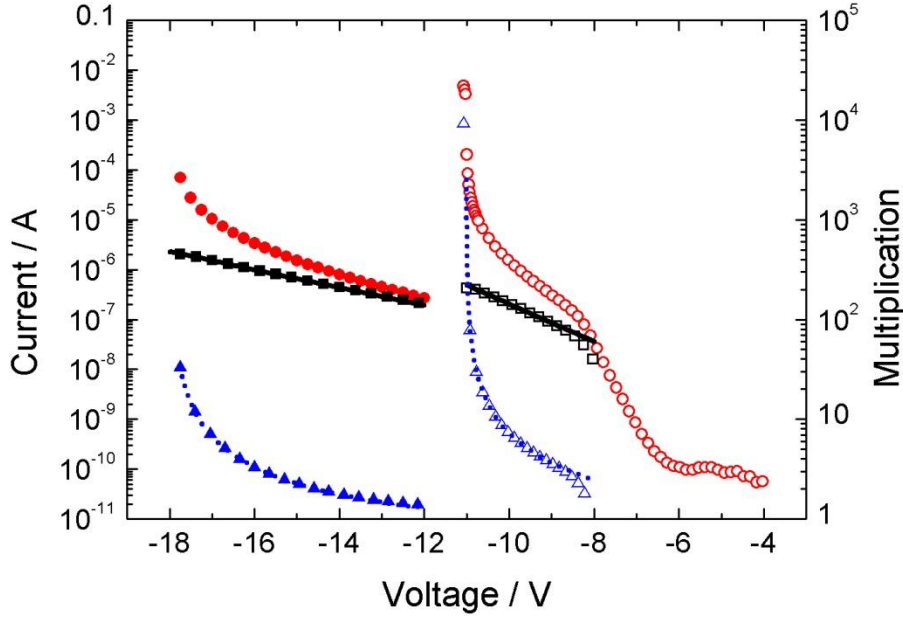


Figure 7.7: Illustrates fitting of the multiplication for 200 μm diameter mesas. Measured photocurrent: (●) *GaAs design*, (○) *AlGaAs design*. Modelled multiplication: dotted lines. Calculated primary photocurrent: (■) *GaAs design*, (□) *AlGaAs Design*. Fitting of primary photocurrent: solid lines. Calculated multiplication: (▲) *GaAs design*, (△) *AlGaAs design*.

For GaAs the coefficients used were:

$$\alpha(\xi) = 1.89 \times 10^5 \exp \left\{ - \left(\frac{5.75 \times 10^5}{\xi} \right)^{1.82} \right\} \quad \xi \leq 5 \times 10^5 \text{ Vcm}^{-1}$$

$$\beta(\xi) = 2.21 \times 10^5 \exp \left\{ - \left(\frac{6.57 \times 10^5}{\xi} \right)^{1.75} \right\} \quad \xi \leq 5 \times 10^5 \text{ Vcm}^{-1}$$

$$\alpha(\xi) = \beta(\xi) = 2.3 \times 10^6 \exp \left\{ - \left(\frac{4.08 \times 10^6}{\xi} \right)^{0.634} \right\} \quad \xi \geq 5 \times 10^5 \text{ Vcm}^{-1} \quad (1)$$

For $\text{Al}_{0.8}\text{Ga}_{0.2}\text{As}$, the coefficients used were:

$$\alpha(\xi) = 3.18 \times 10^5 \exp \left\{ - \left(\frac{1.04 \times 10^6}{\xi} \right)^{1.67} \right\} \quad \xi \leq 3.28 \times 10^5 \text{ Vcm}^{-1}$$

$$\beta(\xi) = 3.55 \times 10^5 \exp \left\{ - \left(\frac{1.12 \times 10^6}{\xi} \right)^{1.85} \right\} \quad \xi \leq 3.28 \times 10^5 \text{ Vcm}^{-1}$$

$$\alpha(\xi) = \beta(\xi) = 3.84 \times 10^6 \exp \left\{ - \left(\frac{1.02 \times 10^7}{\xi} \right)^{0.55} \right\} \quad \xi \geq 3.28 \times 10^5 \text{ Vcm}^{-1} \quad (2)$$

[4] and [5] – as reproduced above, where all fields are given in Vcm^{-1} and the ionisation coefficients have units of cm^{-1} . Multiplication profiles were then calculated using standard local model integrals given in Section (3). Through optimisation of the fitted structure – specifically, small changes in the modelled multiplication region width – the primary photocurrent was found to be well fitted by a simple exponential function in each case, albeit with the region immediately before breakdown differing slightly (due to small differences between the modelled and experimentally observed breakdown voltages). These exponential functions were then extrapolated to large reverse bias. Finally, experimental values for multiplication were determined by dividing the measured photocurrent by the fitted exponentials.

iv) Excess noise measurement

Excess noise behaviour was measured next. The excess noise factor is determined as a function of voltage by first subtracting the dark noise power, $P_{\text{dark}}(V)$ from the illuminated noise power $P_{\text{ill}}(V)$ – in units of Watts – to obtain the corrected noise power, $P_{\text{corr}}(V)$. Once $P_{\text{corr}}(V)$ is known for each voltage point, the excess noise factor, $F(V)$, can be calculated according to

$$F(V) = \frac{P_{\text{corr}}(V)}{50qI(V)M(V)} \quad (1)$$

where the factor of 50 accounts for the input impedance of the noise figure meter, q is the elementary charge, $I(V)$ is the current under illumination and $M(V)$ is the multiplication, as determined using the approach detailed above. It is then usual for the electrical coupling of the device with the noise figure meter to be determined and corrected for by comparison of the

noise measured at low gain with the expected shot noise. A further difficulty arose for the present samples in that the quantum efficiencies at small reverse bias were too low for the shot noise resulting from the photocurrent to be measured. Therefore, P_{corr} , and hence $F(V)$, were known only down to a constant factor. In order to correct for the coupling factor, C , a fitting procedure was used to normalise measured excess noise results, F_{meas} , to the form of McIntyre [6], as given in Section (2), i.e.

$$C \cdot F_{\text{meas}} = k_{\text{eff}}M + (1 - k_{\text{eff}}) \left(2 - \frac{1}{M} \right) \quad (2)$$

so that C could be recovered from the experimental data. Whilst not preferred when a shot-noise-calibrated measurement is available, this fitting technique was found to produce accurate results, which were cross-checked using measurements on $\text{Al}_{0.48}\text{In}_{0.52}\text{As}$ *p-i-n* diodes. In performing the fitting, the high multiplication region was treated, where there is a linear dependence of the excess noise factor on the multiplication (and dead-space effects are less important). The fitting then depends on the fact that McIntyre's curves necessarily intersect $F = M = 1$. Figure 7.8 shows excess noise figures for the $\text{Al}_{0.48}\text{In}_{0.52}\text{As}$ *p-i-n* diodes, with the coupling determined using both the shot noise measurement and by using the fitting procedure detailed. It can be seen that there is good agreement between the two curves. Agreement was further verified through measurements for a range of device areas and for several measurement frequencies, with results varying by no more than 15%, and usually less than 5%. The procedure was finally checked by generating a series of lines using Equation 2, multiplying the F -values by a random number and then fitting to recover k_{eff} . In each case the original value of k_{eff} was recovered exactly. Excess noise plots were then made using the multiplication and excess noise factor data gathered.

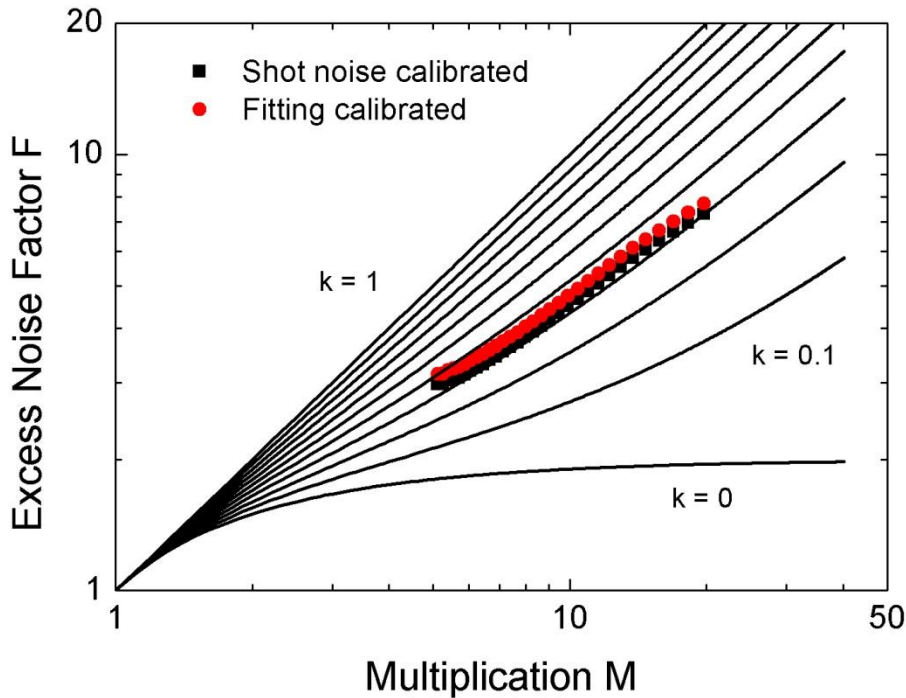


Figure 7.8: Comparison of excess noise results obtained using a shot noise calibrated coupling factor and a fitted coupling factor. The solid lines represent k_{eff} , as given by McIntyre's formula, from $k=0$ to $k=1$ in steps of 0.1.

v) Excess Noise Results

Figure 7.9 and Figure 7.10 show excess noise characteristics for the *GaAs design* and the *AlGaAs design*, respectively. In each case, results were taken from a number of typical devices following screening of a large number of devices. Inspecting Figure 7.9, it can be seen that the data lies in the range $0.2 < k_{\text{eff}} < 0.4$. Previously reported results for thin GaAs *p-i-n* diodes are also shown [Li].⁶ The lower values of k_{eff} in our devices may be explained by the high doping level in the intrinsic region – which was $2.5 \times 10^{16} \text{cm}^{-3}$, as compared with 10^{15}cm^{-3} for the samples in ref [7]. This results in an electric field profile concentrated close to the *p-n* junction, and therefore a decrease in the length over which ionisation events are concentrated. The level of disorder and hence k_{eff} are therefore also reduced. This is visualised in Figure 7.11, which shows the electric field profile at 90% of breakdown,

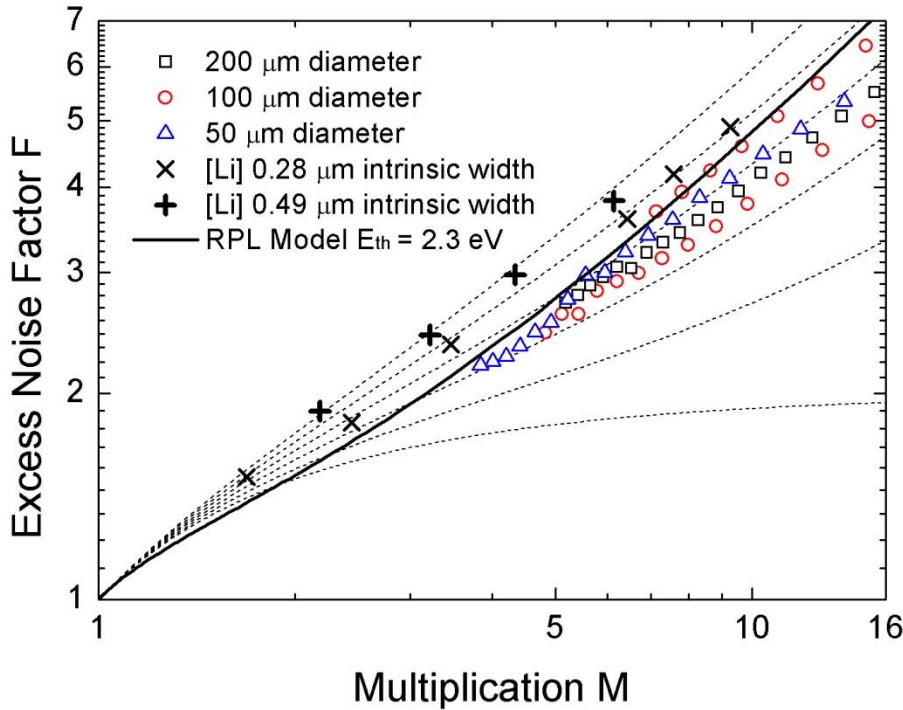


Figure 7.9: Measured and modelled excess noise characteristics for the *GaAs design* sample.

The dotted lines are McIntyre’s curves (Equation 2) from $k = 0$ to $k = 0.5$ in steps of 0.1.

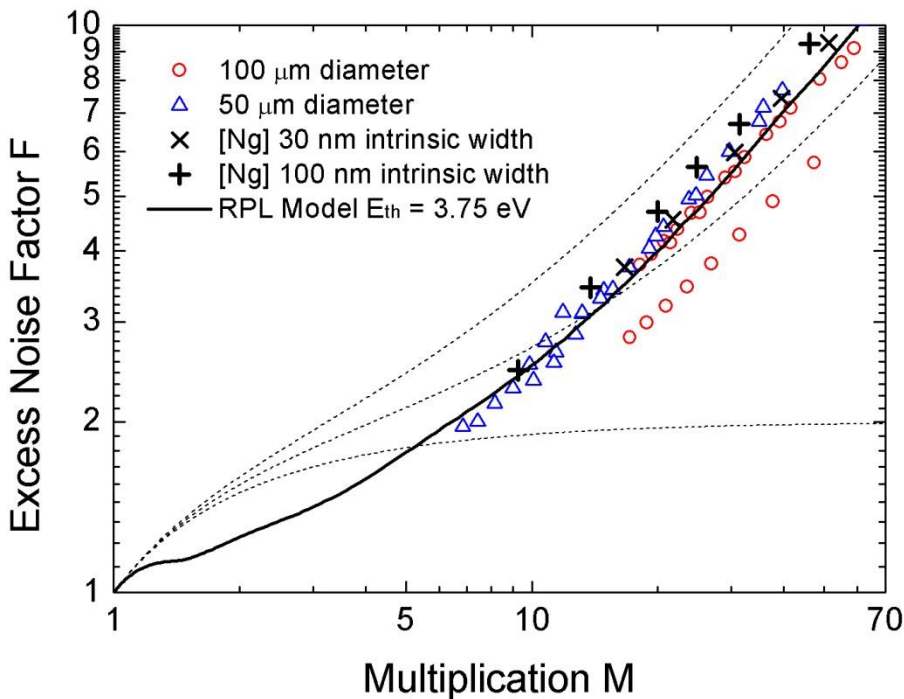


Figure 7.10: Measured and modelled excess noise characteristics for the *AlGaAs design* sam-

ple. The dotted lines are McIntyre’s curves (Equation 2) from $k = 0$ to $k = 0.2$ in steps of 0.1.

together with the associated ionisation coefficients. For the data from the reference, the excess noise behaviour is reduced for the devices with 0.28 μm intrinsic width compared with the data for devices with 0.49 μm intrinsic width due to dead space effects. The curve for the RPL model, which takes the electric field profile and the dead space into account, can be seen to be in close agreement with the experimental data. Figure 7.10 shows excess noise results for the *AlGaAs design*. Excess noise is reduced by the choice of an $\text{Al}_{0.8}\text{Ga}_{0.2}\text{As}$ multiplication region, with the data contained in the range $0.1 < k_{\text{eff}} < 0.2$, except for one outlier. The effects of the significant fraction of dead space in the narrow structure are clearly visible in the region $M < 20$ – i.e. reduced excess noise compared with the local model case. This is reflected in the RPL model curve, for which ionisation threshold energies of 3.75 eV were used (for both electrons and holes). This time, close agreement was found with data from the literature [8] which was also contained in the range $0.1 < k_{\text{eff}} < 0.2$ for devices with intrinsic widths of 30 nm and 100 nm. The intrinsic width of the *AlGaAs design* sample is just 50 nm, however the 65 nm *p*-type charge sheet is also depleted so that the high-field region is wider than the intrinsic layer. This is shown in Figure 7.12. It is further visible that field in the 40nm GaAs buffer layer is reduced to a value of around $3 \times 10^5 \text{ Vcm}^{-1}$ by the AlGaAs charge sheet. Since the ionisation coefficients for GaAs for this field strength are approximately $\alpha = 9000 \text{ cm}^{-1}$ and $\beta = 5000 \text{ cm}^{-1}$ – once again from ref [4] – the mean ionisation paths are greater than 1 μm for both electrons and holes. As a result, ionisation effects in the GaAs buffer were considered to be insignificant. This is supported by the excess noise data which, as noted, closely corresponds to the excess noise characteristics for $\text{Al}_{0.8}\text{Ga}_{0.2}\text{As}$ reported elsewhere. Furthermore, the breakdown voltage was in agreement with values modelled when determining the multiplication.

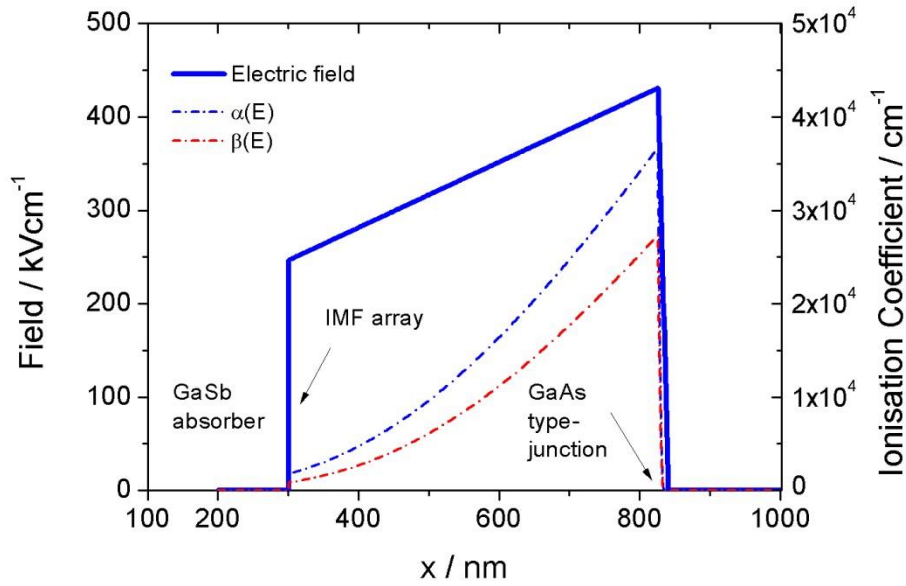


Figure 7.11: Electric field profile and ionisation coefficients, α and β , for electrons and holes, respectively, for the *GaAs design* sample.

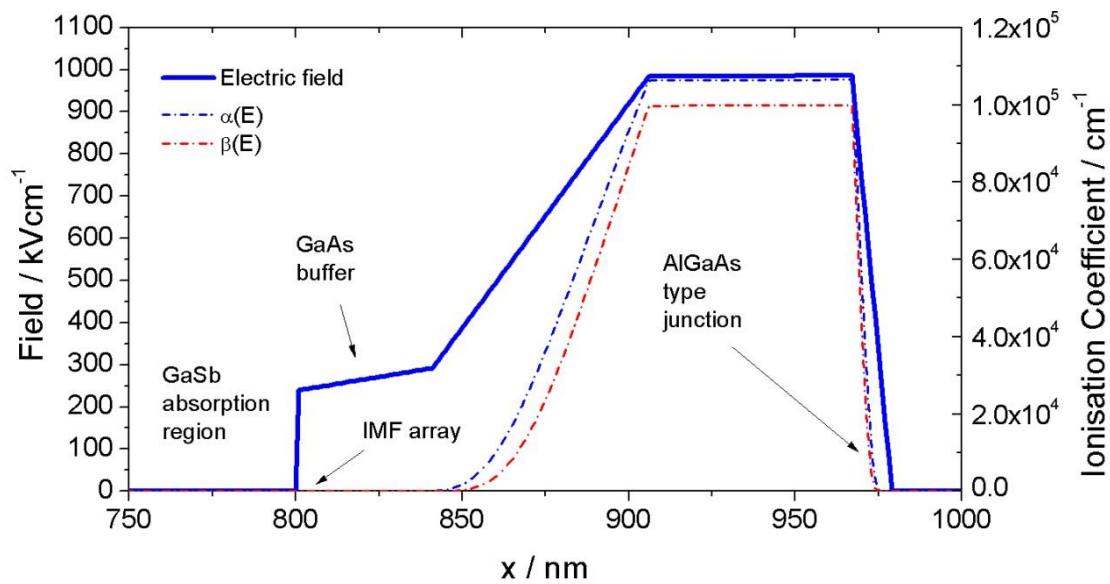


Figure 7.12: Electric field profile and ionisation coefficients, α and β , for electrons and holes, respectively, for the *AlGaAs design* sample.

vi) Discussion

APD structures based on GaAs and Al_{0.8}Ga_{0.2}As multiplication regions paired with GaSb absorption material were demonstrated. Excess noise behaviour was analysed, indicating that multiplication took place exclusively within the wide-bandgap region, and was not affected by ionisation effects in the GaSb absorber or at the IMF interface. At the same time, photosensitivity was demonstrated at 1.55 μm . Operation as a SAM-APD structure was therefore demonstrated in each case: the first demonstration of a SAM-APD structure using an IMF interface, and the first to combine GaAs and AlGaAs multiplication regions with a 6.1 \AA lattice-constant absorption material. However, further challenges remain if the design is to be developed into a commercial product. Notably the quantum efficiencies currently exhibited are very low (0.01% for the *GaAs design* and 0.002% for the *AlGaAs design*). These low quantum efficiencies likely occur as a by-product of the potential barriers at the GaSb/GaAs IMF interfaces between the absorption and multiplication layers, as illustrated by Figures 7.5 and 7.6 – a key limitation at present. For the *GaAs design*, the height of the potential barrier was approximated to be ~ 140 meV – i.e. significantly in excess of kT at room temperature. The weaker quantum efficiency for *AlGaAs design* sample may result from the larger potential barrier at the interface – approximated to be ~ 170 meV – and/or this may be due to the Al_{0.8}Ga_{0.2}As/GaAs conduction band offset (visible at around 0.92 μm in Figure 7.6). Avenues to overcome the potential barrier at the GaSb/GaAs interface could involve reducing the charge sheet doping level or thickness (for the *AlGaAs design*). The effect of this step would be to increase the electric field at the interface so that the potential barrier(s) were overcome. However, this would have the additional effect that the absorption region might experience significant field (potentially resulting in unwanted depletion currents associated with the narrow bandgap material) so that careful optimisation would be necessary in order to achieve optimal device performance.

At present, InGaAs/AlInAs-based SAM-APDs grown lattice-matched on InP – e.g. ref [9] – achieve far higher quantum efficiencies than the devices demonstrated in this chapter for a similar cut-off wavelength. While this is a key limitation of the present work, there are several important advantages to the use of an $\text{Al}_{0.8}\text{Ga}_{0.1}\text{As}$ multiplication region. Firstly, the dark currents are lower: at 90% of breakdown voltage current densities of $5.1 \times 10^{-6} \text{ Acm}^{-2}$ were noted earlier. This can be compared with $3 \times 10^{-4} \text{ Acm}^{-2}$ for the devices presented in ref [9]. Secondly, Excess noise is also reduced, since $\text{Al}_{0.8}\text{Ga}_{0.2}\text{As}$ offers very low values for $k_{\text{eff}} = \beta/\alpha$. However, the key advantage of the platform demonstrated in this work is that absorption regions can be chosen from other 6.1 Å materials. These include quaternary $\text{In}_{0.28}\text{Ga}_{0.72}\text{As}_{0.25}\text{Sb}_{0.75}$ material, which could allow for operation at 2.9 μm , and $\text{InAs}_{0.91}\text{Sb}_{0.09}$ material, which would allow operation beyond 4 μm . An SLS absorption region could also be used, allowing for devices with even longer cut-off wavelengths. Though optimisation of these designs is likely to be challenging, the combination of low-excess-noise and high-gain $\text{Al}_{0.8}\text{Ga}_{0.2}\text{As}$ multiplication regions with long-wavelength absorption regions is undeniably an attractive possibility.

Multiplication region material	Dark Current Density at 90% of breakdown voltage (Acm^{-2})	$k_{\text{eff}} = \beta/\alpha$
GaAs	1.6×10^{-5}	0.2 – 0.4
$\text{Al}_{0.8}\text{Ga}_{0.2}\text{As}$	3.0×10^{-6}	0.1 – 0.2

Table 7.1: Shows a summary of key figures of merit determined in this section for SAM-APD structures based on IMF growth. All data was recorded at 300 K.

References

- [1] A. Jallipalli, K. Nunna, M. N. Kutty, G. Balakrishnan, G. B. Lush, L. R. Dawson, and D. L. Huffaker, *Appl. Phys. Lett.* 95, 072109 (2009).
- [2] S. Sridaran, A. Chavan, and P. S. Dutta, *J. Cryst. Growth* 310, 1590 (2008).
- [3] J. C. Campbell, S. Chandrasekhar, W.T. Tsang, G. J. Qua, B. C. Johnson, *J. Lightw. Technol.* 7, 3 (1989).
- [4] Y. L. Goh, D. J. Massey, A. R. J. Marshall, J. S. Ng, C. H. Tan, W. K. Ng, G. J. Rees, M. Hopkinson, J. P. R. David and S. K. Jones, *IEEE Trans. Electron Devices* 54, 1 (2007).
- [5] S. A. Plimmer, J. P. R. David, and D. S. Ong, *IEEE Trans. Electron Devices* 47, 1080 (2000).
- [6] R. J. McIntyre *IEEE Trans. Electron Devices* 13, 1, 164 (1966).
- [7] K. F. Li, D. S. Ong, J. P. R. David, G. J. Rees, R. C. Tozer, P. N. Robson, and R. Grey, *IEEE Trans. Electron. Devices* 45(10), 2102 (1998).
- [8] B. K. Ng, “Impact ionisation in wide bandgap semiconductors: $\text{Al}_x\text{Ga}_{1-x}\text{As}$ and 4H-SiC” (thesis) (2012).
- [9] M. Lahrichi, G. Glastre, E. Derouin, D. Carpentier, N. Lagay, J. Decobert, and M. Achouche, *IEEE Photon. Technol. Lett.* 22, 18 (2010).

(8) Conclusions and suggestions for further work

Lattice mismatched infrared photodetectors were studied, ranging from simple *p-i-n* photodiodes to *nBn* detectors to separate absorption and multiplication (SAM) APDs.

Even under highly optimised growth conditions, simple GaSb *p-i-n* diode structures grown using interfacial misfit (IMF) arrays were found to exhibit significantly greater dark current densities (0.9 Acm^{-2} and 0.18 Acm^{-2} , for devices grown on Si and GaAs, respectively, at 300 K and -1.0 V) compared with their counterparts grown on native GaSb (0.01 Acm^{-2} for the same bias condition). These elevated currents were attributed to Shockley Read Hall centre due threading dislocations propagating into the electrically active regions of the device structures. While, transmission electron microscopy (TEM) revealed highly-periodic arrays of 90° misfit dislocations – i.e. IMF arrays – which were shown (via XRD Bragg spacings) to relieve almost all of the interfacial strain, TEM further confirmed the presence of a relatively large density of threading dislocations in these structures ($> 10^8 \text{ cm}^{-2}$ as compared with $5 \times 10^5 \text{ cm}^{-3}$, as reported by Huang et al.¹). It was proposed that these occurred due to small differences between the array periods (9:8 for AlSb/Si and 13:14 for GaSb/ GaAs) and the ratios of the lattice constants of AlSb and Si, and GaSb and GaAs, resulting in the unwanted occurrence of vertically-travelling 60° misfit dislocations. A search of literature preceding the work of Huang et al. revealed that previous works also observed periodic misfit arrays for the growth of GaSb on GaAs but – in addition – threading dislocation densities similar to those presented here. The above taken into account, it should be pointed out that, while growth temperatures and III-V ratios for GaSb/GaAs growth were carefully tuned over a large many wafers to obtain optimum RHEED patterns, XRD diffraction curves and surface finish, the final TEM results presented in this work were based on a single set of samples. Without commissioning a new study with a large number of TEM measurements on multiple samples, an

independent figure for the exact minimum threading dislocation density achievable using the growth conditions described in this work is not available.

One solution reported to address both SRH and surface leakage currents is the *nBn* detector design. It was therefore decided to try to grow *nBn* detector structures on GaAs substrates using the IMF growth mode. In Section (6), *nBn* detector structures were found to be particularly suited to lattice mismatched growth. Moderate absorption layer doping was found to be critical for devices grown on GaAs, due to a suppression of field in the absorber and/or pinning of the Fermi level at the band edge, away from mid-gap SRH centres. With an *n*-type doping level of $\sim 4 \times 10^{17} \text{ cm}^{-3}$, dark current densities at 200 K were found to be within a factor of 5 when comparing samples grown on GaAs via an IMF array and samples grown lattice matched on a GaSb substrate ($1.6 \times 10^{-5} \text{ Acm}^{-2}$ and $3 \times 10^{-6} \text{ Acm}^{-2}$, respectively). These figures can further be compared with Rule 07, which shows that an optimised, diffusion limited HgCdTe-based *p-i-n* (operating at the same wavelength and temperature) would exhibit a dark current density of $\sim 1.3 \times 10^{-6} \text{ cm}^{-2}$. D^* figures of $1.5 \times 10^{10} \text{ cmHz}^{1/2}\text{W}^{-1}$ and $9.8 \times 10^{10} \text{ cmHz}^{1/2}\text{W}^{-1}$ at 200 K were calculated, respectively, so that the performance of the sample grown on GaAs was within a factor of 6 of the sample grown on native GaSb at 200 K. A key limitation of the work carried out was that the responsivities measured were lower than 0.15 AW^{-1} at operating bias and temperature. While higher responsivities reported for similar devices were noted in Section (6) [Soibel] for samples with undoped absorbers and optimised band offsets, it can be said that *nBn* devices in general tend to have lower responsivities than *p-i-n* diodes based on the same materials due to the absence of field in the absorption layer. Nonetheless, growth on GaAs was noted to be particularly appealing, due to large area substrates being available. In particular, large-area focal plane arrays could be possible. GaAs substrates are also available more cheaply than their GaSb counterparts, so that lattice-mismatched epitaxy could reduce production costs for applications where the most

highly optimised performance is not required. Infrared devices and FPAs could then be delivered to the mass market. The observed resilience of nBn detectors to threading dislocations/defects also suggests that these devices could be particularly suited to extra-terrestrial applications, where radiation hardness is key. Further work might include the testing of irradiated nBn detectors, where the effects of damage to the lattice (i.e. increased dark currents) may be reduced (compared with that for a $p-i-n$ diode) due to the suppression of SRH currents by the nBn design. It was further demonstrated in Section (6) that the cut-off wavelength of an nBn detector could, at least in principle, be extended by using an absorption layer of arbitrary lattice constant (i.e. that there is, in principle, no need to lattice match the absorption layer to the GaSb buffer). Diffusion-limited devices were demonstrated with a cut-off wavelength of 5.4 μm and an absorption layer composition of $\text{InAs}_{0.79}\text{Sb}_{0.21}$. Further work would be required to grow the barrier layer lattice matched to the absorption layer, and hence remove the possibility of relaxation (which could lead to spikes or potential barriers in the valence band, impeding the flow of photogenerated carriers). Longer wavelength nBn devices have also been reported in the literature, using strained-layer-superlattice (SLS) absorption regions. As noted in Section (3), these have generally used type-II InAs/GaSb layers. However, there are relatively few² papers in the literature giving details of Ga-free nBn SLS designs (i.e. those which use an InAs/InAsSb SLS). The author has been party to preliminary work modelling and growing such structures. Based upon photoluminescence measurements, good agreement was found with the model of Shen,³ suggesting operation would be possible between approximately 5 μm and (at least) 12 μm . Given that the superlattice band structure can be adjusted by varying the Sb fraction in the InAsSb layers it would then be possible also to grow two-colour designs based on this architecture. From the publications list in the introduction, the reader may have noticed that the author has also been party to the development of a short-wave infrared (SWIR) nBn detector, based on an InGaAsSb quaternary material absorption layer. These layers have a

wider bandgap than the InAs(Sb) layers typically used for the absorption material of an *nBn* detector, allowing for reduced dark currents and a higher D^* figures (for the same temperature of operation) when compared to existing *p-i-n* designs based on InAsSb or InAs/GaSb SLS. Once again, bandgap engineering allowed for the suppression of dark currents due to majority carriers, but a near-zero valence band offset, allowing for the flow of photogenerated holes.

Novel avalanche photodiode (APD) structures were demonstrated in Section (7). These used IMF arrays incorporated into the electrically active region of the device (as opposed to the *nBn* designs of Section (6), which simply used a GaSb buffer layer as a “virtual substrate”). Through this approach, it was possible to create GaAs and $\text{Al}_{0.8}\text{Ga}_{0.2}\text{As}$ APDs with GaSb absorption regions – for the first time in a SAM structure – so that the dark current behaviour and noise characteristics of the former could be paired with the 1.7 μm cut-off wavelength of the latter. Low leakage currents were exhibited due to the confinement of the electric field within the wide bandgap regions (at room temperature values of $5.7 \times 10^{-4} \text{ Acm}^{-2}$ and $5.1 \times 10^{-6} \text{ Acm}^{-2}$ were recorded for the GaAs APD and the $\text{Al}_{0.8}\text{Ga}_{0.2}\text{As}$ APD, respectively). The presence of photocurrent – under excitation from a 1.55 μm laser – further confirmed carrier transport across the IMF interface. Excess noise measurements were also carried out in order to determine whether ionisation was successfully confined to the wide bandgap regions. The results confirmed electron initiated multiplication taking place, with no effects due to ionisation in the GaSb regions or at the IMF interface observed – indeed confirming successful operation as a SAM-APD. In particular, values of $0.2 < k_{\text{eff}} < 0.4$ and $0.1 < k_{\text{eff}} < 0.2$ were recorded (for GaAs and $\text{Al}_{0.8}\text{Ga}_{0.2}\text{As}$, respectively), with the latter indicating very low excess noise with multiplication values up to 10^4 achieved. However, it should be noted that these devices had very limited ($<0.01\%$) quantum efficiency (QE), likely owing to potential barriers at the IMF interfaces. Avenues to alleviate this problem could include the use of an optimised charge sheet. Whilst these devices are not intended to compete directly with InGaAs/AlInAs designs,

which offer robust quantum efficiency figures for 1.55 μm operation, the prospect of using other absorption layer materials which are lattice matched to GaSb, e.g. InAsSb, InGaAsSb or even SLS layers, could allow for longer wavelength APDs retaining the dark current and noise behaviours of $\text{Al}_{0.8}\text{Ga}_{0.2}\text{As}$ to be conceived. Single photo-n avalanche photodiode (SPAD) operation could also be possible, even in the long wavel-ength range – a GaAs APD could be particularly suitable for this mode of operation (since, for GaAs, $k_{\text{eff}} = \beta/\alpha \sim 0.5$, the breakdown is abrupt).

In view of the above, the limitations of simple GaSb *p-i-n* diodes based on the IMF growth mode should be put into perspective. It is indeed possible to transition the lattice constant of GaAs to 6.09 Å in a way that minimises the threading dislocation density, with most of the strain at the interface being relieved through an array of 90° misfit dislocations. The residual threading dislocation density ($\sim 10^8 \text{ cm}^{-2}$) – whilst significant – is not inhibitive to the development of novel device structures, several of which have been demonstrated in particular in this work.

References

- [1] S. Huang, G. Balakrishnan, and D. L. Huffaker, J. Appl. Phys. 105, 103104 (2009).
- [2] H. S. Kim, O. O. Cellek, Z.-Y. Lin, Z.-Y. He, X.-H. Zhao, S. Liu, H. Li and Y.-H. Zang, Applied Physics Letters, 101, 161114 (2012).
- [3] M. Shen and W. Cao, Mat. Sci. Eng. B-Solid., 103, 122-127 (2003).

Appendix I – Constants for Bandstructure Modelling

	a	c_{11}	c_{12}	c_{44}	$E_{v,av}$	Δ_0	$E_0(\Gamma)$	$E_0(X)$	$E_0(L)$	a_v	$a_c(\Gamma)$	b	d
AlP	5.451	1.32	0.63	0.62	-8.09	0.07 ^a	3.58	2.45	3.11 ^a	3.15	-5.54	-1.6 ^a	
AlAs	5.660	1.25	0.53	0.54	-7.49	0.28	2.95	2.16 ^b	2.80 ^a	2.47	-5.64	-1.5 ^a	
AlSb	6.136	0.88	0.43	0.41	-6.66	0.65	2.22	1.61 ^c	2.21 ^c	1.38	-6.97	-1.4	-4.3
GaP	5.451	1.41	0.62	0.70	-7.40	0.08	2.74	2.26	2.63	1.70	-7.14	-1.5	-4.6
GaAs	5.653	1.18	0.54	0.59	-6.92	0.34	1.42	1.91 ^b	1.73 ^b	1.16	-7.17	-1.7	-4.6
GaSb	6.096	0.88	0.40	0.43	-6.25	0.82	0.72	1.05 ^c	0.76 ^c	0.79	-6.85	-2.0	-4.8
InP	5.869	1.02	0.58	0.46	-7.04	0.11	1.35	2.21 ^d	2.05 ^d	1.27	-5.04	-1.6	-4.2
InAs	6.058	0.83	0.45	0.40	-6.67	0.38	0.36	1.37 ^d	1.07 ^d	1.00	-5.08	-1.8	-3.6
InSb	6.479	0.66	0.36	0.30	-6.09	0.81	0.17	1.63 ^d	0.93 ^d	0.36	-6.17	-2.1	-5.0

A method to calculate strain-dependent band offsets in III-V heterostructures was presented in Section (2). Constants from Krijn's paper¹ are reproduced here for easy reference. a is the lattice constant, c_{11} , c_{12} and c_{44} are elastic constants, $E_{v,av}$ is the average valence band position for heavy and light holes (before strain is considered), Δ_0 is the spin orbit split-off energy, $E_g(\Gamma, X, L)$ are the bandgaps for the Γ , X and L valleys (although only the Γ valley is considered in the present work), a_v and a_c are the hydrostatic deformation potentials for the valence band and the conduction band, respectively and b and d are the shear deformation potentials.

[1] M. P. C. M. Krijn, *Semicond. Sci. Technol.* 6, 27 (1991).

Appendix II – Spectral Response Model

Sze [1] showed that the spectral quantum efficiency (QE) for a $p-i-n$ diode can be modelled by considering the material absorption coefficient, $\alpha(\lambda)$, the electron and hole diffusion lengths, L_e and L_h , diffusion constants, D_e and D_h , the surface recombination velocities at the p - and n -type contacts, S_p and S_n , the depletion width, x_d , the p -type neutral region thickness, x_p , and the n -type neutral region thickness, x_n . Once these quantities, illustrated in Figure 1, are known, the photocurrent density due to electrons diffusing from the p -type neutral region to the depletion region can be written

$$J_e = \frac{qF(1-R)\alpha L_e}{\alpha^2 L_e^2 - 1} \left(\frac{\left(\frac{S_p L_e}{D_e} + \alpha L_e \right) - e^{-\alpha x_p} \left(\frac{S_p L_e}{D_e} \cosh\left(\frac{x_p}{L_e}\right) + \sinh\left(\frac{x_p}{L_e}\right) \right)}{\left(\frac{S_p L_e}{D_e} \right) \sinh\left(\frac{x_p}{L_e}\right) + \cosh\left(\frac{x_p}{L_e}\right)} \right) \quad (1)$$

where F is the incident photon flux, R is the surface reflectance and q is the elementary charge. Correspondingly, the photocurrent density due to holes diffusing from the n -type neutral region to the depletion region can be written

$$J_h = \frac{qF(1-R)\alpha L_h}{\alpha^2 L_h^2 - 1} \exp(-\alpha(x_p + x_d)) \times \left(\alpha L_h - \frac{\left(\frac{S_n L_h}{D_h} \right) \left(\cosh\left(\frac{x_n}{L_h}\right) - \exp(-\alpha x_n) \right) + \sinh\left(\frac{x_n}{L_h}\right) + \alpha L_h \exp(-\alpha x_n)}{\left(\frac{S_n L_h}{D_h} \right) \sinh\left(\frac{x_n}{L_h}\right) + \cosh\left(\frac{x_n}{L_h}\right)} \right) \quad (2)$$

and the photocurrent arising due to carriers absorbed in the depletion region itself can be written,

$$J_{dr} = qF(1-R) \exp(-\alpha x_p) (1 - \exp(-\alpha x_d)) \quad (3)$$

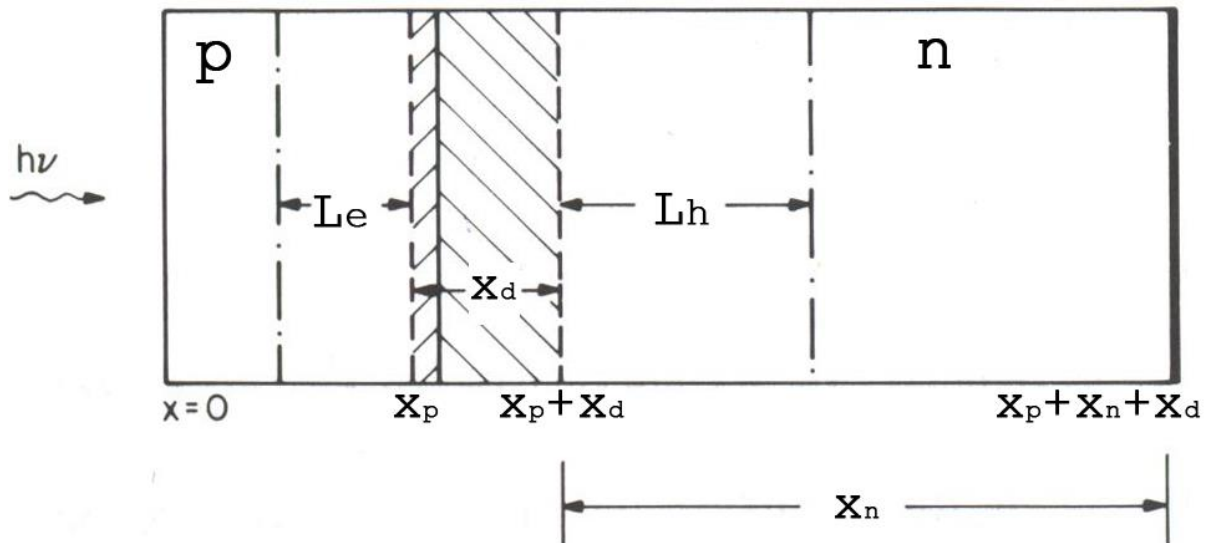


Figure 1: Illustration of a $p-i-n$ photodiode, with L_e , L_h , x_p , x_n and x_d indicated, as described in the text.

so that the total photocurrent is then given by the sum of equations 1, 2, and 3. Finally, the quantum efficiency is given by setting F equal to unity and dividing by the sum by q . A loop is then used to evaluate the above equations as a function of wavelength.

[1] S. M. Sze, Physics of Semiconductor Devices, 2ED (1981).